Title	Growth Morphology of Solidification Microstructure and Anisotropy of Solid-liquid Interfacial Energy
Author(s)	KIM, GEUN WOO
Degree Grantor	北海道大学
Degree Name	博士(工学)
Dissertation Number	甲第15107号
Issue Date	2022-06-30
DOI	https://doi.org/10.14943/doctoral.k15107
Doc URL	https://hdl.handle.net/2115/87697
Type	doctoral thesis
File Information	Geunwoo_Kim.pdf

HOKKAIDO UNIVERSITY

Growth Morphology of Solidification Microstructure and Anisotropy of Solid-liquid Interfacial Energy

A DISSERTATION

SUBMITTED TO THE GRADUATE SCHOOL

IN PARTIAL FULFILLMENT OF THE REQUIREMENTS

for the degree

DOCTOR OF PHILOSOPHY

By

Geunwoo Kim

Dissertation Committe: Munekazu Ohno

Naoyuki Hashimoto

Norihito Sakaguchi

Graduate School of Engineering

Division of Materials Science and Engineering

Research Group of Materials Design

Laboratory of Microstructure Control

April 2022

Abstract

Growth morphologies of solidification microstructures in metallic materials, are largely determined by the anisotropy of solid-liquid interfacial energy, $\gamma(\boldsymbol{n})$, where $\boldsymbol{n}$ is unit vector normal to the interface. Therefore, the anisotropy of $\gamma(\boldsymbol{n})$ is an essential information in understanding and controlling the solidification microstructures. The intefacial anisotropy in fcc crystals is described by anisotropy parameters ε_1 and ε_2 that characterize $\langle 100 \rangle$ and $\langle 110 \rangle$ growth, respectively. In most of previous studies on dendritic growth in fcc-based metallic alloys, the growth morphology of fcc alloys has been supposed to be $\langle 100 \rangle$ dendrite and, accordingly, only ε_1 has been considered. However, it was recently revealed that the growth morphology of some fcc alloys changes from $\langle 100 \rangle$ to $\langle 110 \rangle$ dendrite by increasing concentration of the solute element, which means that ε_1 and ε_2 depend on the solute concentration. This phenomenon must be taken into account in controlling solidification microstructures with high accuracy. However, details of morphological change and dependence on solidification conditions and alloy systems have not been clarified yet. Therefore, in this study, morphological diversity of isothermally- and directionally- solidified microstructure associated with transition in ε_1 and ε_2 is closely investigated by means of phase-field simulations.

Meanwhile, the anisotropy parameters of practical alloys have been rarely clarified. To experimentally determine ε_1 and ε_2, an equilibrium shape of the solid must be first realized, and then the solid-liquid interface region shold be imaged clearly enough to accurately elucidate a few percent difference of $\gamma(\boldsymbol{n})$ in metallic system. Because of these difficulties, the experimental measurement of anisotropy parameters has been rarely reported. As a computational method, molecular dynamics (MD) simulations is effective way to determining ε_1 and ε_2. The capillary fluctuation method and cleaving technique have been developed for computing these anisotropy

parameters based on MD simulations and have been successfully applied to several types of materials. However, the accuracy of MD simulations is largely influenced by atomic potential which is not always accurate. Therefore, in this study, a novel method for estimation of anisotropy parameters is proposed by combining phase-field simulations and machine learning overcoming the above-mentioned difficulties.

This thesis consists of six chapters and the organization is described below.

In chapter 1, the importance of anisotropy of solid-liquid interfacial energy was described. In ad- dition, the diversity of the growth morphology and the necessity for measuring anisotropy were ex- plained.

In chapter 2, the quantitative phase-field model which allows for simulations of solidification mi crostructure with high accuracy was explained.

In chapter 3, the morphological diversity of isothermally-solidified microstructure associated with different anisotropy was investigated by systematically changing ε_1 and ε_2. The growth morphologies were classified into four types, i.e. $\langle 100 \rangle$, $\langle 100 \rangle-$like hyperbranched, $\langle 110 \rangle-$like hyperbranched and $\langle 110 \rangle$ growth. The morphology map for isothermally-solidified microstructure was constructed based on this classification. Furthermore, dependencies of this map on solidification condition and alloy system were also investigated by changing initial supersaturation and partition coefficient, respectively. It was found that $\langle 100 \rangle$ growth, which is typical growth pattern of fcc-based alloy, hardly occurs when initial supersaturation is large and/or partition coefficient is small.

In chapter 4, the morphological diversity of directionally-solidified microstructure associated with the different anisotropy was investigated by systematically changing the anisotropy parameters and the angle between $\langle 100 \rangle$ crystallographic orientation and heat flow direction. The growth morphologies were classified into three types, i.e. $\langle 100 \rangle$, seaweed and $\langle 110 \rangle$ growth. The morphology map for directionally-solidified microstructure was constructed based on the classification. Furthermore, dependence of this map on solidification conditions such as pulling speed and temperature gradient was investigated. It was found that the seaweed growth region in the space of ε_1 and ε_2 slightly becomes wider as the pulling speed decreases.

In chapter 5, an inverse analysis method of estimating the anisotropy parameters of solid-liquid interfacial energy was developed based on the machine learning. The

interfacial shape distribution (ISD) map, which characterizes the details of three-dimensional dendrite morphology, was selected as the input for convolutional neural network, a method of machine learning employed in this study. The feasibility of this approach was tested by performing quantitative phase-field simulations for a free-growing dendrite during isothermal solidification of a model alloy system to obtain training and test data. Both ε_1 and ε_2 were estimated with errors less than 5%, which can be further improved by increasing the size of the training data.

In chapter 6, the overall summary and conclusions of this thesis were presented.

Contents

Chapter 1

Introduction

1.1　Dendrite and preferred growth direction

Many kinds of practical metallic alloys such as steel, aluminum and magnesium alloys are manufactured by solidification processes such as casting and welding. Various types of solidification microstructures form after solidification, depending on solidification condition and solute concentrations. Features of solidification structures such as size and morphology of solidified grains have a large influence on various properties of metallic materials [1–5]. Therefore, prediction and control of solidification microstructures are of great importance in production of high quality materials.

A dendrite, which is exemplified in Fig. 1.1, is a typical shape of crystals growing in an undercooled melt during solidification of metallic materials [1, 4]. This microstructure is formed by crystal growing in specific crystal direction, so-called preferred growth direction (PGD). PGD of the dendrite is an important factor controlling the growth morphology [1]. It has been believed or assumed that PGD depends only on the crystal structure in most of early works of solidification and casting [1,3]. It is usually considered that PGD is always $\langle 100 \rangle$ in cubic crystals such as face centered cubic (fcc) and body centered cubic (bcc), while $\langle 11\bar{2}0 \rangle$ and $\langle 0001 \rangle$ for hexagonal close-packed (hcp) crystals [7,8]. However, it was found that PGD of some fcc alloy changes by solute concentration [9]. This transition phenomenon of PGD will be explained in detail in the next section.
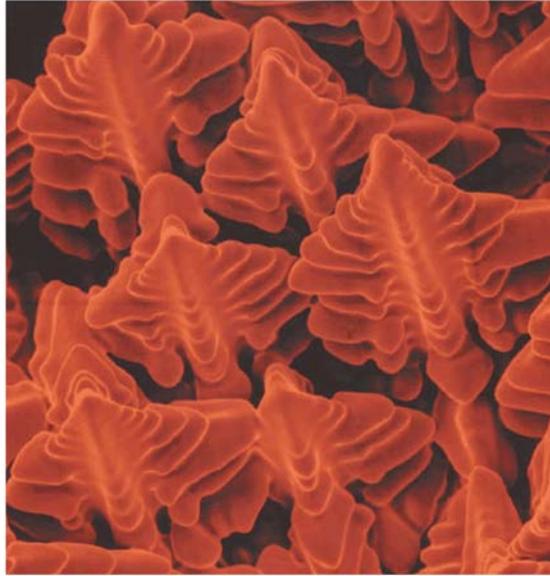
Fig. 1.1. Dendritic microstructure of Ni-based alloy [6].

1.2 Transition in preferred growth direction

Figure 1.2 shows the transition phenomenon of PGD observed in Al-Zn alloy, where the horizontal axis and the vertical axis indicate Zn concentration and misorientation angle between the growth direction of dendrite of fcc crystal (Al-rich solid solution) and $\langle 100 \rangle$ crystal direction, respectively [9]. As shown in Fig. 1.2, it was revealed that PGD of fcc solid solution in Al-Zn alloy changes from $\langle 100 \rangle$ to $\langle 110 \rangle$ with increasing Zn concentration, even though the crystal structure of Al-Zn alloy is fcc in all concentration range [9]. A similar behavior was also observed in Al-Ge alloys [10], Al-Sm alloys [11], other fcc alloys (Cu-Zn and Ni-Co) [12] and hcp alloys (Mg-Zn and Mg-Sn) [13, 14]. Thus, transition of PGD may occur in many kinds of alloy systems. These findings demonstrate diversity of PGD in alloy solidification phenomena, which has not been clearly taken into account in controlling solidification microstructure in early works [15]. Then, it is very important to reveal diversity of solidification microstructure associated with the diversity of PGD. The underlying mechanism of this phenomenon is closely related to anisotropic property of solid-liquid interfacial energy, which will be explained in the next section.
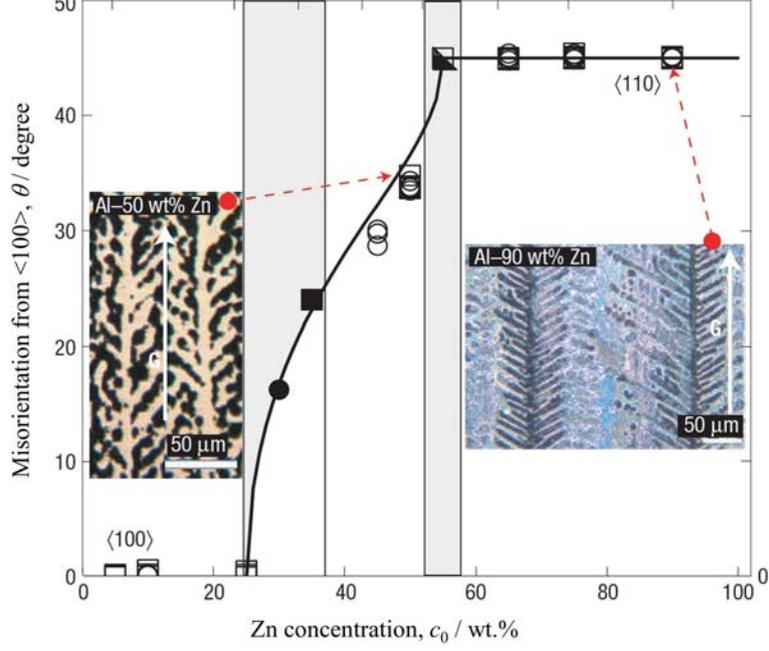
Fig. 1.2. Growth direction of columnar dendrite of Al-Zn alloy [9].

1.3 Anisotropy of solid-liquid interfacial energy

In solidification of metallic materials with negligible interfacial attachment kinetics, PGD of dendrite is largely determined by anisotropy of solid-liquid interfacial energy $\gamma(\boldsymbol{n})$ where $\boldsymbol{n}$ is unit vector normal to the interface. Dendrite will pick easy growth direction by the largest $\gamma(\boldsymbol{n})$ to minimize the entire interfacial energy or by the lowest interfacial stiffness, $S(\boldsymbol{n})$. Stiffness can be understood as a degree of the resistance to deformation of the interface. Thus, it can be understood that it is difficult for the crystal to grow in the direction in which the stiffness is large, and it is easy to grow in the direction in which the stiffness is small. Interfacial stiffness can be expressed in following manner, $S = \gamma + \gamma''$, and in three dimensions, the stiffness can be expressed by following equation:

$$S = 2\gamma + \frac{\partial^2 \gamma}{\partial \theta} + \frac{1}{\sin^2 \theta} \frac{\partial^2 \gamma}{\partial \varphi^2} + \cot \theta \frac{\partial \gamma}{\partial \theta} \tag{1.1}$$

where θ and φ are conventional spherical angular coordinates of the interface normal $\boldsymbol{n}$. Haxhimali et al. [9] analyzed this stiffness and predicted preferred growth direction by introducing interfacial energy of cubic crystal which is given by following

3

equation [16, 17]:

$$\gamma(\boldsymbol{n}) = \gamma_0 \left[1 + \varepsilon_1 \left(Q(\boldsymbol{n}) - \frac{3}{5} \right) + \varepsilon_2 \left(3Q(\boldsymbol{n}) + 66S(\boldsymbol{n}) - \frac{17}{7} \right) \right] \qquad (1.2)$$

where $Q(\boldsymbol{n}) = n_x^4 + n_y^4 + n_z^4$, $S(\boldsymbol{n}) = n_x^2 n_y^2 n_z^2$ and n_i are Cartesian components of $\boldsymbol{n}$. ε_1 and ε_2 denote anisotropy parameter and the anisotropic property of $\gamma(\boldsymbol{n})$ is described by those anisotropy parameters. They calculated and visualized $1/S$ plot
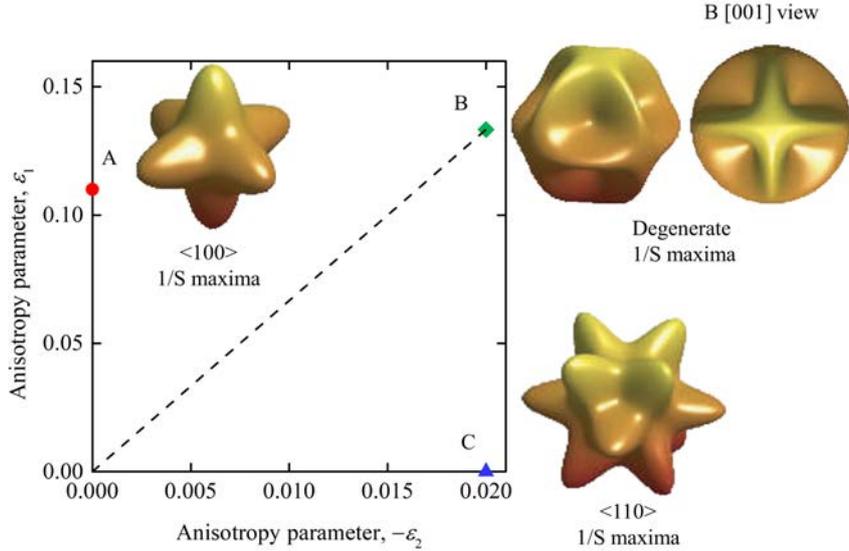
Fig. 1.3. Morphology selectiom map from minimum interfacital stiffness [9].

as a function of orientation $\boldsymbol{n}$ for different sets of anisotropy parameters. Stiffness minima, which correspond to maxima of $1/S$, are clearly seen in a map given in Fig.1.3. This map shows the two distinct regions with stiffness minima corresponding to $\langle 100 \rangle$ and $\langle 110 \rangle$ respectively, separated by a boundary line $\varepsilon_1 = -20\varepsilon_2/3$.

From this result, one can understand that the crystal preferentially grows in $\langle 100 \rangle$ orientation and PGD is $\langle 100 \rangle$, when ε_1 is dominant. On the other hand, when ε_2 is dominant, the crystal preferentially grows in $\langle 110 \rangle$ orientation and PGD accordingly corresponds to $\langle 100 \rangle$ [9, 18]. Therefore, the transition of PGD observed in Al-Zn alloys [9] must be associated with dependences of anisotropy parameters ε_1 and ε_2 on the solute concentration.

Note that actual growth morphology of dendrites is determined not only by PGD but also by conditions of solidification such as initial undercooling (or supersaturation), cooling rate and temperature gradient. Haxhimali et al. [9] performed

phase-field simulations of free dendritic growth in a pure material by changing ε_1 and ε_2 systematically and they found that actual growth direction continuously changes from $\langle 100 \rangle$ to $\langle 110 \rangle$ when a set of ε_1 and ε_2 shifts from a range of ε_1-dominant to the one of ε_2-dominant. In the intermediate range, a dendrite having many branches in various orientations appears and it is called hyperbranched growth. They summarized these results using morphology map which indicates the growth morphology of the dendrite in ε_1-ε_2 space, as shown in Fig. 1.4. There are three growth regions in
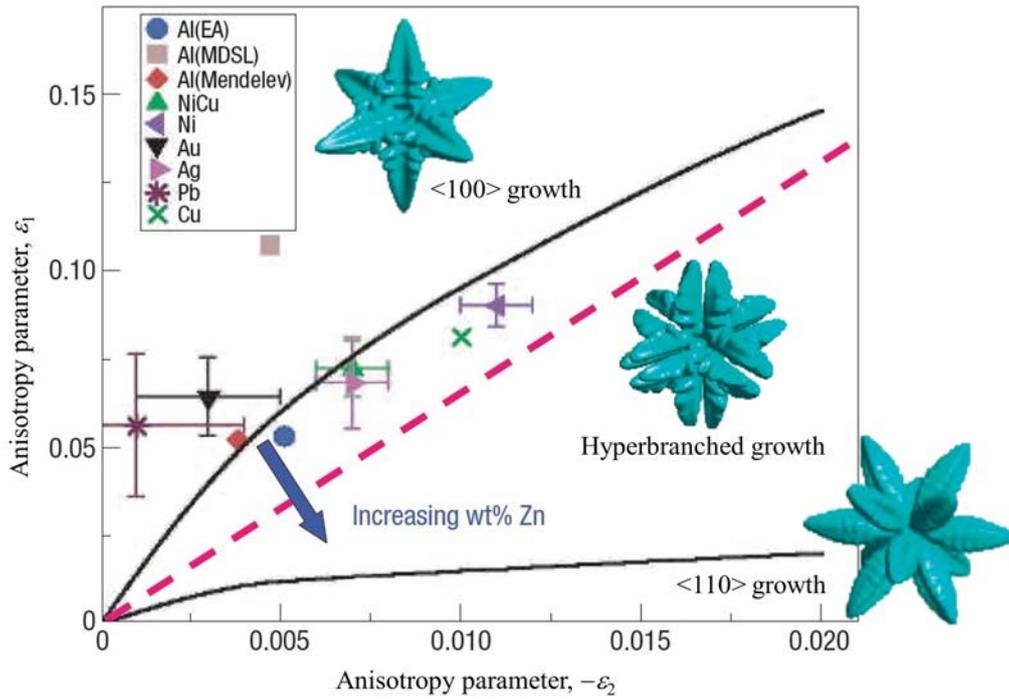
Fig. 1.4. Morphology map from phase-field simulation [9].

the orientation selection map, i.e. $\langle 100 \rangle$, $\langle 110 \rangle$ and hyperbranched growth regions. Although the morphology map obtained by Hahimali et al. [9] is valid only for the pure material at a fixed degree of undercooling, the morphology map for Al-Zn alloy system obtained by Dantzig et al. by means of phase-field simulations [19] is essentially the same as the one in the pure material [9].

1.4 Morphological diversity of columnar dendrite

Columnar dendrites form by directional solidification or near the wall of mold in casting process, and the columnar dendrite structure is one of typical solidification microstructures (see Fig. 1.5). Therefore, it is necessary to investigate the influ-
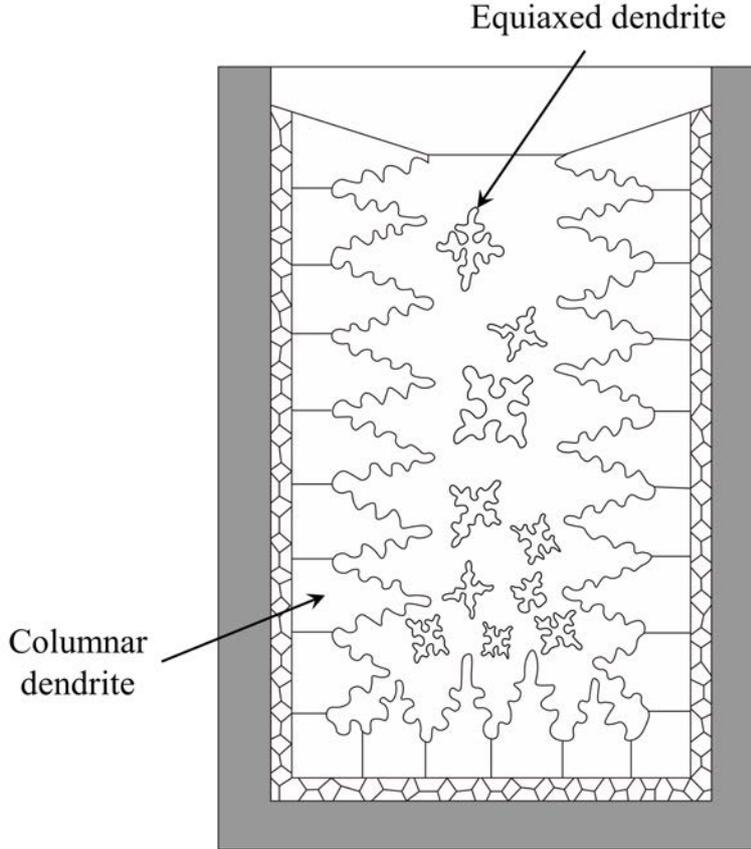
Fig. 1.5. Typical casting microstructure.

ence of the transition phenomenon of PGD on morphology of columnar dendrite. Dantzig et al. investigated the morphological change of columnar dendrite by means of phase-field simulation of Al-Zn binary alloy [19]. They systematically varied two kinds of anisotropy parameter, from ε_1 dominant region to ε_2 dominant region (see Fig.1.6). Similar to equiaxed dendrite, columnar dendrite also grows preferentially in $\langle 100 \rangle$ when ε_1 is dominant, while it grows in $\langle 110 \rangle$ when ε_2. Seaweed structures were formed in the intermediate region. This finding agrees well with the experimental result [9] and they finally made a correlation between the Zn composition and anisotropy parameters [19]. However, simulations performed in early work [19], are conducted very small computational size and only for the initial state of solid-
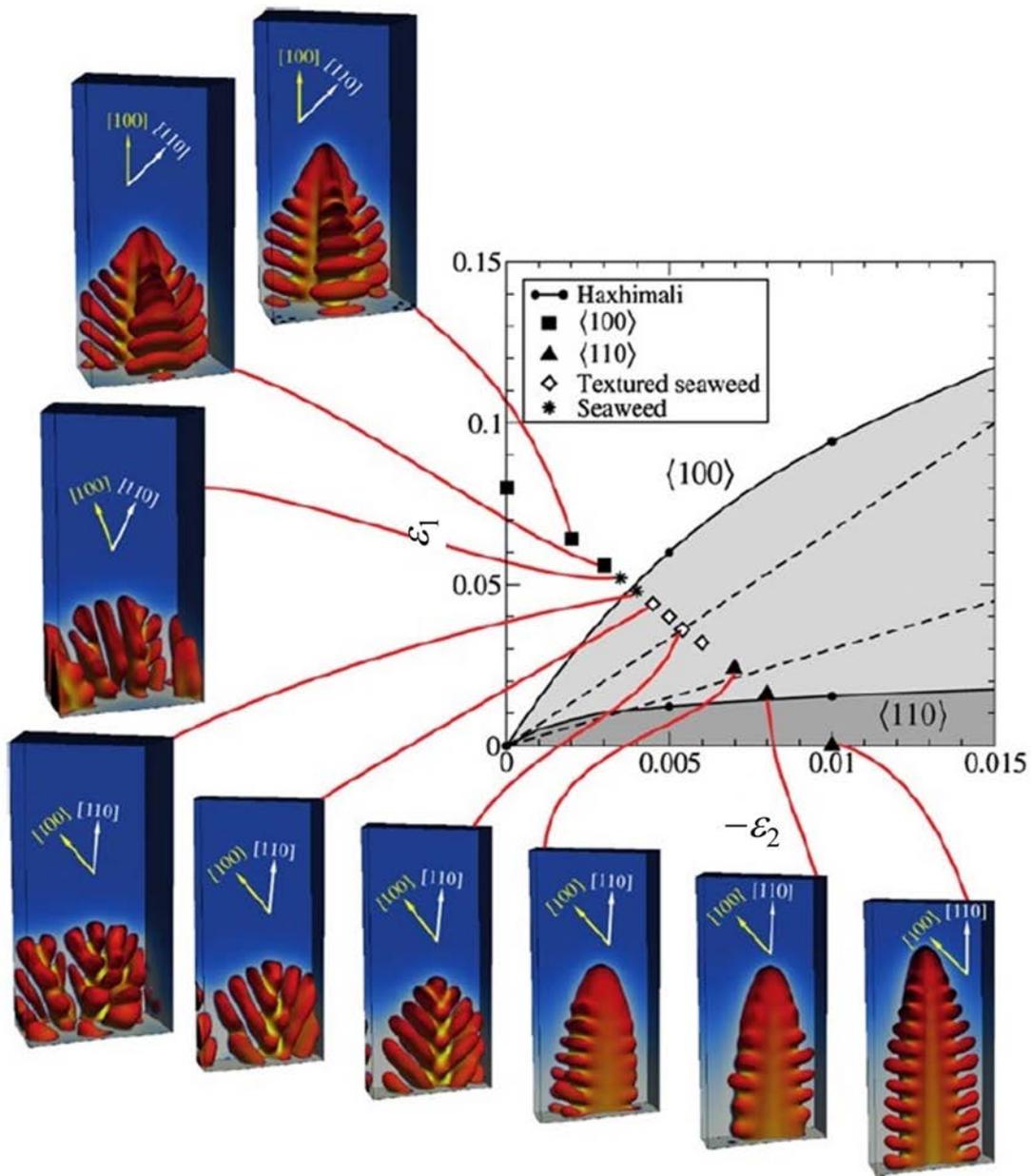
Fig. 1.6. Directionally-solidified microstructures and morphology map [19].

ification. Thus, further investigations should be needed at larger domain size and longer solidification time.

Also, this phase-field study [19] is conducted for only one set of temperature gradient and pulling speed. Chen et al. [20] investigated morphological change of Al-Zn alloy with different pulling speed by directional solidification experiments. They found that Al-32wt.% Zn alloy forms seaweed structure at low pulling speed ($\sim$150μm), while it forms $\langle 110 \rangle$ growth columnar dendrite at high pulling speed (1000μm) [20]. This finding implies that morphological change of columnar dendrite associated with transition in PGD could be affected by pulling speed.

1.5   Estimation of anisotropy parameter

In sections 1.3-1.4, it has been described that as the solute concentration of the alloy changes, PGD changes and growth morphology is formed in various ways, for example, $\langle 100 \rangle$ dendrite, $\langle 110 \rangle$ dendrite, hyperbranched and seaweed structure. However, the anisotropy parameters of the practical alloy system are rarely reported. Therefore, there have been many efforts through experiments and simulations to determine this anisotropy parameter. To experimentally determine ε_1 and ε_2, an equilibrium shape of the solid must be first realized, and then the solid-liquid interface region should be imaged clearly enough to accurately elucidate a few percent difference of $\gamma(\boldsymbol{n})$ in metallic system. Because of these difficulties, the experimental measurement of anisotropy parameters has been rarely reported [21]. As a computational method, molecular dynamics (MD) simulations are effective way to determine ε_1 and ε_2. The capillary fluctuation method [22] and cleaving technique [23] were developed for computing ε_1 and ε_2 from MD simulations. These methods have been successfully applied to several types of materials. However, the accuracy of MD simulations is largely influenced by atomic potential, and there is a problem that anisotropy parameters can only be measured within limited alloy system. Therefore, there is a need for a new method to determine anisotropy parameters capable of overcoming the above-mentioned difficulties.

With the recent development of in-situ observation technology, it has become possible to accurately measure the three-dimensional morphology of solidification microstructure using x-ray tomography (see Fig. 1.7 (a)). Comparing the experimentally obtained 3D microstructure with the simulated microstructures at various $(\varepsilon_1, \varepsilon_2)$ values, it seems reasonable to estimate the aniotropy parameters with this inverse analysis approach. However, comparing the three-dimensional microstructure requires a lot of information such as the growth direction, growth velocity, and concentration distribution of the system, thus it requires a lot of trial and error. Therefore, instead of a complex three-dimensional microstructure, information that extracts only the characteristics of the morphology is needed. Gibbs et al. [24] proposed a method to characterize three-dimensional morphology with an interfacial shape distribution (ISD) map as shown in Fig. 1.7 (b) using the statistical distribution of curvedness and shape factor of local morphology, which will be explained

in detail in Chapter 5.
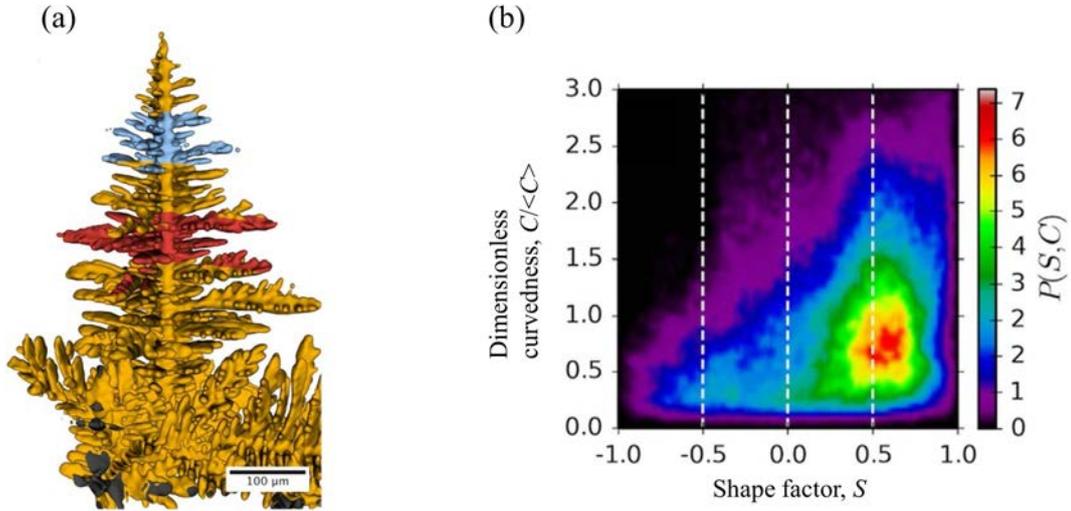
Fig. 1.7. (a) Three-dimensional growth morphology of Al-Cu alloy obtained by X-ray tomography. (b) corresponding interfacial shape distribution (ISD) map [24].

1.6   Purpose of this study

The morphology map of free dendrite growth serves as a basis for understanding of occurrence of various growth morphologies associated with diversity of PGD in equiaxed dendrite and also coulmanar dendrite [19]. It will offer useful information in controlling the solidification microstructures with use of the concentration dependence of anisotropy parameters. Therefore, further extensive investigations on the morphology map need to be carried out by extending the region of ε_1-ε_2 space and by classifying growth morphologies in more detail. Furthermore, the morphology map should depend on the solidification condition and the type of the alloy system. However, such dependencies have not been clarified yet.

Therefore, the purpose of this study is to construct the morphology map with high accuracy by conducting the extensive investigations of growth morphology of dendrite in ε_1-ε_2 space by means of quantitative phase-field simulations of fcc-based model alloy system. Moreover, it is also aimed to construct the morphology maps under different initial supersaturation and partition coefficients for equiaxed dendrite and the maps under different pulling speed and temperature gradient for columnar dendrite.

In addition, as an inverse analysis approach, a novel method to estimate anisotropy parameters of the alloy system using the ISD map will be proposed. The ISD maps for isothermally-soldified microsctructures associated with different set of ε_1 and ε_2 were obtained by the means of quantitative phase-field simulations. Then machine learning was applied to describe the relationship between the ISD map and a set of ε_1 and ε_2. The machine learning model allow the ε_1 and ε_2 to be estimated from a given ISD map.

1.7 Organization of this thesis

This thesis consists of six chapters and the organization is described below.

In chapter 2, details of quantitative phase-field model for solidification and the method to introducing anisotropy of solid-liquid interfacial energy into phase-field model are explained. In addition, phase-field model applied with nonlinear proconditioning [25] is explained.

In chapter 3, morphological diversity of equiaxed dendrite is described. Classification of growth morphology and the morphology map for different initial supersaturation and partition coefficient are explained. Computational conditions and acceleration methods will also be briefly described.

In chapter 4, morphological diversity of columnar dendrite is described. Classification of growth morphology and the morphology map for different solidification are explained.

In chapter 5, a method of estimating anisotropy parameters using inverse analysis is explained in detail, and the estimation results of isothermally-solidified microstructure is also described.

Finally, in chapter 6, the contributions and future prospectives of this study are summarized.

References

[1] W. Kurz, D. J. Fisher, Fundamentals of solidification, Vol. 1, Trans Tech Publications Aedermannsdorf, Switzerland, 1986.

[2] W. J. Boettinger, S. R. Coriell, A. Greer, A. Karma, W. Kurz, M. Rappaz, R. Trivedi, Solidification microstructures: recent developments, future directions, Acta materialia 48 (1) (2000) 43–70.

[3] J. A. Dantzig, M. Rappaz, Solidification, EPFL press, 2009.

[4] W. Kurz, D. J. Fisher, R. Trivedi, Progress in modelling solidification microstructures in metals and alloys: dendrites and cells from 1700 to 2000, International Materials Reviews 64 (6) (2019) 311–354.

[5] W. Kurz, M. Rappaz, R. Trivedi, Progress in modelling solidification microstructures in metals and alloys. part ii: dendrites from 2001 to 2018, International Materials Reviews 66 (1) (2021) 30–76.

[6] S. David, T. DebRoy, Current issues and problems in welding science, Science 257 (5069) (1992) 497–502.

[7] K. Pettersen, O. Lohne, N. Ryum, Dendritic solidification of magnesium alloy AZ91, Metallurgical Transactions A 21 (1) (1990) 221–230.

[8] M. Wang, T. Jing, B. Liu, Phase-field simulations of dendrite morphologies and selected evolution of primary α-Mg phases during the solidification of Mg-rich Mg–Al-based alloys, Scripta Materialia 61 (8) (2009) 777–780.

[9] T. Haxhimali, A. Karma, F. Gonzales, M. Rappaz, Orientation selection in dendritic evolution, Nature materials 5 (8) (2006) 660.

[10] M. Becker, J. Dantzig, M. Kolbe, S. T. Wiese, F. Kargl, Dendrite orientation transition in alge alloys, Acta Materialia 165 (2019) 666–677.

[11] L. Wang, J. J. Hoyt, N. Wang, N. Provatas, C. W. Sinclair, Controlling solid-liquid interfacial energy anisotropy through the isotropic liquid, Nature communications 11 (1) (2020) 1–7.

[12] Y. Okuda, Solute concentration dependence of preferred growth direction of dendrites in fcc solid solutions, Hokkaido university (2017).

[13] S. Shuai, E. Guo, Q. Zheng, M. Wang, T. Jing, Y. Fu, Three-dimensional α-Mg dendritic morphology and branching structure transition in Mg-Zn alloys, Materials Characterization 118 (2016) 304–308.

[14] M. Wang, Y. Xu, Q. Zheng, S. Wu, T. Jing, N. Chawla, Dendritic growth in Mg-based alloys: phase-field simulations and experimental verification by X-ray synchrotron tomography, Metallurgical and Materials Transactions A 45 (5) (2014) 2562–2574.

[15] J. Warren, Dendritic crystals: rule of thumb breaks down, Nature materials 5 (8) (2006) 595.

[16] S.-K. Chan, H.-H. Reimer, M. Kahlweit, On the stationary growth shapes of NH_4Cl dendrites, Journal of Crystal Growth 32 (3) (1976) 303–315.

[17] W. Fehlner, S. Vosko, A product representation for cubic harmonics and special directions for the determination of the fermi surface and related properties, Canadian Journal of Physics 54 (21) (1976) 2159–2169.

[18] M. Asta, C. Beckermann, A. Karma, W. Kurz, R. Napolitano, M. Plapp, G. Purdy, M. Rappaz, R. Trivedi, Solidification microstructures and solid-state parallels: Recent developments, future directions, Acta Materialia 57 (4) (2009) 941–971.

[19] J. Dantzig, P. Di Napoli, J. Friedli, M. Rappaz, Dendritic growth morphologies in Al-Zn alloys –PartII: phase-field computations, Metallurgical and Materials Transactions A 44 (12) (2013) 5532–5543.

[20] Z. Chen, E. Wang, X. Hao, Microstructure and orientation evolution in uni-directional solidified Al–Zn alloys, Materials Science and Engineering: A 667 (2016) 1–8.

[21] R. E. Napolitano, S. Liu, Three-dimensional crystal-melt wulff-shape and interfacial stiffness in the al-sn binary system, Physical Review B 70 (21) (2004) 214103.

[22] J. Hoyt, M. Asta, A. Karma, Method for computing the anisotropy of the solid-liquid interfacial free energy, Physical review letters 86 (24) (2001) 5530.

[23] R. L. Davidchack, B. B. Laird, Direct calculation of the hard-sphere crystal/melt interfacial free energy, Physical review letters 85 (22) (2000) 4751.

[24] J. Gibbs, K. A. Mohan, E. Gulsoy, A. Shahani, X. Xiao, C. Bouman, M. De Graef, P. Voorhees, The three-dimensional morphology of growing dendrites, Scientific reports 5 (1) (2015) 1–9.

[25] K. Glasner, Nonlinear preconditioning for diffuse interfaces, Journal of Computational Physics 174 (2) (2001) 695–711.

Chapter 2

Phase-field model

2.1   Introduction of phase-field model

The microstructure of materials is a geometric pattern formed by the different phases and concentration distribution. Features of microstructures formed after solidification such as size and morphology of solidified grains have a large influence on various properties of metallic materials [1–3]. Therefore, it is important to predict and control the solidification microstructures in production of high quality materials.

Diffusion of alloy element or latent heat and interfacial energy effect play an important role in the microstructure formation process [1, 4–6]. In case of alloy solidification, the growth morphology is determined by the competition and balance between diffusion effect and interfacial energy effect (Gibbs-Thomson effect) [4]. Thus, the interaction of diffusion and interfacial energy effect plays a key role in the formation of various microstructures during various transformation such as solid-state transformation, sintering and thin film growth and solidification [4,7].

For the past few decades, efforts have been devoted to understanding and predicting the microstructure by numerically solving the diffusion equation governing diffusion process and Gibbs-Thomson equation governing interfacial energy effect with a focus on dendritic growth process. However, most of them have centered on not quantitative but qualitative discussion of the microstructure. In 1990s, a phase-field model has emerged as a powerful method for calculating microstructure formation.

The fundamental idea of this method is as follows;

16

(1) Phase-field variable(s) ϕ is introduced. ϕ is a continuous variable defined in the whole system (see Fig. 2.1)

(2) The interface is defined as a region with finite thickness in which ϕ changes continuously (diffuse interface).

(3) Time evolution equation for ϕ, and diffusion field required for phenomena of interest are constructed. Then, relationships between the parameters in the equation and measurable quantities are established so that the equations converge to the Gibbs-Thomson equation and diffusion equation when the interface thickness is reduced.
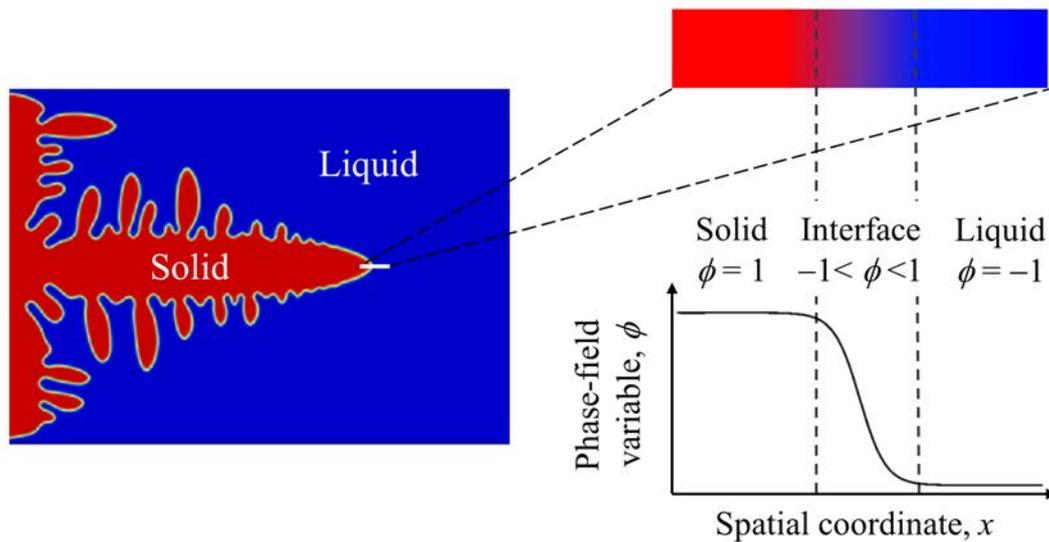
Fig. 2.1. Schematic representation of phase-field variable and diffuse interface.

The phase-field model is fundamentally different from the conventional methods for simulating microstructural models. In the conventional method, it is necessary to trace the interface when solving Gibbs-Thomson equation, which is difficult to calculate especially the shape of interface is complex. On the other hand, the phase-field model does not require tracking of the interface, since this model is based on the diffuse interface. Therefore, the phase-field model has the advantage in simulating a microstructural evolution with a complex interface morphology such as dendritic structure. Significant progresses have been made in modelling of solidification in materials including pure materials, binary alloys and multicomponent alloys. Thus, the phase-field model has been recognized as the most powerful tool to simulation the microstructure formation process since the 21st century [8–11].

In this chapter, the details of phase-field model for solidification phenomena will be explained. Fundamental equations for this model will be derived for pure substance and binary alloy solidification in the following sections.

2.2 Time-evolution equation

2.2.1 Fundamentals of phase-field model

The phase field equation used in the phase field model is based on the second law of thermodynamics that "the total free energy of the system monotonically decreases with time". Given the Helmholtz free energy of the whole system F, the second law of thermodynamics can be expressed as follows;

$$\frac{\partial F}{\partial t} = \int_V \frac{\delta F}{\delta \phi} \frac{\partial \phi}{\partial t} dv \leq 0 \tag{2.1}$$

In Eq. (2.1), the integral is a volume integral and ϕ indicates a state variable which can be classified as either the conserved or the non-conserved quantity. A typical example of the conserved quantity is the solute concertation which is often expressed as c. The phase-field variable which represents the probability of finding a phase corresponds to the non-conserved quantity.

Firstly, when ϕ is a non-conserved quantity, Eq. (2.1)can be satisfied by defining the time derivative of ϕ as follows;

$$\frac{\partial \phi}{\partial t} = -M_\phi \frac{\delta F}{\delta \phi} \tag{2.2}$$

where M_ϕ is positive constant. The relation in Eq. (2.2) is not the only solution that satisfies the Eq. (2.1), but always satisfies the Eq. (2.1) for any F and ϕ.

In case of conserved-quantity, Eq. (2.1) can be rewritten as follows.

$$\int_V \frac{\delta F}{\delta c} \frac{\partial c}{\partial t} dv \leq 0 \tag{2.3}$$

Note that the following conservation law always holds:

$$\frac{\partial c}{\partial t} = -\nabla \cdot \boldsymbol{J} \tag{2.4}$$

where $\boldsymbol{J}$ is flux. Substituting Eq. (2.4) into Eq. (2.3) and applying Gauss's divergence theorem, one finds the following equation.

$$
\begin{aligned}
\frac{\partial F}{\partial t} &= -\int_V \frac{\delta F}{\delta c} \nabla \cdot \boldsymbol{J} dv \\
&= -\int_S \frac{\delta F}{\delta c} \boldsymbol{J} ds + \int_V \boldsymbol{J} \cdot \left(\nabla \frac{\delta F}{\delta c}\right) dv \\
&= \int_V \boldsymbol{J} \cdot \left(\nabla \frac{\delta F}{\delta c}\right) dv \leq 0
\end{aligned}
\tag{2.5}
$$

Therefore, if the flux vector $\boldsymbol{J}$ satisfies the following relation, Eq. (2.5) always holds.

$$
\boldsymbol{J} = -L\nabla \frac{\delta F}{\delta c}
\tag{2.6}
$$

Here, L is a positive constant. And by substituting Eq. (2.5) into Eq. (2.4) one can find,

$$
\frac{\partial c}{\partial t} = \nabla \cdot \left(L\nabla \frac{\delta F}{\delta c}\right)
\tag{2.7}
$$

Equations (2.2) and (2.7) are time-evolution equations of non-conserved and conserved quantities, respectively.

2.2.2 Free energy of inhomogeneous system

The free energy of the entire system can be obtained by integrating the local free energy density over the entire system. Also, the local free energy density is considered as a function of local values of state variables and their spatial distribution . Then, the local free energy density can be expressed as follows,

$$
f = f\left(c, \nabla c, \nabla^2 c, \cdots\right)
\tag{2.8}
$$

Taylor expansion of Eq. (2.8) around homogeneous system is given as,

$$
\begin{aligned}
f\left(c, \nabla c, \nabla^2 c, \cdots\right) = f_0(c) &+ \sum_{i=1}^{3} L_i \frac{\partial c}{\partial x_i} + \sum_{i,j=1}^{3} \kappa_{ij}^{(1)} \frac{\partial^2 c}{\partial x_i \partial x_j} \\
&+ \frac{1}{2} \sum_{i,j=1}^{3} \kappa_{ij}^{(2)} \frac{\partial c}{\partial x_i} \frac{\partial c}{\partial x_j} + \cdots
\end{aligned}
\tag{2.9}
$$

19

where $f_0(c) = f(c, 0, 0, \cdots)$, $L_i = \partial f_0/\partial_{x_i}c$, $\kappa_{ij}^{(1)} = \partial f_0/\partial \left(\partial_{x_i x_j}c\right)$, and $\kappa_{ij}^{(2)} = \partial^2 f_0/\partial \left(\partial_{x_i}c\right)\partial \left(\partial_{x_j}c\right)$, also x_i denotes conventional Cartesian coordinates. Furthermore, the four-fold symmetric property of cubic crystal, which is our main concern in this study, yields the following relations,

$$
\begin{aligned}
f(x_i) &= f(-x_i) & c(x_i) &= c(-x_i) \\
\left.\frac{\partial c}{\partial x_i}\right|_{x_i} &= -\left.\frac{\partial c}{\partial x_i}\right|_{-x_i} & L_i(x_i) &= L_i(-x_i)
\end{aligned}
$$

Substituting these relationships into Eq. (2.9) yields the following equation).

$$
\begin{aligned}
f_0\left(c(x_k)\right) &+ \sum_{i=1}^{3} L_i(x_k)\frac{\partial c(x_k)}{\partial x_i} + \sum_{i,j=1}^{3} \kappa_{ij}^{(1)}(x_k)\frac{\partial^2 c(x_k)}{\partial x_i \partial x_j} \\
&+ \frac{1}{2}\sum_{i,j=1}^{3} \kappa_{ij}^{(2)}(x_k)\frac{\partial c(x_k)}{\partial x_i}\frac{\partial c(x_k)}{\partial x_j} \\
= f_0\left(c(-x_k)\right) &+ \sum_{i=1}^{3} L_i(-x_k)\frac{\partial c(-x_k)}{\partial x_i} + \sum_{i,j=1}^{3} \kappa_{ij}^{(1)}(-x_k)\frac{\partial^2 c(-x_k)}{\partial x_i \partial x_j} \\
&+ \frac{1}{2}\sum_{i,j=1}^{3} \kappa_{ij}^{(2)}(-x_k)\frac{\partial c(-x_k)}{\partial x_i}\frac{\partial c(-x_k)}{\partial x_j}
\end{aligned}
\tag{2.10}
$$

where $k = 1, 2$ and 3. From Eq. (2.10) $L_i(x_k)\partial c(x_k)/\partial x_i$ becomes 0, and in order to satisfy this relationship, $L_i(x_k)$ should be 0, thus, $L_1 = L_2 = L_3 = 0$. Also, a tensor that represents the cubic crystal symmetry can be represented as a unit matrix, then $\kappa^{(1)}$ and $\kappa^{(2)}$ can be expressed as follows.

$$
\kappa^{(1)} = \begin{pmatrix} \kappa_1 & 0 & 0 \\ 0 & \kappa_1 & 0 \\ 0 & 0 & \kappa_1 \end{pmatrix} \qquad \kappa^{(2)} = \begin{pmatrix} \kappa_2 & 0 & 0 \\ 0 & \kappa_2 & 0 \\ 0 & 0 & \kappa_2 \end{pmatrix}
\tag{2.11}
$$

By substituting $L_i = 0$ and Eq. (2.11) into Eq. (2.9) and dropping higher order terms, the free energy density can be expressed as follows.

$$
f\left(c, \nabla c, \nabla^2 c\right) = f_0(c) + \kappa_1 \nabla^2 c + \kappa_2|\nabla c|^2
\tag{2.12}
$$

Also, from this free energy density in Eq. (2.12), the free energy of the entire system can be obtained as follows.

$$F = \int_V \left[f_0(c) + \kappa_1 \nabla^2 c + \kappa_2 |\nabla c|^2 \right] dv \tag{2.13}$$

By rewriting the second term of integrand function by Gauss's divergence theorem as follows,

$$\int_V \kappa_1 \nabla^2 c \, dv = \int_S \kappa_1 \left(\nabla c \cdot \boldsymbol{n} \right) ds - \int_V \frac{\partial \kappa_1}{\partial c} |\nabla c|^2 dv = - \int_V \frac{\partial \kappa_1}{\partial c} |\nabla c|^2 dv$$

the free energy of the inhomogeneous system can be finally expressed by Eq. (2.14)

$$F = \int_V \left[f_0(c) + \frac{1}{2} \varepsilon_c^2 |\nabla c|^2 \right] dv \tag{2.14}$$

where ε_c is given as $\varepsilon_c^2 = 2(\kappa_2 - \partial \kappa_1 / \partial c)$. In Eq. (2.14), the first term of integrand is the local free energy density of homogeneous system and the second term is proportional to the gradient of the conserved variables and it is called the gradient energy. ε_c is the gradient energy coefficient usually assumed constant.

Furthermore, the free energy can be derived for the non-conserved quantity in the same way as follows,

$$F = \int_V \left[f_0(\phi) + \frac{1}{2} \varepsilon_\phi^2 |\nabla \phi|^2 \right] dv \tag{2.15}$$

The free energy functional shown in Eqs. (2.14) and (2.15) is called Ginzburg-Landau type free energy.

2.2.3   Functional derivative and phase-field equation

The function $f(x)$ means a relationship that maps a number x, such as a real number or a complex number, to another number.

On the other hand, as shown in Eqs. (2.14) and (2.15) a function can also have a function in the domain, instead of a real number or a complex number in the domain. This kind of relationship is called functional. In this case, the free energy F is functional of c and ϕ and it depends on c, ∇c, ϕ and $\nabla \phi$. Our

main concern is to find c and ϕ that minimize the functional F. To find this, variational derivative method (or functional derivative) is need. The details are explained in some references [12–15] and here, we discuss only the derivation of phase-field equation using variational derivative method.

Next, the process of obtaining functional derivative $\delta F/\delta \phi$ will be described. Functional can be expressed as $F = \int_v f(\phi, \nabla \phi) dv$ from Eq. (2.15), then the functional derivative of F can be written as follows.

$$\frac{\delta F}{\delta \phi} = \frac{\partial f}{\partial \phi} - \nabla \cdot \frac{\partial f}{\partial (\nabla \phi)} \qquad (2.16)$$

The second term of the right side of Eq. (2.16) is expressed as follows.

$$\nabla \cdot \frac{\partial f}{\partial (\nabla \phi)} = \frac{\partial}{\partial x}\left(\frac{\partial f}{\partial_x \phi}\right) + \frac{\partial}{\partial y}\left(\frac{\partial f}{\partial_y \phi}\right) + \frac{\partial}{\partial z}\left(\frac{\partial f}{\partial_z \phi}\right) \qquad (2.17)$$

By applying this variational derivative formula into the free energy functional (2.14) and (2.15), then substituting into time-evolution equations (2.2) and (2.7), time-evolution equations of non-conserved and conserved quantity are obtained.

$$\frac{\partial \phi}{\partial t} = -M_\phi \left(\frac{\partial f_0}{\partial \phi} - \varepsilon_\phi^2 \nabla^2 \phi\right) \qquad (2.18)$$

$$\frac{\partial c}{\partial t} = L \nabla^2 \left(\frac{\partial f_0}{\partial c} - \varepsilon_c^2 \nabla^2 c\right) \qquad (2.19)$$

Equations (2.18) and (2.19) are refer as Allen-Cahn equation and Cahn-Hilliard equation, respectively.

In addition, the local free energy of the homogeneous system can be expressed as follows.

$$f_0(\phi) = f_{dw}(\phi) + f_{bulk}(\phi) \qquad (2.20)$$

$f_{dw}(\phi)$ is a term representing the free energy barrier between different phases (such

as solid and liquid phases) and it is usually described by following form:

$$f_{dw}(\phi) = \omega\phi^2 \left(1 - \phi^2\right) \tag{2.21}$$

where ω is constant and $f_{dw}(\phi)$ is a function that takes the minimum value when $\phi = 0, 1$, at the bulk phase. That is, it is a function that contributes to an increase in the free energy when the system does take bulk phase, i.e. interface of different phases.

The second term of Eq. (2.20) is a term contributing to bulk free energy. Given that f_s and f_l denote the local free energy of the homogeneous system of the solid and liquid phase, respectively, $f_{bulk}(\phi)$ is a function that satisfy $f_{bulk}(0) = f_l$ (liquid phase) and $f_{bulk}(1) = f_s$ (solid phase). This kind of bulk free energy is usually expressed by following form,

$$f_{bulk}(\phi) = g(\phi)f_S + (1 - g(\phi))f_L \tag{2.22}$$

where $g(\phi)$ monotonically increasing function, the form of which is often given by the fifth order polynomial $g(\phi) = \phi^3(10 - 15\phi + 6\phi^2)$. Substituting the relationships in equations (2.20)-(2.22) into the Allen-Cahn equation, the time-evolution equation of phase-field variable (the phase-field equation) can be obtained as follows,

$$\frac{1}{M_\phi}\frac{\partial\phi}{\partial t} = \varepsilon^2\nabla^2\phi - \frac{df_{dw}(\phi)}{d\phi} - \frac{dg(\phi)}{d\phi}\left(f_s - f_l\right) \tag{2.23}$$

2.3 Phase-field model for solidification of pure substance

In solidification of pure substance, the morphology of the solid-liquid interface is determined by the heat diffusion related to release of latent heat due to solidification. If the temperature of the liquid phase is higher than melting point and the temperature of the solid phase is maintained lower than melting point, the latent heat from the S-L interface releases only toward the solid phase. In this situation, the S-L interface always maintains a flat morphology. However, if the temperature of the liquid is lower than melting point and the solidification begins from

inside the liquid phase, the latent heat must release toward liquid phase. In this situation, the flat interface becomes morphologically unstable and forms a complex geometric pattern called dendritic morphology. The growth rate of dendrite is a function of the degree of undercooling. Numerous studies of dendritic growth have been conducted since the 1950s and, importantly, the micro-solvability theory which is consistent with experiments, was constructed around 1990 [16–18]. In addition to the theoretical studies, numerical studies of dendritic growth have been continued and three-dimensional computational simulation of dendritic growth have been successfully carried out by Kobayashi around 1990 [8]. The numerical method of Kobayashi's study is the phase-field model.

2.3.1 Sharp interface model for solidification of pure substance

When the solid-liquid interface is regarded as a mathematical surface with a thickness of zero, solidification of pure substance is dominated by the heat conduction (or diffusion) in the bulk solid and liquid phase, the energy conservation law at the interface and Gibbs-Thomson effect. If the temperature of an arbitrary point in the system is T, the heat diffusion inside the system is expressed by following equation:

$$\frac{\partial T}{\partial t} = D_T \nabla^2 T \tag{2.24}$$

where D_T is heat diffusion coefficient given by $D_T = k_t/c_p$ and c_p is specific heat and k_t thermal conductivity.

At the S-L interface, two conditions must be satisfied. The first one is the condition that latent heat released by solidification must be equal to the amount of heat energy that escapes from the interface to bulk phases, i.e. the energy conservation law at the interface. This law is expressed as follows:

$$v_n \Delta H = k_T \left(\frac{\partial T}{\partial n} \right)_S - k_T \left(\frac{\partial T}{\partial n} \right)_L \tag{2.25}$$

where v_n is the velocity of S-L interface, H is the solidification latent heat and

$(\partial T)/\partial n)_S$ and $(\partial T)/\partial n)_L$ are the temperature gradient normal to the S-L interface at the solid and liquid sides, respectively.

The second condition for the interface is Gibbs-Thomson effect. If the interface is planar and it does not move, the temperature of the interface should be the equilibrium melting point, T_m. If the interface has an arbitrary curvature κ, the interface temperature should be lowered by $\Delta T_R = (T_m^e/\Delta T)\sigma\kappa$. ΔT_R is called the curvature undercooling. If the interface is moving at the speed of v_n, the atoms must leap from the liquid to solid phase and this process requires proper driving force. The driving force related to the leap of atoms is called kinetic undercooling, represented as ΔT_k. However, this kinetic undercooling can be neglected when the speed of interface is low, such as the solidification process of metallic materials. In this case, it is said that local equilibrium condition is satisfied at the interface. In the general case where the effects of ΔT_R and ΔT_k are exist, the temperature at the interface, T_i can be expressed as follows:

$$T_i = T_m^e - \frac{T_m^e}{\Delta H}\sigma\kappa - \beta_k v_n \tag{2.26}$$

where σ is the interface energy and β_k is the interface kinetic coefficient. Equations (2.24)-(2.26) are governing equations of the solidification process of pure substance. All the information about the interface velocity, temperature distribution and the morphological change of interface can be obtained by solving these equations. However, it is very difficult to solve these equations accurately in a numerical way as well as analytical method. In fact, the easiest and most accurate way to solve these equations is to use the phase-field model. In the next subsection, it will be explained that how to construct phase-field model corresponding above equations (2.24)-(2.26).

2.3.2 Phase-field model for solidification of pure substance

The phase-field model for solidification of pure substance consists of phase-field equation (2.23) and heat diffusion equation with release of the latent heat. Since the free energy difference between the solid and the liquid phases, $(f_s - f_l)$ is approximated as $\Delta(T_i - T_m^e)/T_m^e$, governing equations of phase-field model can be rewritten

as follows:

$$\frac{1}{M_\phi}\frac{\partial \phi}{\partial t} = \varepsilon^2 \nabla^2 \phi - \omega q'(\phi) - g'(\phi)\frac{\Delta H}{T_m^e}(T_i - T_m^e) \tag{2.27}$$

where $q(\phi) = \phi^2(1-\phi^2)$ and $g(\phi) = \phi^3(10 - 15\phi + 6\phi^2)$. Heat diffusion equation with release of the latent heat can be expressed as follows.

$$\frac{\partial T}{\partial t} = D_T \nabla^2 T + \frac{\Delta H}{C_p}\frac{dg(\phi)}{dt} \tag{2.28}$$

The second term on the right side of Eq. (2.28) indicates the rate of temperature change due to the release of the latent heat. In bulk solid and bulk liquid phases, the last term of Eq. (2.28) disappears and it becomes equivalent to Eq. (2.24). Also, if the thickness of the interface is sufficiently thin and the parameters in the phase-field equation are determined appropriately, Eqs. (2.27) and (2.28) can reproduce Eqs. (2.25) and (2.26).

2.3.3 Relationship between physical parameters

At the equilibrium state, there is no time change of the phase-field variable which means that $\partial \phi/\partial t = 0$. In case of pure substance, also, the condition $f_s = f_l$ holds at the equilibrium. When the normal direction to the interface is described as x and boundary condition of $\phi = 0$ at $x \to \infty$ and $\phi = 1$ at $x \to -\infty$ is considered, the solution of the phase-field equation(2.27) is given as

$$\phi(x) = \frac{1}{2}\left[1 - \tanh\left(\frac{x}{\sqrt{2}W}\right)\right] \tag{2.29}$$

where $W = \varepsilon/\sqrt{\omega}$, and the profile of $\phi(x)$ changes depending on the size of W. Therefore, W is a measure of interface width. Although the detailed procedure is omitted here, the interfacial energy, γ and the phase-field mobility, M_ϕ can be obtained as follows through the analysis of the non-equilibrium state.

$$\gamma = \frac{1}{3\sqrt{2}}\varepsilon\sqrt{\omega} \tag{2.30}$$

$$M_\phi = \frac{\omega C_p T_m D_T}{\varepsilon^2 \Delta H^2} \tag{2.31}$$

2.4   Phase-field model for solidification of alloy

2.4.1   Sharp interface model for solidification of alloy

In the solidification process of alloys, in addition to the heat diffusion and migration of the interface, the diffusion of solute atoms occurs. Since the diffusion of atom is significantly slower than the diffusion of heat, the rate of solidification in alloys is usually controlled by the diffusion of solute atoms.

Solidification process of the alloy, as is similar to pure substance, is governed by the solute diffusion in bulk phase, mass conservation law of solute atoms at the interface and the Gibbs-Thomson law. These laws can be expressed by Eqs. (2.32)-(2.35).

$$\frac{\partial c}{\partial t} = \nabla \cdot (D_s \nabla c) \tag{2.32}$$

$$\frac{\partial c}{\partial t} = \nabla \cdot (D_l \nabla c) \tag{2.33}$$

$$v_n \left(c_l^e - c_s^e \right) = D_s \frac{\partial c_s}{\partial n} - D_l \frac{\partial c_l}{\partial n} \tag{2.34}$$

$$T_l^k = T_l^e - |m_l| c_l^e - \frac{T_m^e \gamma \kappa}{\Delta H} - \beta_k v_n \tag{2.35}$$

In the next subsection, we will describe the procedures of constructing phase-field and solute diffusion equations satisfying the above free boundary problem (Eqs. (2.32)-(2.35)).

2.4.2   KKS model

In the model which is most frequently used model for alloy solidification, the homogeneous free energy of the bulk solid and bulk liquid phase are expressed as functions of solute concentration, $f_s = f_s(c, T)$ and $f_l = f_l(c, T)$, respectively. The phase-field variable ϕ and solute concentration field c are made mutually dependent. Note that the equilibrium condition of alloy is not $f_s = f_l$, but $\mu_s = \mu_l$ where μ_i is the chemical potential of i phase. Therefore, even in the equilibrium state, the third term on the right side of Eq. (2.18) does not become 0, then it ϕ profile becomes dependent on the concentration. Therefore, the interface width W can not be determined in advance. Furthermore, the grid size of the calculation needs to be smaller than the

interface width, and, hence, the calculation efficiency depends on the concentration profile. As a result, the efficiency of calculation becomes extremely poor. A model free from this problem was proposed by Kim, Kim and Suzuki [19], and this model is usually called KKS model. In KKS model, the solute concentrations of solid (c_s) and liquid phase (c_l) are defined in the whole system regardless of occupied phase and the alloy concentration is defined as follows:

$$c = h(\phi)c_s + (1 - h(\phi))\,c_l \tag{2.36}$$

where $h(\phi)$ is monotonically increasing function with respect to ϕ and $h(\phi) = \phi$ is often used. Furthermore, in this model, it is assumed that the chemical potential (more precisely, diffusion potential) of the solid and liquid phase is equal at each spatial point as follows.

$$\mu_c = \frac{\partial f_s}{\partial c_s} = \frac{\partial f_l}{\partial c_l} \tag{2.37}$$

By considering Eqs. (2.36) and (2.37) and by performing variational derivative of free energy function, time-evolution equation of ϕ can be expressed as follows.

$$\frac{1}{M_\phi}\frac{\partial \phi}{\partial t} = \varepsilon^2 \nabla^2 \phi - \frac{df_{dw}(\phi)}{d\phi} - \frac{dg(\phi)}{d\phi}\left(f_s - f_l - \mu(c_s - c_l)\right) \tag{2.38}$$

Comparing Eq. (2.18) with (2.38), we can see that driving force term is modified. In the phase-field equation(2.38), the third term on the right side becomes 0 in the equilibrium state and this equilibrium profile of ϕ becomes equal to Eq. (2.29) in which the concentration dependence of ϕ profile disappears. Also, the time-evolution equation of c is expressed as follows:

$$\frac{\partial c}{\partial t} = \nabla \cdot (D(\phi)\nabla c) + \nabla \cdot (D(\phi)(c_l - c_s)\nabla \phi) \tag{2.39}$$

where $D(\phi)$ is diffusion coefficient satisfying $D(\phi = 1) = D_s$ and $D(\phi = 0) = D_l$.

2.4.3 Quantitative model

The KKS model had been widely used in the simulation of alloy solidification and its effectiveness had been verified. However, it is known that the phase-field model for alloy solidification including KKS model has a problem in the accuracy of the simulation result. That is, the result depends on the value of the interface width W which is an arbitrary constant. Although the actual solid-liquid interface width is on the order of several nm, the interface width used in phase-field simulation is several tens of μm. In the alloy model, then, solute trapping phenomenon occurs. Solute trapping phenomenon indicates that solute atoms that had to be transferred from the solid phase to the liquid phase cannot be sufficiently transferred by overestimating the interface width and be captured in the solid phase region.

Karma et al. introduced a quantitative phase-field model that solved this solute trapping phenomenon by artificially introducing an anti-trapping current which pushes the solute toward the liquid phase side [16, 20, 21]. In the Karma's model, the diffusion in the solid phase is neglected, since solute diffusion at the solid phase is much slower than that of liquid in most of the alloy solidification. However, solute atoms such as carbon in steel materials diffuse very rapidly in the solid phase. Ohno et al. proposed the quantitative phase-field model considering diffusion within the solid phase which is applicable to any kinds of alloy system [22]. In this study, I performed simulations by using Ohno's model [22] using dilute binary alloy approximation and this model will be explained below.

First of all, to simplify the mathematical calculation, we redefine the variables and summarize the expressions necessary for this calculation. The phase-field variable is rewritten as p, and it is defined that solid phase when $p = 1$ and liquid phase when $p = 0$. Then free energy functional can be rewritten as follows:

$$F = \int_V \left[\frac{\widetilde{\sigma}}{2} |\nabla p|^2 + \widetilde{\omega}\widetilde{f}(p) + \widetilde{g}(p)f_s + (1 - \widetilde{g}(p)) f_l \right] dv \qquad (2.40)$$

where $\widetilde{\sigma}$ is gradient energy coefficient, $\widetilde{f}(p)$ is double-well potential, $\widetilde{\omega}$ is constant and $\widetilde{g}(p)$ is monotonically increasing function of p. Also, the alloy concentration can

be rewritten as follows:

$$c = \widetilde{h}(p)c_s + \left(1 - \widetilde{h}(p)\right)c_l \qquad (2.41)$$

where $\widetilde{h}(p)$ is monotonically increasing function of p. From these relationships, we can rewrite time-evolution equation of KKS model (Eqs. (2.38) and (2.39)) as follows:

$$\frac{1}{\widetilde{M}}\frac{\partial p}{\partial t} = \widetilde{\sigma}^2\nabla^2 p - \widetilde{\omega}\widetilde{f}' - \widetilde{g}'\left[f_s(c_s) - f_l(c_l) - (c_s - c_l)\mu_c\right] \qquad (2.42)$$

$$\frac{\partial c}{\partial t} = \nabla D(p)\left[\widetilde{h}(p)\nabla c_s + \left(1 - \widetilde{h}(p)\right)\nabla c_l\right] \qquad (2.43)$$

where $\widetilde{M}$ is phase-field mobility, $\widetilde{f}'(p) = d\widetilde{f}/dp$, $\widetilde{g}'(p) = d\widetilde{g}/dp$, $D(p)$ is diffusion coefficient satisfying $D(p = 1) = D_s$ and $D(p = 0) = D_l$. And interpolation functions are defined as, $\widetilde{f}(p) = p^2(1 - p)^2$, $\widetilde{g}(p) = p^3(10 - 15p + 6p^2)$ and $\widetilde{h}(p) = p$. Then, the phase-field variable ϕ can be redefined as $\phi = 2p - 1$. Solid and liquid phase correspond to $\phi = 1$ and $\phi = -1$, respectively. In addition, the dimensionless supersaturation u is defined as $u = (c_l - c_l^e)/(c_l^e - c_s^e)$. The driving force of solidification can be approximated as follows by using dilute binary approximation.

$$f_c(c_s) - f_l(c_l) - (c_s - c_l)\mu c \approx -\frac{RT_0}{v_m}\left[c_l^e - c_s^e - (c_l - c_s)\right]$$
$$\approx -\frac{RT_m}{v_m}\left[c_l^e - c_s^e - (c_l - c_s)\right] \qquad (2.44)$$

By using this approximation and introducing anti-trapping current, $\boldsymbol{J}_{at}$, we can rewrite Eqs. (2.42) and (2.43) as equation of ϕ and u as follows:

$$\frac{1}{M}\frac{\partial\phi}{\partial t} = \sigma^2\nabla^2\phi - 2\omega\widetilde{f}' - \widetilde{g}'\lambda u \qquad (2.45)$$

$$\frac{[1 + k - (1 - k)h(\phi)]}{2}\frac{\partial u}{\partial u} = \nabla \cdot [D_l q(\phi)\nabla u - \boldsymbol{J}_{at}] + \frac{1}{2}[1 + (1 - k)u]\frac{\partial h(\phi)}{\partial t} \qquad (2.46)$$

where M, σ, ω are expressed as $M = 4\widetilde{M}$, $\sigma = \widetilde{\sigma}/2$ and $\omega = \widetilde{\omega}/4$. Also, the coupling

constant λ is $\lambda = RT_m(1-k)(c_l^e - c_s^e)/2v_m$ and $h(\phi)$ and $q(\phi)$ are expressed as $h(\phi) = 2\widetilde{h}(p) - 1$ and $q(\phi) = [1 + k - (1-k)h(\phi)]/2$. The phase-field mobility by thin-interface analysis is given as follows.

$$\frac{1}{M} = \frac{W^2}{D_l}\frac{15a_2}{16}\frac{RT_m}{v_m}(1-k)(c_l^e - c_s^e) \tag{2.47}$$

The anti-trapping current, $\boldsymbol{J}_{at}$ has the same direction as the normal vector of S-L interface, and it is expressed as follows, which is proportional to the time change of phase-field variable.

$$\boldsymbol{J}_{at} = -a(\phi)\frac{\sigma}{\sqrt{\omega}}[1 + (1-k)u]\frac{\partial\phi}{\partial t}\frac{\nabla\phi}{|\nabla\phi|} \tag{2.48}$$

If we change some variables as follows, $\tau = 1/M\omega$, $W^2 = \sigma^2/\omega$, $\lambda^* = 15\lambda/8\omega$, $f' = 2\widetilde{f}'$ and $g' = 8\widetilde{g}'/15$, the phase-field equation (2.45) and diffusion equation (2.46) cad be expressed as follows.

$$\tau\frac{\partial\phi}{\partial t} = W^2\nabla^2\phi - f'(\phi) - \lambda^*g'(\phi)u \tag{2.49}$$

$$\frac{[1 + k - (1-k)h(\phi)]}{2}\frac{\partial u}{\partial t} = \nabla\cdot\left(D_l q(\phi)\nabla u\right.$$
$$+ a(\phi)\frac{\sigma}{\sqrt{\omega}}[1 + (1-k)u]\frac{\partial\phi}{\partial t}\frac{\nabla\phi}{|\nabla\phi|}\left.\right)$$
$$+ \frac{1}{2}[1 + (1-k)u]\frac{\partial h(\phi)}{\partial t} \tag{2.50}$$

And $a(\phi)$ and $\psi(\chi)$ satisfy following relationships:

$$a(\phi) = \frac{1}{2\sqrt{2}}\left(1 - k\frac{D_s}{D_l}\right)\psi(\chi) \tag{2.51}$$

$$\psi(\chi) = 1 - \frac{1}{2}\left(1 - k\frac{D_s}{D_l}\right)\chi \tag{2.52}$$

where χ was set to 0 in this study. Equations (2.49) and (2.50) are the final form of quantitative phase-field model for isothermal solidification that considers diffusion in solid phase proposed by Ohno et al. [22]. By solving these two equations, the solidification process of binary alloy can be simulated with high accuracy.

2.5 Anisotropic property of solid-liquid interfacial energy

The phase-field models for solidification of pure substance and binary alloy, described up to previous section, assumed that the S-L interfacial energy is isotropic. In order to simulate the dendritic growth correctly, it is necessary to consider the anisotropic property of interfacial energy. In this study, I constructed a model by using interfacial energy considering cubic symmetry in three-dimension. It can be expressed as follows [23, 24]:

$$\gamma(\boldsymbol{n}) = \gamma_0 \left[1 + \varepsilon_1 \left(Q(\boldsymbol{n}) - \frac{3}{5} \right) + \varepsilon_2 \left(3Q(\boldsymbol{n}) + 66S(\boldsymbol{n}) - \frac{17}{7} \right) \right] = \gamma_0 a_s(\boldsymbol{n}) \quad (2.53)$$

where $\boldsymbol{n} = (n_x, n_y, n_z)$ is unit vector of interfacial normal, $Q(\boldsymbol{n}) = n_x^4 + n_y^4 + n_z^4$, $S(\boldsymbol{n}) = n_x^2 n_y^2 n_z^2$, ε_1 and ε_2 are anisotropy parameters. Also, in the quantitative model used in this study, since interface width W is proportional to gradient energy, anisotropy is introduced as $W(\boldsymbol{n}) = W_0 a_s(\boldsymbol{n})$, where W_0 is average interface width. Then, the modified phase-field equation can be expressed as follows:

$$\begin{aligned}
\tau(\boldsymbol{n}) \frac{\partial \phi}{\partial t} &= \nabla \cdot \left(W^2(\boldsymbol{n}) \nabla \phi \right) \\
&+ \sum_{s=x,y,z} \frac{\partial}{\partial s} \left(|\nabla \phi|^2 W(\boldsymbol{n}) \frac{\partial W(\boldsymbol{n})}{\partial(\partial_s \phi)} \right) \\
&- f'(\phi) - \lambda^* g'(\phi) u
\end{aligned} \quad (2.54)$$

where $\tau(\boldsymbol{n}) = \tau_0 a_s^2(\boldsymbol{n})$, $\tau_0 = a_2 W_0^2 \lambda^* [1 + (1 - k)u_0]/D_l$, $a_2 = 0.6272$ and u_0 is initial dimensionless supersaturation. To make Eq. (2.54) suitable for numerical simulation, the first and the second term on the right side of Eq. (2.54) can be

expanded as follows.

$$\tau(\boldsymbol{n})\frac{\partial \phi}{\partial t} = W(\boldsymbol{n})^2 \nabla^2 \phi + 2W(\boldsymbol{n}) \sum_{r,s=x,y,z} \frac{\partial W(\boldsymbol{n})}{\partial(\partial_s \phi)}(\partial_{sr}\phi)(\partial_r \phi)$$

$$+ \sum_{s=x,y,z} \left(2W(\boldsymbol{n})\frac{\partial W(\boldsymbol{n})}{\partial(\partial_s \phi)} \sum_{r=x,y,z} (\partial_r \phi)(\partial_{rs}\phi) \right.$$

$$+ |\nabla \phi|^2 \frac{\partial W(\boldsymbol{n})}{\partial(\partial_s \phi)} \sum_{r=x,y,z} \frac{\partial W(\boldsymbol{n})}{\partial(\partial_r \phi)}(\partial_{rs}\phi) \qquad (2.55)$$

$$+ |\nabla \phi|^2 W(\boldsymbol{n}) \sum_{r=x,y,z} \frac{\partial^2 W(\boldsymbol{n})}{\partial(\partial_s \phi)\partial(\partial_r \phi)}(\partial_{rs}\phi) \Bigg)$$

$$+ f'(\phi) - \lambda^* g'(\phi)u$$

In order to perform the simulation using Eq. (2.55), it is necessary to calculate $\partial W(\boldsymbol{n})/\partial(\partial_s \phi)$ and $\partial^2 W(\boldsymbol{n})/\partial(\partial_s \phi)\partial(\partial_r \phi)$, and have to express by using $\partial_x \phi$, $\partial_y \phi$ and $\partial_z \phi$.

First of all, derivative of $W(\boldsymbol{n})$ with $\partial_x \phi$, $\partial_y \phi$ and $\partial_z \phi$ can be expressed as follows.

$$\frac{\partial W(\boldsymbol{n})}{\partial(\partial_s \phi)} = W_0 \left[(\varepsilon_1 + 3\varepsilon_2)\frac{\partial Q(\boldsymbol{n})}{\partial(\partial_s \phi)} + 66\varepsilon_2 \frac{\partial S(\boldsymbol{n})}{\partial(\partial_s \phi)} \right] \qquad (2.56)$$

$$\frac{\partial^2 W(\boldsymbol{n})}{\partial(\partial_s \phi)\partial(\partial_r \phi)} = W_0 \left[(\varepsilon_1 + 3\varepsilon_2)\frac{\partial^2 Q(\boldsymbol{n})}{\partial(\partial_s \phi)\partial(\partial_r \phi)} + 66\varepsilon_2 \frac{\partial^2 S(\boldsymbol{n})}{\partial(\partial_s \phi)\partial(\partial_r \phi)} \right] \qquad (2.57)$$

$Q(\boldsymbol{n})$ and $S(\boldsymbol{n})$ can be expressed as follows.

$$Q(\boldsymbol{n}) = \frac{(\partial_x \phi)^4 + (\partial_y \phi)^4 + (\partial_z \phi)^4}{[(\partial_x \phi)^2 + (\partial_y \phi)^2 + (\partial_z \phi)^2]^2} \qquad (2.58)$$

$$S(\boldsymbol{n}) = \frac{(\partial_x \phi)^2(\partial_y \phi)^2(\partial_z \phi)^2}{[(\partial_x \phi)^2 + (\partial_y \phi)^2 + (\partial_z \phi)^2]^3} \qquad (2.59)$$

Then, the partial derivatives of $Q(\boldsymbol{n})$ and $S(\boldsymbol{n})$ are expressed as follows.

$$\frac{\partial Q(\boldsymbol{n})}{\partial(\partial_s \phi)} = \frac{4(\partial_s \phi)^4}{\left(\sum_r (\partial_r \phi)^2 \right)^2} - \frac{4(\partial_s \phi)\sum_r (\partial_r \phi)^4}{\left(\sum_r (\partial_r \phi)^2 \right)^3} \qquad (2.60)$$

$$\frac{\partial^2 Q(\boldsymbol{n})}{\partial(\partial_s\phi)^2} = \frac{12(\partial_s\phi)^2}{\left(\sum_r (\partial_r\phi)^2\right)^2} - \frac{4\sum_r (\partial_r\phi)^4}{\left(\sum_r (\partial_r\phi)^2\right)^3}$$
$$- \frac{32(\partial_s\phi)^4}{\left(\sum_r (\partial_r\phi)^2\right)^3} + \frac{24(\partial_s\phi)^2\sum_r (\partial_r\phi)^4}{\left(\sum_r (\partial_r\phi)^4\right)^4} \qquad (2.61)$$

$$\frac{\partial^2 Q(\boldsymbol{n})}{\partial(\partial_s\phi)\partial(\partial_r\phi)} = -\frac{16(\partial_s\phi)(\partial_r\phi)\left[(\partial_s\phi)^2 + (\partial_r\phi)^2\right]}{\left(\sum_r (\partial_r\phi)^2\right)^3} + \frac{24(\partial_s\phi)(\partial_r\phi)\sum_r (\partial_r\phi)^4}{\left(\sum_r (\partial_r\phi)^4\right)^4} \quad (2.62)$$

$$\frac{\partial S(\boldsymbol{n})}{\partial(\partial_s\phi)} = \frac{2(\partial_s\phi)(\partial_r\phi)^2(\partial_t\phi)^2}{\left(\sum_r (\partial_r\phi)^2\right)^3} - \frac{6(\partial_s\phi)^3(\partial_r\phi)^2(\partial_t\phi)^2}{\left(\sum_r (\partial_r\phi)^2\right)^4} \qquad (2.63)$$

$$\frac{\partial^2 S(\boldsymbol{n})}{\partial(\partial_s\phi)^2} = \frac{2(\partial_r\phi)^2(\partial_t\phi)^2}{\left(\sum_r (\partial_r\phi)^2\right)^3} - \frac{30(\partial_s\phi)^2(\partial_r\phi)^2(\partial_t\phi)^2}{\left(\sum_r (\partial_r\phi)^2\right)^4} + \frac{48(\partial_s\phi)^4(\partial_r\phi)^2(\partial_t\phi)^2}{\left(\sum_r (\partial_r\phi)^2\right)^5} \quad (2.64)$$

$$\frac{\partial^2 S(\boldsymbol{n})}{\partial(\partial_s\phi)\partial(\partial_r\phi)} = \frac{4(\partial_r\phi)(\partial_s\phi)(\partial_t\phi)^2}{\left(\sum_r (\partial_r\phi)^2\right)^3} - \frac{12(\partial_r\phi)^3(\partial_s\phi)(\partial_t\phi)^2}{\left(\sum_r (\partial_r\phi)^2\right)^4}$$
$$- \frac{12(\partial_r\phi)(\partial_s\phi)^3(\partial_t\phi)^2}{\left(\sum_r (\partial_r\phi)^2\right)^4} + \frac{48(\partial_r\phi)^3(\partial_s\phi)^3(\partial_t\phi)^2}{\left(\sum_r (\partial_r\phi)^2\right)^5} \qquad (2.65)$$

The phase-field equation including interfacial anisotropy can be solved by calculating Eq. (2.55) by using partial derivatives of $Q(\boldsymbol{n})$ and $S(\boldsymbol{n})$ (Eqs. (2.60)-(2.65)).

2.6 QPFM model for directional solidification

All of the phase-field models described so far are applicable to the isothermal solidification process. Next, I will explain a model that can be applied when there is a temperature gradient, such as directional solidification process. For the sake of simplicity of calculation, I will explain the case that constant temperature gradient is applied throughout the entire system, so-called frozen temperature approximation, in which the temperature field is given as

$$T(z) = T_0 + G(z - V_p t) \tag{2.66}$$

where G is temperature gradient along z axis and V_p is pulling speed.
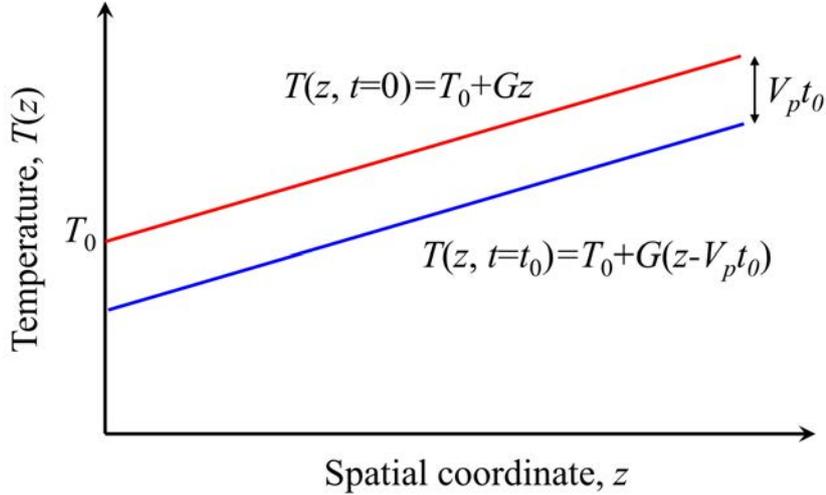
Fig. 2.2. Schematics of frozen temperature approximation.

Initial temperature field (red line of Fig. 2.2) is set as $T(z) = T_0 + Gz$, where T_0 is the temperature at the bottom of system. Then, the temperature is decreased by $V_p t_0$ when the time passes by t_0 (blue line of Fig. 2.2).

By considering the temperature gradient explained above, the driving force term in the phase-field equation (2.55), $\lambda^* g(\phi) u$, changes as follows:

$$\lambda^* g(\phi) \left[u + \frac{z - V_p t}{l_T} \right] \tag{2.67}$$

where l_T is thermal length given by $l_T = |m_l|(1 - k)c_0/kG$ and c_0 is the alloy concentration. Also this temperature gradient does not essentially change the final

form of diffusion equation including anti-trapping current (2.50). Thus, the final form of phase-field equation for directional solidification can be expressed as follows.

$$\tau(\boldsymbol{n})\frac{\partial \phi}{\partial t} = \nabla \cdot \left[W^2(\boldsymbol{n})\nabla\phi \right]$$
$$+ \sum_{s=x,y,z} \frac{\partial}{\partial s} \left[|\nabla\phi|^2 W(\boldsymbol{n})\frac{\partial W(\boldsymbol{n})}{\partial(\partial_s\phi)} \right] \tag{2.68}$$
$$- f'(\phi) - \lambda^* g'(\phi) \left[u + \frac{z - V_p t}{l_T} \right]$$

2.7 Normalization of phase-field model

Simulation results can be standardized by normalization of time and spatial scale. In this study, normalization of time and spatial scale was performed by using capillary length d_0 and solute diffusivity in liquid phase D_l as follows:

$$\widetilde{x} = \frac{x}{d_l} \qquad \widetilde{t} = t\frac{D_l}{d_0^2} \tag{2.69}$$

where $\widetilde{x}$ and $\widetilde{t}$ are normalized spatial coordinate and time. From this normalization, derivatives of ϕ with $\widetilde{x}$ and $\widetilde{t}$ can be represented as follows:

$$\frac{\partial \phi}{\partial \widetilde{x}} = d_0\frac{\partial \phi}{\partial x} \qquad \frac{\partial \phi}{\partial \widetilde{t}} = \frac{d_0^2}{D_l}\frac{\partial \phi}{\partial t} \tag{2.70}$$

By using these relationships, the normalized phase-field equation and diffusion equation with anti-trapping current can be expressed as follows:

$$\alpha\eta^2 \left[1 + (1-k)u \right] a_s^2(\boldsymbol{n})\frac{\partial \phi}{\partial \widetilde{t}} = \eta^2\widetilde{\nabla} \cdot \left(a_s^2(\boldsymbol{n})\widetilde{\nabla}\phi \right)$$
$$+ \eta^2 \sum_{r=x,y,z} \frac{\partial}{\partial r} \left(|\widetilde{\nabla}\phi|^2 a_s(\boldsymbol{n})\frac{\partial a_s(\boldsymbol{n})}{\partial(\partial_r\phi)} \right) \tag{2.71}$$
$$+ \phi(1-\phi^2) - a_1\eta(1-\phi^2)^2 u$$

36

$$\frac{[1 + k - (1 - k)h(\phi)]}{2} \frac{\partial u}{\partial \widetilde{t}} = \widetilde{\nabla} \cdot \left(q(\phi) \widetilde{\nabla} u \right.$$

$$\left. + a(\phi)\eta[1 + (1 - k)u] \frac{\partial \phi}{\partial \widetilde{t}} \frac{\widetilde{\nabla}\phi}{|\widetilde{\nabla}\phi|} \right)$$

$$+ \frac{1}{2}[1 + (1 - k)u] \frac{\partial h(\phi)}{\partial \widetilde{t}} \tag{2.72}$$

where a_1 is constant given by $a_1 = 0.8839$, $\eta = W_0/d_0$ and $\alpha = D_l\tau_0/W_0^2$. Also, the phase-field equation for directional solidification can be expressed as follows:

$$\alpha\eta^2 \left[1 + (1 - k)u\right] a_s^2(\boldsymbol{n}) \frac{\partial \phi}{\partial \widetilde{t}} = \eta^2 \widetilde{\nabla} \cdot \left(a_s^2(\boldsymbol{n}) \widetilde{\nabla}\phi \right)$$

$$+ \eta^2 \sum_{r=x,y,z} \frac{\partial}{\partial r} \left(|\widetilde{\nabla}\phi|^2 a_s(\boldsymbol{n}) \frac{\partial a_s(\boldsymbol{n})}{\partial(\partial_r\phi)} \right) \tag{2.73}$$

$$+ \phi(1 - \phi^2) - a_1\eta(1 - \phi^2)^2 \left[u + \frac{\widetilde{z} - \widetilde{V_p}\widetilde{t}}{\widetilde{l_T}} \right]$$

where $\widetilde{z} = z/d_0$, normalized thermal length and pulling speed are given by $\widetilde{l_T} = l_T/d_0$ and $\widetilde{V_p} = V_p d_0/D_l$, respectively.

From Eqs. (2.71)-(2.73), it can be seen that the parameters that control the phase-field equation and the diffusion equation became only k, u, ε_1, ε_2, V_p and l_T by the normalization.

2.8 Nonlinear preconditioning of phase-field model

As described this this chapter, the phase-field model is a powerful tool to solve the free-boundary problem numerically. However, there is a limitation of computational grid size due to the nonlinear nature of phase-field variabe within the interface, which acts as a major problem in increasing the scale of simulation. Glasner [25] proposed a method to enable simulation at a larger grid size using a nonlinear preconditioning method. In order to apply the preconditioning method, the governing equations of phase-field and concentration field must be reformulated using the following relationship:

$$\phi = \tanh\left(\frac{\psi}{\sqrt{2}}\right) \tag{2.74}$$

The first and second partial derivatives of ϕ using ψ can be expressed as follows:

$$\phi_x = \frac{1 - \phi_x}{\sqrt{2}} \psi_x \tag{2.75}$$

$$\phi_{xx} = \frac{1 - \phi^2}{\sqrt{2}} [\psi_{xx} - \sqrt{2}\phi\psi_x^2] \tag{2.76}$$

Then Eq (2.71)-(2.73) can be reformulated by the above relationship as follows. Phase-field equation for isothermal solidification (Eq. (2.71))

$$\begin{aligned}
\alpha\eta^2 \left[1 + (1 - k)u\right] a_s^2(\boldsymbol{n}) \frac{\partial\psi}{\partial t} = \; &\eta^2 \nabla \cdot \left(a_s^2(\boldsymbol{n})\nabla\phi\right) \\
&+ \eta^2 a_s(\boldsymbol{n}) \left[\nabla\psi^2 - \sqrt{2}|\nabla\psi|^2\right] \\
&+ \eta^2 \sum_{r=x,y,z} \frac{\partial}{\partial r} \left(\nabla\psi|^2 a_s(\boldsymbol{n}) \frac{\partial a_s(\boldsymbol{n})}{\partial\psi_r}\right) \\
&- \sqrt{2}\eta^2 \phi a_s(\boldsymbol{n}) \sum_{r=x,y,z} \psi_r \frac{\partial a_s(\boldsymbol{n})}{\partial\psi_r} \\
&+ \sqrt{2}\phi - \sqrt{2}a_1\eta(1 - \phi^2)u
\end{aligned} \tag{2.77}$$

Note that the $\tilde{}$ notation is omitted in this equation.

Diffusion equation with anti-trapping current (Eq. (2.72)) can be reformulated as follows:

$$\begin{aligned}
\frac{[1 + k - (1 - k)h(\phi)]}{2} \frac{\partial u}{\partial t} = \nabla \cdot \bigg(&q(\phi)\nabla u \\
&+ \frac{\eta}{4}(1 - kq_s)[1 + (1 - k)u](1 - \phi^2)\frac{\partial\psi}{\partial t}\frac{\nabla\psi}{|\nabla\psi|}\bigg) \\
&+ \frac{1}{2\sqrt{2}}[1 + (1 - k)u](1 - \phi^2)\frac{\partial h(\psi)}{\partial t}
\end{aligned} \tag{2.78}$$

Finally, phase-field quation for directional solidification (Eq. (2.73)) can be reformulated as follows:

$$
\begin{aligned}
\alpha\eta^2\left[1+(1-k)u\right]a_s^2(\boldsymbol{n})\frac{\partial\psi}{\partial t} ={}& \eta^2\nabla\cdot\left(a_s^2(\boldsymbol{n})\nabla\phi\right) \\
&+ \eta^2 a_s(\boldsymbol{n})\left[\nabla\psi^2-\sqrt{2}|\nabla\psi|^2\right] \\
&+ \eta^2\sum_{r=x,y,z}\frac{\partial}{\partial r}\left(|\nabla\psi|^2 a_s(\boldsymbol{n})\frac{\partial a_s(\boldsymbol{n})}{\partial\psi_r}\right) \\
&- \sqrt{2}\eta^2\phi a_s(\boldsymbol{n})\sum_{r=x,y,z}\psi_r\frac{\partial a_s(\boldsymbol{n})}{\partial\psi_r} \\
&+ \sqrt{2}\phi-\sqrt{2}a_1\eta(1-\phi^2)\left[u+\frac{\widetilde{z}-\widetilde{V}_p\widetilde{t}}{\widetilde{l}_T}\right]
\end{aligned}
\tag{2.79}
$$

2.9 Summary

In this chapter, the details of phase-field model which used in the simulation of this study were explained in detail. Solid-liquid interface is represented by introduction phase-field variable, and time-evolution equations of conserved and non-conserved quantity are derived based on the second law of thermodynamics. Then, the phase-field models that can reproduce isothermal solidification process of pure substance and binary alloy were described. Furthermore, a quantitative phase-field model, used in this research, was explained. Described model includes the anisotropic solid-liquid interfacial energy that can correctly represent cubic crystal symmetry in three-dimension was explained. A quantitative phase-field model for directional solidification of binary alloy was also described. In addition, normalization method of those phase-field models of binary alloy which is described above was also described. Finally, the phase-field model using nonlinear preconditioning was described.

References

[1] W. Kurz, D. J. Fisher, Fundamentals of solidification, Vol. 1, Trans Tech Publications Aedermannsdorf, Switzerland, 1986.

[2] W. J. Boettinger, S. R. Coriell, A. Greer, A. Karma, W. Kurz, M. Rappaz, R. Trivedi, Solidification microstructures: recent developments, future directions, Acta materialia 48 (1) (2000) 43–70.

[3] J. A. Dantzig, M. Rappaz, Solidification, EPFL press, 2009.

[4] J. S. Langer, Instabilities and pattern formation in crystal growth, Reviews of Modern Physics 52 (1) (1980) 1.

[5] B. Chalmers, Principles of solidification.

[6] M. C. Flemings, Solidification processing, Materials Science and Technology.

[7] W. D. Callister, D. G. Rethwisch, Fundamentals of materials science and engineering, Vol. 471660817, Wiley London, UK:, 2000.

[8] R. Kobayashi, Modeling and numerical simulations of dendritic crystal growth, Physica D: Nonlinear Phenomena 63 (3-4) (1993) 410–423.

[9] M. Ohno, K. Matsuura, Quantitative phase-field modeling for two-phase solidification process involving diffusion in the solid, Acta Materialia 58 (17) (2010) 5749–5758.

[10] T. Takaki, Phase-field modeling and simulations of dendrite growth, ISIJ international 54 (2) (2014) 437–444.

[11] T. Takaki, M. Ohno, T. Shimokawabe, T. Aoki, Two-dimensional phase-field simulations of dendrite competitive growth during the directional solidification of a binary alloy bicrystal, Acta Materialia 81 (2014) 272–283.

[12] J. B. Marion, Classical dynamics of particles and systems, Academic Press, 2013.

[13] H. Goldstein, Classical mechanics, Pearson Education India, 2011.

[14] J. T. Oden, J. N. Reddy, Variational methods in theoretical mechanics, Springer Science & Business Media, 2012.

[15] V. Benci, D. Fortunato, Variational methods in nonlinear field equations, Springer Monographs in Mathematics, Springer 2 (2014) 3.

[16] A. Karma, W.-J. Rappel, Phase-field method for computationally efficient modeling of solidification with arbitrary interface kinetics, Physical review E 53 (4) (1996) R3017.

[17] E. Brener, Needle-crystal solution in three-dimensional dendritic growth, Physical review letters 71 (22) (1993) 3653.

[18] Y. Saito, Statistical physics of crystal growth, World Scientific, 1996.

[19] S. G. Kim, W. T. Kim, T. Suzuki, Phase-field model for binary alloys, Physical review e 60 (6) (1999) 7186.

[20] A. Karma, W.-J. Rappel, Quantitative phase-field modeling of dendritic growth in two and three dimensions, Physical review E 57 (4) (1998) 4323.

[21] A. Karma, Phase-field formulation for quantitative modeling of alloy solidification, Physical Review Letters 87 (11) (2001) 115701.

[22] M. Ohno, K. Matsuura, Quantitative phase-field modeling for dilute alloy solidification involving diffusion in the solid, Physical Review E 79 (3) (2009) 031603.

[23] S.-K. Chan, H.-H. Reimer, M. Kahlweit, On the stationary growth shapes of NH_4Cl dendrites, Journal of Crystal Growth 32 (3) (1976) 303–315.

[24] W. Fehlner, S. Vosko, A product representation for cubic harmonics and special directions for the determination of the fermi surface and related properties, Canadian Journal of Physics 54 (21) (1976) 2159–2169.

[25] K. Glasner, Nonlinear preconditioning for diffuse interfaces, Journal of Computational Physics 174 (2) (2001) 695–711.

Chapter 3

Morphological diversity of isothermally-solidified microstructure

In this chapter, the morphological change of isothermally-solidified microstructure associated transition phenomenon of preferred growth direction will be explained. Also, effects of solidification condition and alloy system on morphological will be discussed. Details of computationals conditions and acceleration method will be described.

3.1 Computational conditions of isothermal solidification

Phase-field simulation for isothermal solidification ans diffusion equation with anti-trapping current were discretized using a second-order finite difference scheme with grid spacing Δx and solved using a first order Euler scheme. Phase-field equation for isothermal solidification (Eq. (2.71)) and diffusion equation with anti-trapping current (Eq. (2.72)) were discretized using a second-order finite difference scheme with grid spacing Δx and solved using a first order Euler scheme. Three-dimensional simulations for one-eighth of a freely growing dendrite were performed. The computational system is the cubic shape and it was divided into uniform cubic grids with Δx. The initial system is occupied by the liquid phase with the initial
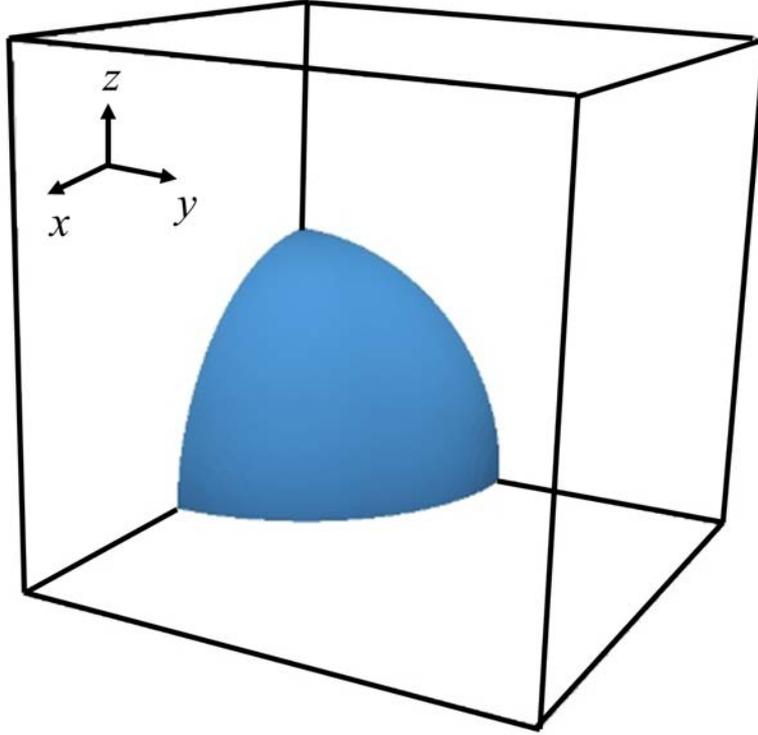
Fig. 3.1. Schematic representation of computational domain for isothermal solidification.

solid seed put in the origin (see Fig. 3.1). The mirror boundary condition was applied on x-y plane at $z = 0$, y-z plane at $x = 0$ and z-x plane at $y = 0$, while the zero-flux boundary condition was applied on x-y plane at $z = L_s$, y-z plane at $x = L_s$ and z-x plane at $y = L_s$ where L_s is the system size. The number of grid points was set to 768^3 or 1024^3 and Δx was set to 0.075 and 0.080 μm, depending on the conditions.

In this study, simulations were carried out the for isothermal solidification in fcc-based binary alloys. The following parameters were employed ; melting point of pure substance, $T_m = 1000$ [K], liquidus slope, $m_L = -600$ [K/at.%], molar volume, $v_m = 10^{-6}$ [m^3/mol], average interfacial energy $\gamma_0 = 0.15$ [J/m^2] and solute diffusivity in liquid $D_L = 3.0 \times 10^{-9}$ [m^2/s]. The solid diffusivity D_s was set to 0 for the sake of simplicity. In this case, when the spatial and time scales are normalized by d_0 and d_0^2/D_L, the problem depends only on four parameters, i.e., the initial supersaturation u_0, the partition coefficient k and the anisotropy parameters ε_1 and ε_2. I changed these parameters systematically and the values used in the simulation are summarized in 3.1. I carried out a numerical survey for the growth morphology

in the binary alloy systems to construct the orientation selection maps with high accuracy. Note that the capillary length d_0 is given as $d_0 = \Gamma / (|m_L|(1 - k)c_L^e)$ with the Gibbs-Thomson coefficient Γ. Hence, d_0 changes according to k in this study. Specifically, d_0 decreases as k decreases in this analysis.

Table 3.1: Physical parameters used in isothermal solidification.

Physical parameter	Value
Anisotropy paramters, ε_1	0 - 0.2
Anisotropy paramters, ε_2	-0.015 - 0
Initial supersaturation, u_0	$-0.45, -0.40, -0.35$
Partition coefficient, k	0.10, 0.15, 0.20

The simulations of isothermal solidification were accelerated by using multiple GPUs, NVidia Tesla P100. Six and eight GPUs were used in computations for 768^3 and 1024^3 grid points, respectively. In both cases, the computational domain was one-dimensionally divided for the sake of MPI efficiency which will be explained in next section.

3.2 Acceleration method of simulations

In this study, GPGPU (General-Purpose Computing on Graphics Processing Units) was used to accelerate simulation. GPGPU is a technology using a graphics processing unit (GPU), which typically handles computation only for computer graphics, to perform the computation in applications traditionally handled by the central processing unit (CPU) [1, 2].

Simulations were perforemd by using a finite difference lattice as shown in Fig. 3.2. It becomes possible to simulate the formation process of microstructure by calculating $\phi_{t+\Delta t}(x_i, y_i)$ and $u_{t+\Delta t}(x_i, y_i)$, values at the next time step (after Δt) of $\phi(x_i, y_i)$ and $u(x_i, y_i)$ at each coordinate. In the conventional CPU simulation, the phase-field parameter ϕ and concentration field u are calculated at one grid point, then the next point is calculated. For example, the calculation is proceeded from (x_1, y_1) to (x_2, y_1) and to (x_3, y_1). However, in the calculation using GPU, computation is performed on a plurality of coordinates by one operation using a large number of computation cores in GPU. For example, by calculating the variables in
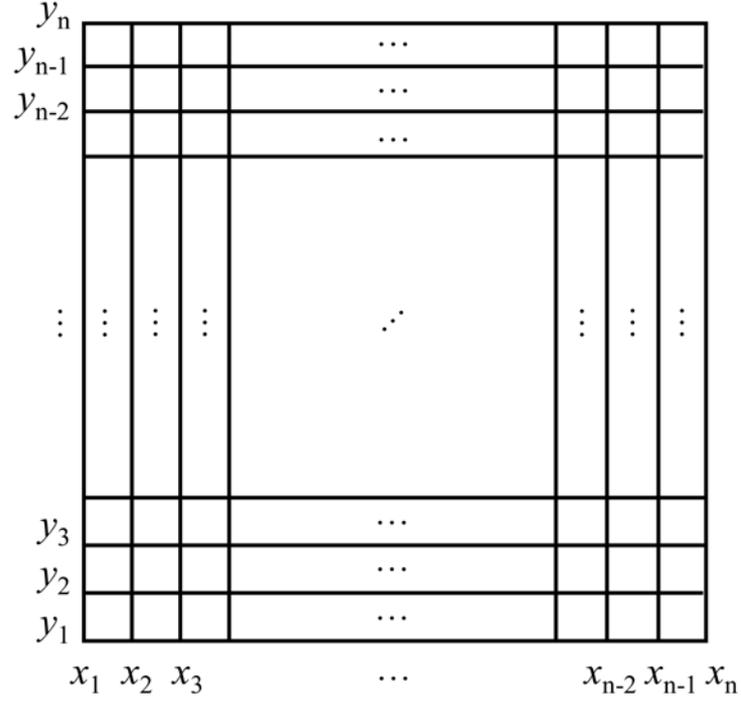
Fig. 3.2. Schematic representation of computational domain represented as finite difference lattice.

$(x_1 - x_{16}, y_1 - y_{16})$ by one operation, the calculation can be performed faster than the calculation on CPU. Currently, phase-field simulation can be accelerated from dozens to hundred times by using GPU. The flow chart of the GPGPU calculation is shown in Fig. 3.3 and details are as follows.

(1) First, set input parameters such as k, u_0, ε_1 and ε_2.

(2) Then set the initial conditions of ϕ and u using input parameters (these two steps are executed in CPU).

(3) Copy ϕ and u from CPU to GPU.

(4) Compute ϕ_{n+1} and u_{n+1} from ϕ and u by parallel computation on GPU.

(5) Conduct iterative computation after updating this value.

(6) After some timesteps, print out data (ϕ and u) and visualize.
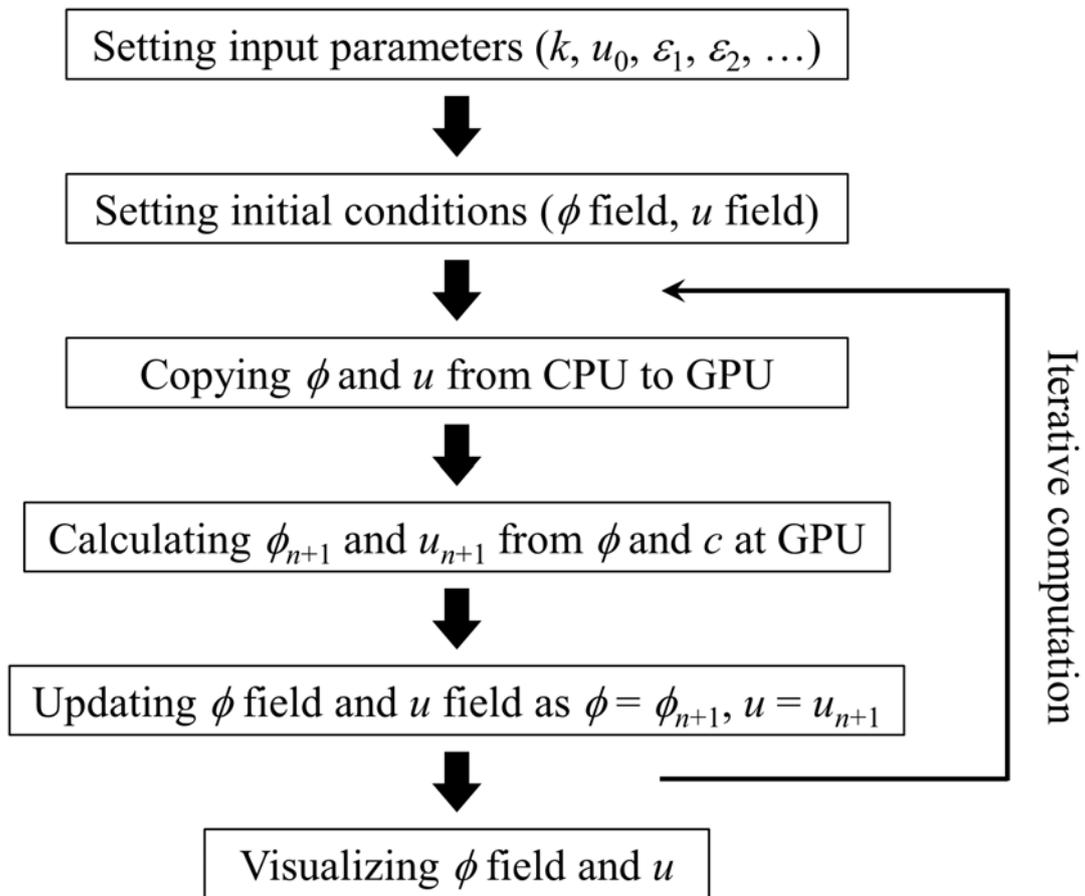
Fig. 3.3. Program flow chart of phase-field simulation by GPGPU.

Although acceleration of the simulation can be achieved with GPU-based calculation, there is one more problems in this method. That is the limitation of the calculation size due to the lack of the GPU memory. Typical GPU has only 2-6GBs memory and the latest GPUs (NVidia Tesla P100 and V100) have just 16GBs. This is much lower than the physical memory of the usual computer for calculation. One way to overcome this memory shortage is to use multiple-GPUs by Message Passing Interface (MPI). MPI is a standard for describing information exchange in distributed and parallel processing [3]. It is possible to calculate using different GPU by applying MPI which is usually used to share memory in different CPU-based computer nodes [1,2]. Next, a schematic method of multi-GPUs calculation using MPI is briefly described in case of two GPUs for simplicity.
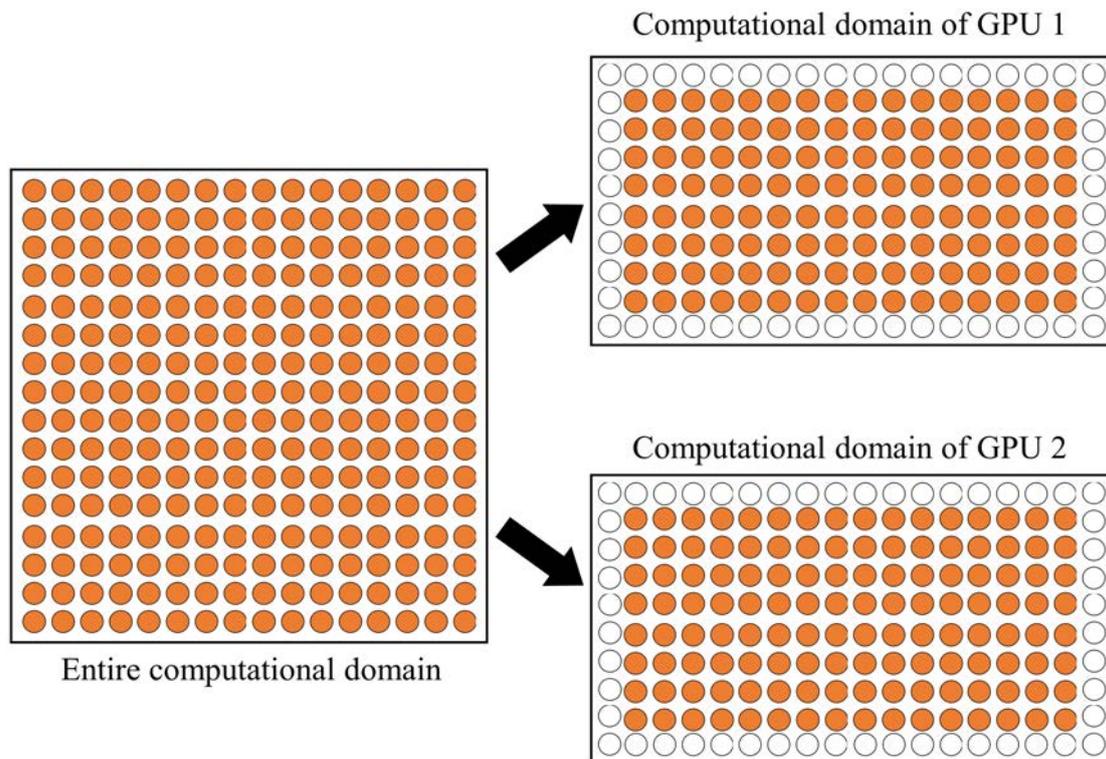
Fig. 3.4. Schematics of computational domain divided for two GPUs.

As shown in Fig. 3.4 the computational domain is divided into two GPUs. The blue circle represents the lattice needed for the calculation and the white circle represents the halo region for storing the boundary values in different GPUs. Then the following process is performed to transmit the boundary value between two GPUs (see Fig. 3.5).
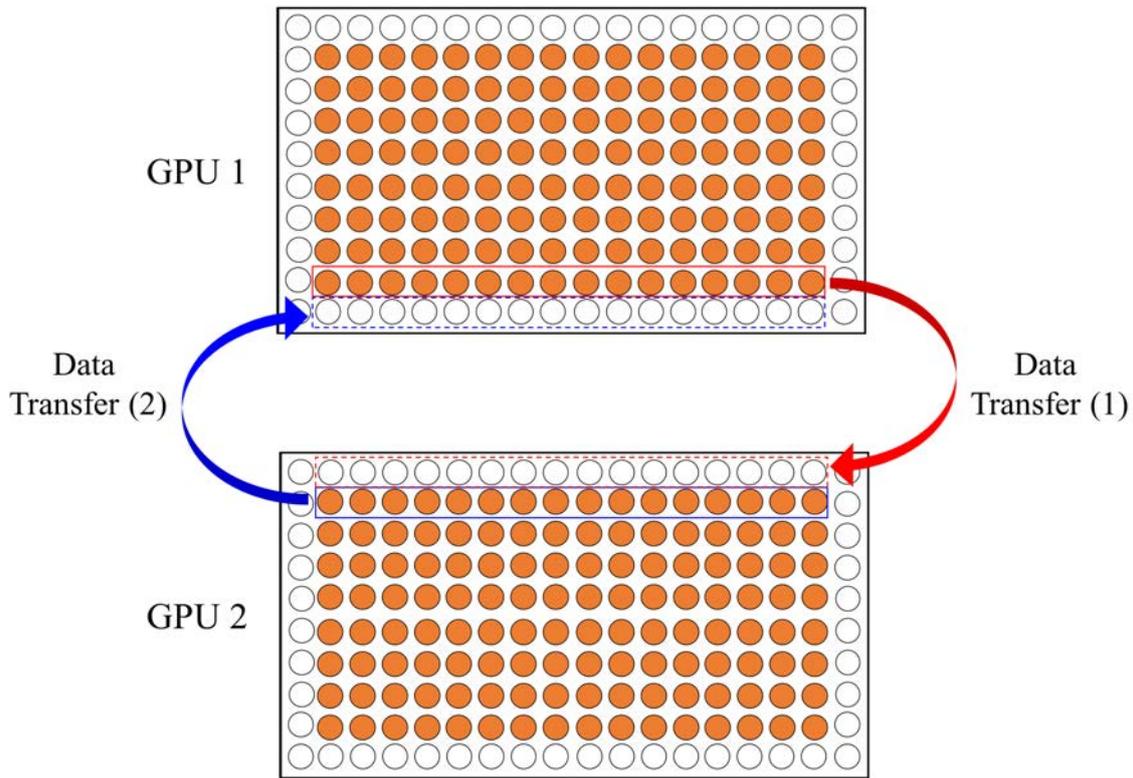
Fig. 3.5. Schematics of transferring process between two GPUs.

(1) Sending the data of GPU1(red solid line box) to the halo region of GPU2(red dotted line box) and GPU2 receiving the data.

(2) Sending the data of GPU2(blue solid line box) to the halo region of GPU1(blue dotted line box) and GPU1 receiving the data.

By transferring the boundary values in this way, it becomes possible to simulate with multiple-GPUs.

Using this multiple-GPUs technique, it became possible to simulate the millimeter-scale solidification microstructure with only using laboratory-level simulation server, which is conventionally only possible on supercomputers equipped with hundreds of GPUs (see Fig. 3.6) .
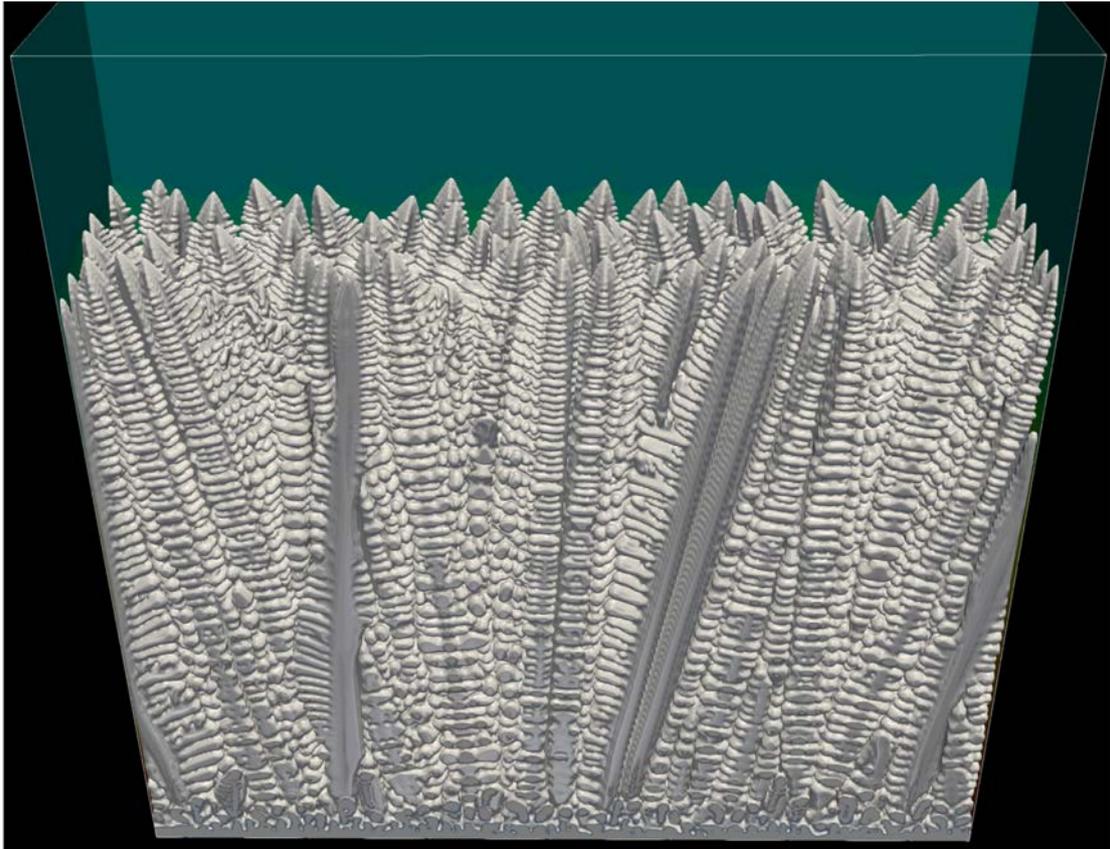
Fig. 3.6. Large-scale simulation results of coulmnar dendritic growth during directional solidification in an Al-3mass% Cu alloy with a temperature gradient 10 K/mm and pulling speed 90 μm/s. The system was $0.7 \times 2.8 \times 2.8$mm^3 size and divided by 10 GPUs.

3.3 Classification of growth morphologies

Different growth morphologies of isothermally-solidified microstructure were found by changing initial supersaturature u_0, partition coefficient k, anisotropy parameters ε_1 and ε_2. Figures 3.7 and 3.8 show the simulated microstructures for $u_0 = -0.4$ and $k = 0.1$. Figure 3.7(a) represents the dendritic structure simulated for $\varepsilon_1 = 0.2$ and $\varepsilon_2 = -0.01$. In this case, $\langle 100 \rangle$ dendritic growth occurs. This is the typical growth pattern of dendrite usually observed in fcc-based alloys when the contribution of ε_1 to the growth morphology is dominant. Figure 3.7(b) represents the microstructure simulated for $\varepsilon_1 = 0$ and $\varepsilon_2 = -0.01$. In this case, $\langle 110 \rangle$ dendrite growth occurred, since the contribution of ε_2 is dominant. This growth morphology was observed in the directionally-solidified microstructure of Al-Zn alloy with high Zn concentration range [4].
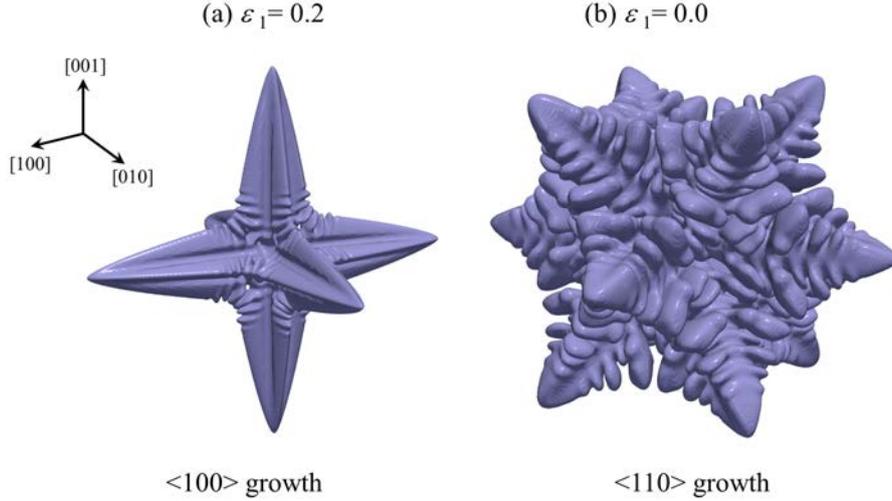
Fig. 3.7. $\langle 100 \rangle$ and $\langle 110 \rangle$ growth morphologies obtained by phase-field simulations for $u_0 = -0.4$, $k = 0.1$ and different ε_1 with fixed $\varepsilon_2 = -0.01$.

In early works [4, 5] hyperbranched growth was observed with $\langle 100 \rangle$ and $\langle 110 \rangle$ growth morphologies. In this study, it was found that the hyperbranched growth should be further classified into two types as shown in Figs 3.8 (a) and (b). In the case of Fig. 3.8(a), the anisotropy parameters were set to $\varepsilon_1 = 0.1$ and $\varepsilon_2 = -0.01$. Although the growth morphology looks similar to $\langle 100 \rangle$ growth morphology (Fig. 3.7(a)), the branch growing in $\langle 100 \rangle$ direction in Fig. 3.7(a) splits into four branches in Fig. 3.8(a). This growth was defined morphology as $\langle 100 \rangle$-like hyperbranched growth morphology. Another hyperbranched growth morphology is represented in

Fig. 3.8(b) simulated for $\varepsilon_1 = 0.05$ and $\varepsilon_2 = -0.01$. Although this growth morphology looks like $\langle 110 \rangle$ growth morphology (Fig. 3.7(b)), there are many branches and it cannot be clearly identified which is the primary branches in Fig. 3.8(b). Thus, this growth morphology was defined as $\langle 100 \rangle$-like hyperbranched growth morphology. In summary, growth morphologies were classified into four-types in isothermally-solidified microstructure.


(a) $\varepsilon_1 = 0.1$ (b) $\varepsilon_1 = 0.05$

[001]
[100]   [010]

<100>–like
hyperbranched

<110>–like
hyperbranched
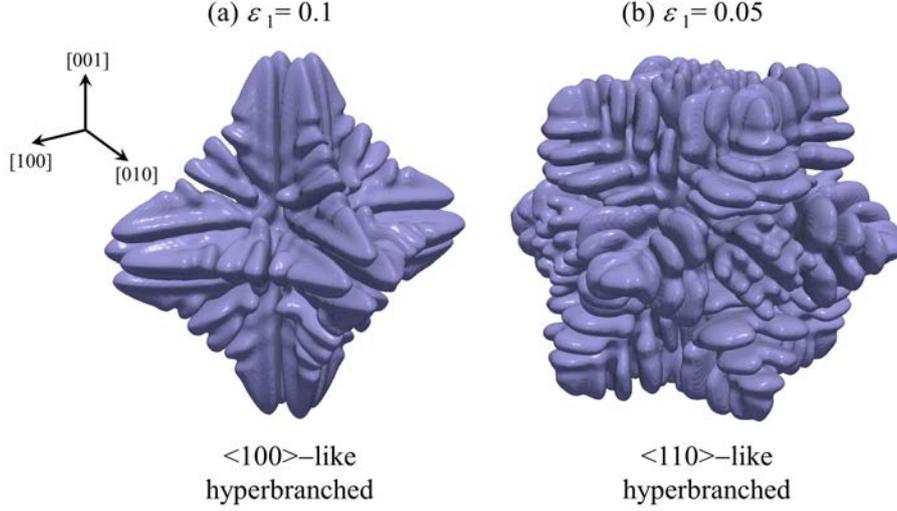
Fig. 3.8. Two types of hyperbranched growth morphologies obtained by phase-field simulations for $u_0 = -0.4$, $k = 0.1$ and different ε_1 with fixed $\varepsilon_2 = -0.01$.

To clarify the regions of four different growth morphologies in ε_1-ε_2 space, an extensive investigation was performed by changing ε_1 and $\varepsilon_2 1$. More specifically, the boundary between the different growth morphologies in ε_1-ε_2 space was investigated by changing ε_1 with fixed value of ε_2, based on a searching algorithm called the binary search and details of this algorithm is explained in Ref. [6].

The detailed classification of the growth morphology was carried out by using the microstructure on (001) section as shown in Figs. 3.9-3.10. Figures 3.9 (a) and (b) are the microstructures on (001) section calculated for $\varepsilon_1 = 0.10625$ and $\varepsilon_1 = 0.10$, respectively. ε_2 is -0.01 in both cases. In Fig. 3.9(a), the branch grows in $\langle 100 \rangle$ orientation at the edge of the system as indicated by the dashed circle and I called this branch as $\langle 100 \rangle$ primary branch. However, there is no $\langle 100 \rangle$ primary branch in Fig. 3.9(b). The former is classified into $\langle 100 \rangle$ growth morphology, while the latter one is classified into $\langle 100 \rangle$-like hyperbranched growth morphology. To be more precise, the morphology was classified into the hyperbranched growth morphology

when $\langle 100 \rangle$ primary branch does not exist or it is shorter than adjacent branches.
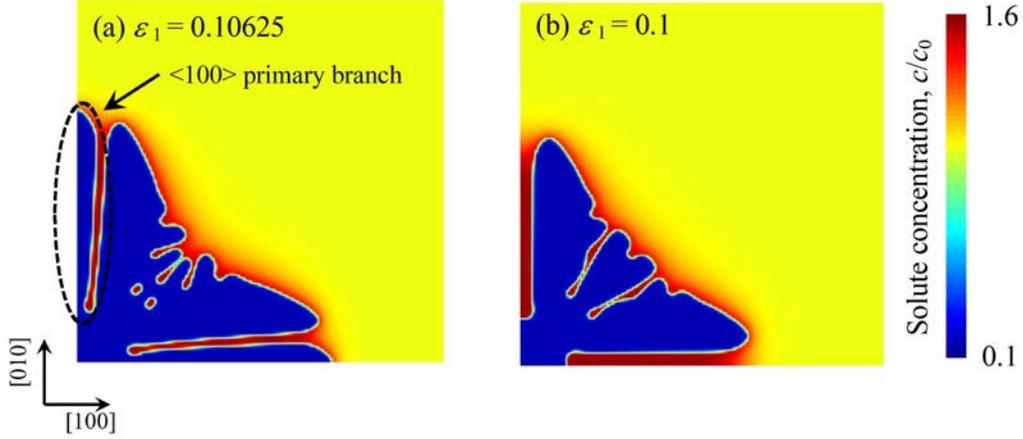
Fig. 3.9. Microstructures on (001) section calculated by different ε_1 with fixed $\varepsilon_2 = -0.01$. $\langle 100 \rangle$ growth and $\langle 100 \rangle$-like hyperbranched growth morphology can be identified.
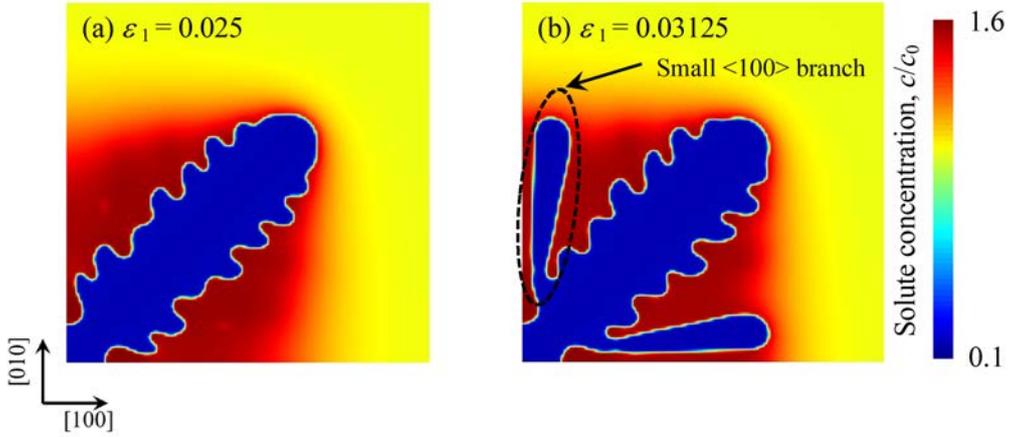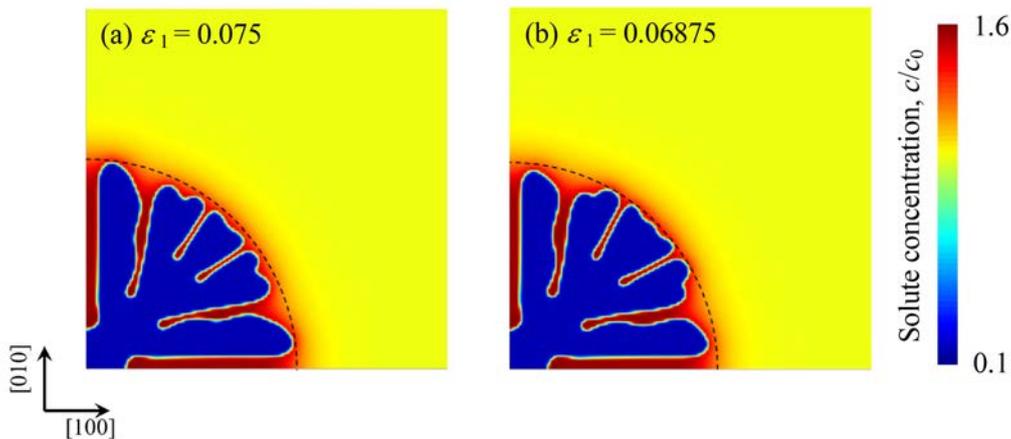

Fig. 3.10. Microstructures on (001) section calculated by different ε_1 with fixed $\varepsilon_2 = -0.01$. $\langle 110 \rangle$ growth and $\langle 110 \rangle$-like hyperbranched growth morphology can be identified.

Figure 3.10(a) is the microstructure calculated for $\varepsilon_1 = 0.025$ and $\varepsilon_2 = -0.01$. The $\langle 110 \rangle$ branch can be seen clearly and this growth morphology represents $\langle 110 \rangle$ growth. In Fig. 3.10(b) calculated for $\varepsilon_1 = 0.03125$ and $\varepsilon_2 = -0.01$, there is also $\langle 110 \rangle$ branch. However, in this case, another small branch growing in $\langle 100 \rangle$ appeared as indicated by the dotted circle. Thus, this growth morphology was defined as the $\langle 110 \rangle$-like hyperbranched growth morphology. Note that this criterion for classification between $\langle 110 \rangle$ growth and hyperbranched growth morphologies is different from the one reported in the early works [4,5]. In early works, they classified

$\langle 110 \rangle$ growth morphology and hyperbranched growth morphology by the occurrence of the tip splitting of $\langle 110 \rangle$ branch. In this study, it was found that the occurrence of the tip splitting of branch is very sensitive to the numerical accuracy such as grid spacing and the way of calculation of Laplacian in the finite difference method. Although the tip splitting is an important indicator of the morphological change of solidified structure, the $\langle 110 \rangle$ tip splitting was not considered in classification of growth morphology in this study. Instead of the occurrence of $\langle 110 \rangle$ tip splitting, the growth morphology was classified by the emergence of small $\langle 100 \rangle$ branches as shown in Fig. 3.10(b) which is also an important indicator of the morphological change of dendrite.

Figure 3.11 shows two types of the hyperbranched growth morphology. Figure 3.11(a) shows the microstructure on (001) section simulated for $\varepsilon_1 = 0.075$ and $\varepsilon_2 = -0.01$, while Fig. 3.11(b) shows the case of $\varepsilon_1 = 0.06875$ and $\varepsilon_2 = -0.01$. In Fig. 3.11(a), the growth of branches close to $\langle 100 \rangle$ direction is slightly faster than the other branches. On the other hand, in Fig. 3.11(b), $\langle 110 \rangle$ branch or branches split from former $\langle 110 \rangle$ branch grow slightly faster than the other branches. Therefore, the morphologies was classified in Figs. 3.11(a) and (b) into $\langle 100 \rangle$-like hyperbranched growth and $\langle 110 \rangle$-like hyperbranched growth morphologies, respectively. Note that emergence of these growth patterns was very sensitive to the system size of simulation. Hence, in cases which these growth modes arise, simulations were performed with larger computational domain size with 1024^3 grids points.

Fig. 3.11. Microstructures on (001) section calculated by different ε_1 with fixed $\varepsilon_2 = -0.01$. $\langle 100 \rangle$-like hyperbranched growth and $\langle 110 \rangle$-like hyperbranched growth morphology can be identified.

3.4 Morphology map of isothermally-solidified microstructure

As described in section 3.3, four different growth morphologies were classified by phase-field simulations of fcc-based alloy. From this classification, morphology map was constructed of isothermally-solidified microstructure. This map shows what kind of growth morphology will be formed with different anistoropy parameters in ε_1-ε_2 space. The morphology map in case of $u_0 = -0.4$ and $k = 0.1$ is shown in Fig. 3.12.
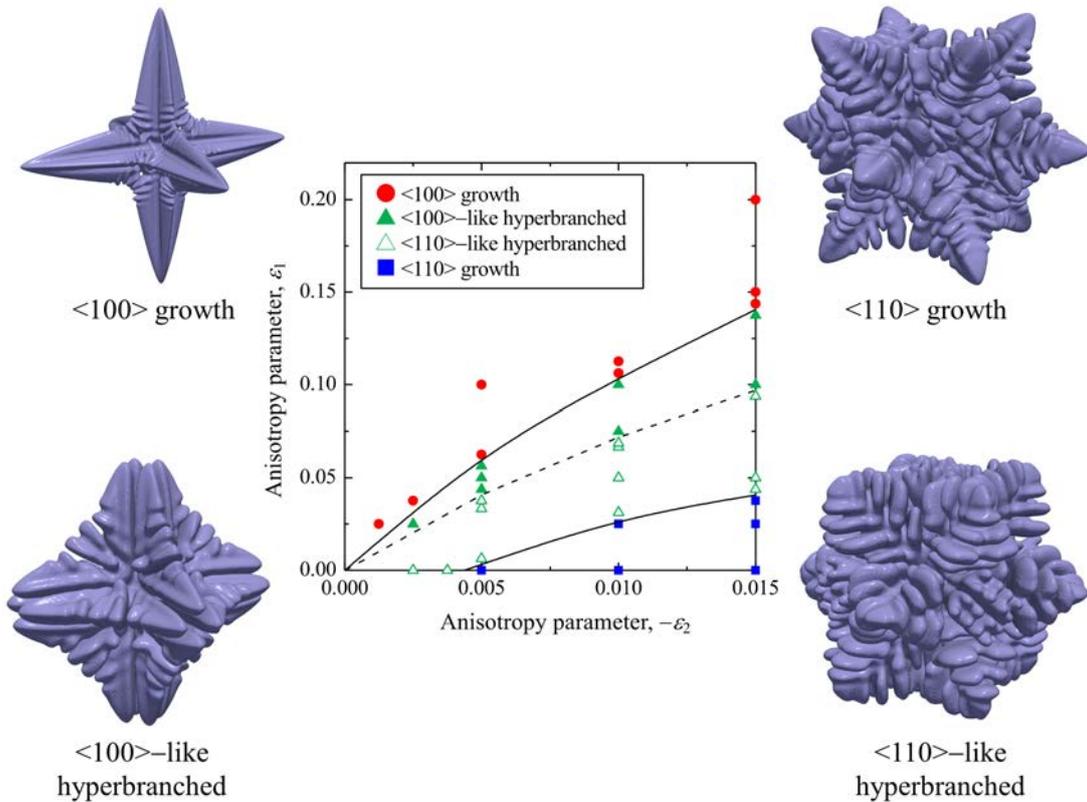
Fig. 3.12. Morphology map in case of $u_0 = -0.4$, $k = 0.1$. This map shows what kind of growth morphology will be formed with different sets of anisotropy parameters.

The $\langle 100 \rangle$ growth region can be seen in the upper-left part and $\langle 110 \rangle$ growth region can be seen in the lower-right parts. Also the hyperbranched growth region exist between them. This is similar to orientation selection maps obtained for pure material [4] and Al-Zn alloy [5]. However, there are two important differences. First, as explained in section 3.3, growth morphologies were classified into four

types. The dotted line indicates the boundary between $\langle 100 \rangle$-like hyperbranched growth and $\langle 110 \rangle$-like hyperbranched growth regions. This dashed line is close to the theoretical boundary [4] of $\langle 100 \rangle$ and $\langle 110 \rangle$ growth, $\varepsilon_2 = -20\varepsilon_2/3$, obtained from the minimum interface stiffness (see Fig.1.3). This dashed line is missing in early works [4, 5]. Another difference appears in the boundary between $\langle 110 \rangle$ growth and hyperbranched growth. This boundary was started from $(\varepsilon_1, \varepsilon_2) = (0, 0)$ in early works. In this study, it was found that $\langle 110 \rangle$-like hyperbranched growth occurs when anisotropy parameters were set to $(\varepsilon_1, \varepsilon_2) = (0, 0.0025)$ and $(\varepsilon_1, \varepsilon_2) = (0, 0.003125)$. Thus, the boundary between $\langle 110 \rangle$ growth and hyperbranched growth is started from $(\varepsilon_1, \varepsilon_2) = (0, 0.00375)$ in this study.

As shown in Fig. 3.12, the morphology map of isotheramlly-solidifed microstructure for an binary alloy system was constructed from the systematic investigation of growth morphology by changing ε_1-ε_2 space.

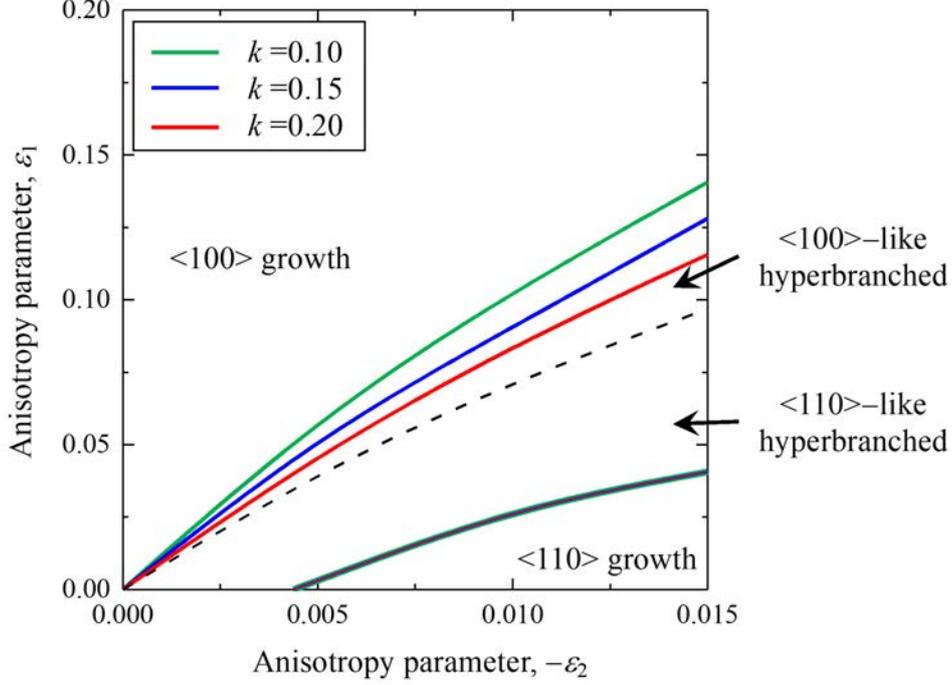## 3.5 Effects of solidification condition and alloy system on morphology map

In this study, to investigate the effect of solidification condition on morphology map, simulations were carried out for three different values of initial supersaturation, $u_0 = -0.35$, -0.40, and -0.45. Figure 3.13 shows the morphology maps with three different initial supersaturation u_0. Note that the morphology map clearly depends on initial supersaturation. More specifically, as the absolute value of u_0 increases, the boundary between $\langle 100 \rangle$ growth and $\langle 110 \rangle$-like hyperbranched growth regions gradually moves upward. In other words, the $\langle 100 \rangle$ growth region shrinks when $|u_0|$ is large. On the other hand, the other two boundaries (i.e., the one between two hyperbranched growth regions and the one between $\langle 110 \rangle$-like hyperbranched and $\langle 110 \rangle$ growth regions) do not change significantly.
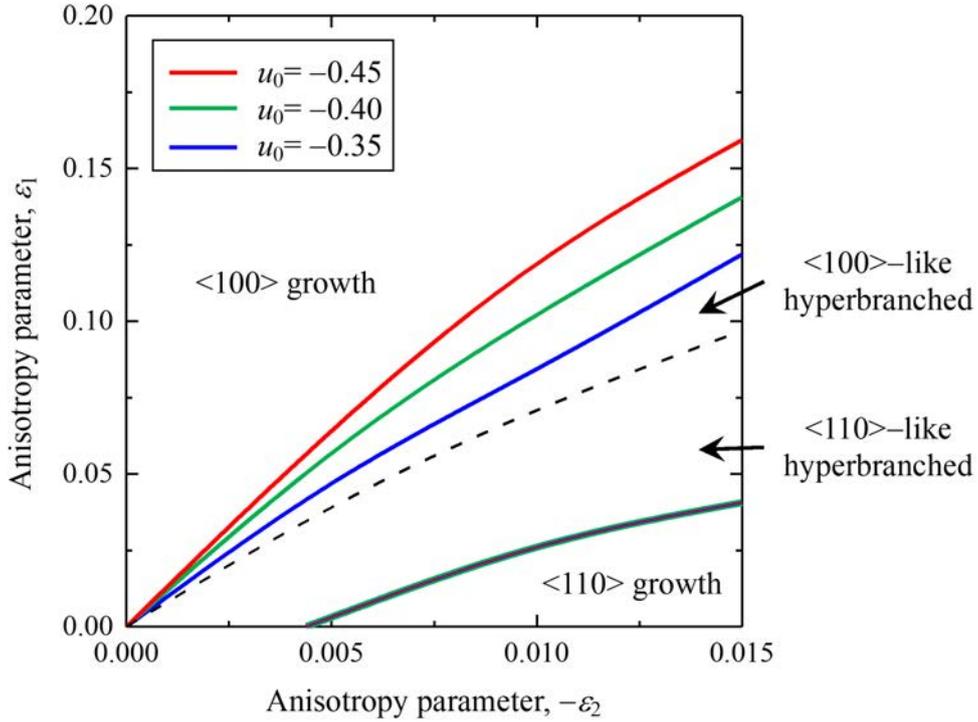
Fig. 3.13. Morphology maps with different initial supersaturation. The $\langle 100 \rangle$ growth region shrinks as initial supersaturation increases.

Figure 3.14 shows the morphology maps obtained for different partition coefficients, k was set to 0.1, 0.15 and 0.20. As k decreases, the boundary between $\langle 100 \rangle$ growth and $\langle 100 \rangle$-like hyperbranched growth regions moves upward, while the other two boundaries do not change significantly, similar to Fig. 3.13. Therefore, from

the morphology maps with different initial supersaturation and partition coefficient, $\langle 100 \rangle$ growth, typical growth of fcc-based alloy, is difficult to occur when the $|u_0|$ is large and/or k is small.

Fig. 3.14. Morphology maps with different partition coefficient. The $\langle 100 \rangle$ growth region shrinks as partition coefficient decreases.

The dependencies of the morphology map on solidification condition (u_0) and alloy system (k) can be understood as follows. The growth rate of the solid phase tends to increase as $|u_0|$ increases and k decreases. If the growth rate is high, the flat interface becomes unstable, then the branching occurs easily. In other words, the growth tends to be isotropic if the growth rate is high. Therefore, the solid tends to grow in various directions, when $|u_0|$ is large and/or k is small, resulting in appearance of hyperbranched growth. This explains the shrinkage of $\langle 100 \rangle$ growth region for large $|u0|$ and small k. However, the boundary in two types of hyperbranched growth regions and the boundary between $\langle 110 \rangle$-like hyperbranched and $\langle 110 \rangle$ growth regions do not depend on solidification condition and alloy system. Note that $\langle 110 \rangle$ has twelve equivalent directions in the cubic crystal, while $\langle 100 \rangle$ has only six equivalent directions. Namely, $\langle 110 \rangle$ dendrites and two hyperbranched morphologies already have many branches as compared with $\langle 100 \rangle$ dendrites. Hence, effects of solidification condition and alloy system on two hyperbranched growth

and $\langle 110 \rangle$ growth should be small. Thus, the boundary between two types of hyper-branched growth regions and the boundary between $\langle 110 \rangle$-like hyperbranched and $\langle 110 \rangle$ growth regions do not change with changes of u_0 and k.

3.6 Summary

In this chapter, first of all the simulation conditions of isothermal solidifications and acceleration method using GPU were described. In addition, morphological change of isothermally-solidified dendrite associated with transition in preferred growth direction was investigated by systematically changing anisotropy parameters. The growth morphologies are classified into four types, i.e. $\langle 100 \rangle$, $\langle 100 \rangle$-like hyperbranched, $\langle 110 \rangle$-like hyperbranched and $\langle 110 \rangle$ growth. From this classification, the omorphology map for isothermally-solidified microstructure was constructed. Finally, dependencies of this map on solidification condition and alloy system are also investigated by changing initial supersaturation and partition coefficient, respectively. It was found that the region of $\langle 100 \rangle$ growth, which is typical growth direction of fcc-based alloy, shrinks when initial supersaturation is large and/or partition coefficient is small.

References

[1] G. Ruetsch, M. Fatica, CUDA Fortran for scientists and engineers: best practices for efficient CUDA Fortran programming, Elsevier, 2013.

[2] J. Cheng, M. Grossman, T. McKercher, Professional Cuda C Programming, John Wiley & Sons, 2014.

[3] Y. Aoyama, J. Nakano, et al., Rs/6000 sp: Practical MPI programming, IBM Poughkeepsie, New York, 1999.

[4] T. Haxhimali, A. Karma, F. Gonzales, M. Rappaz, Orientation selection in dendritic evolution, Nature materials 5 (8) (2006) 660.

[5] J. Dantzig, P. Di Napoli, J. Friedli, M. Rappaz, Dendritic growth morphologies in Al-Zn alloys –PartII: phase-field computations, Metallurgical and Materials Transactions A 44 (12) (2013) 5532–5543.

[6] D. E. Knuth, The art of computer programming: sorting and searching, Vol. 3, Pearson Education, 1997.

Chapter 4

Morphological diversity of directironally-solidified microstructure

In this chapter, the morphological diversity of directionally-solidified microstructure associated with transition phenomenon of preferred growth direction will be explained. Also, the effect of solidification conditions on morphological change will be discussed.

4.1 Computational conditions of directional solidification

Phase-field equation for directional solidification (Eq. (2.79)) and diffusion equation with anti-trapping current(Eq. (2.78)) were solved in same way with isothermal solidification process. Three-dimensional simulations for one-half of a directionally-solidified dendrite were performed. The computational system is cuboid shape (see Fig. 4.1) and the systems is initially occupied by liquid phase with the initial solid seed put in the center of x-y plane. The mirror boundary condition was applied on x-z plane at $y = 0$ and $y = L_y$, periodic boundary condition was applied on y-z plane at $x = 0$ and $x = L_x$ and zero-flux boundary condition was applied on x-y plane at $z = 0$ and $z = L_z$, where L_x, L_y and L_z is the size of x,y and z direction, respectively. The temperature gradient, G, was set parallel to z direction and

pulling speed, V_p, was also set parallel to z direction, but is opposite direction to temperature gradient.
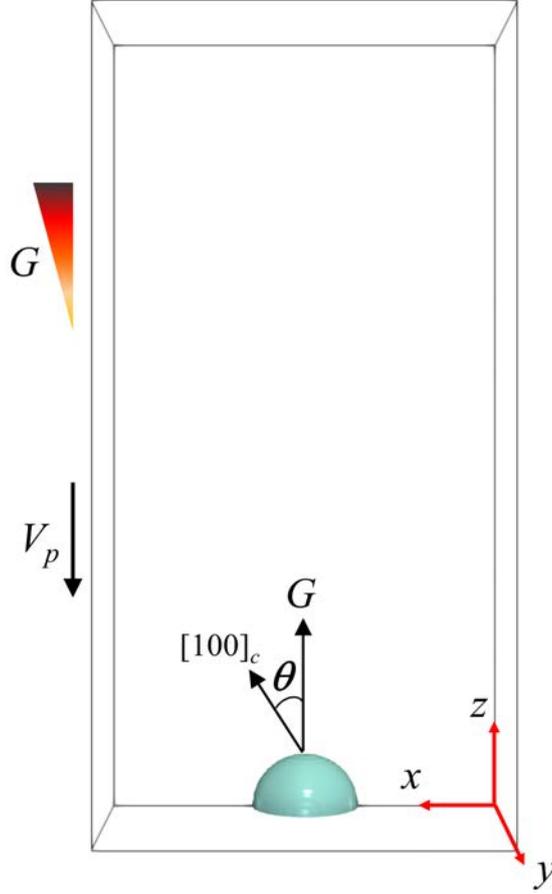
Fig. 4.1. Schematic representation of computational domain for directional solidification.
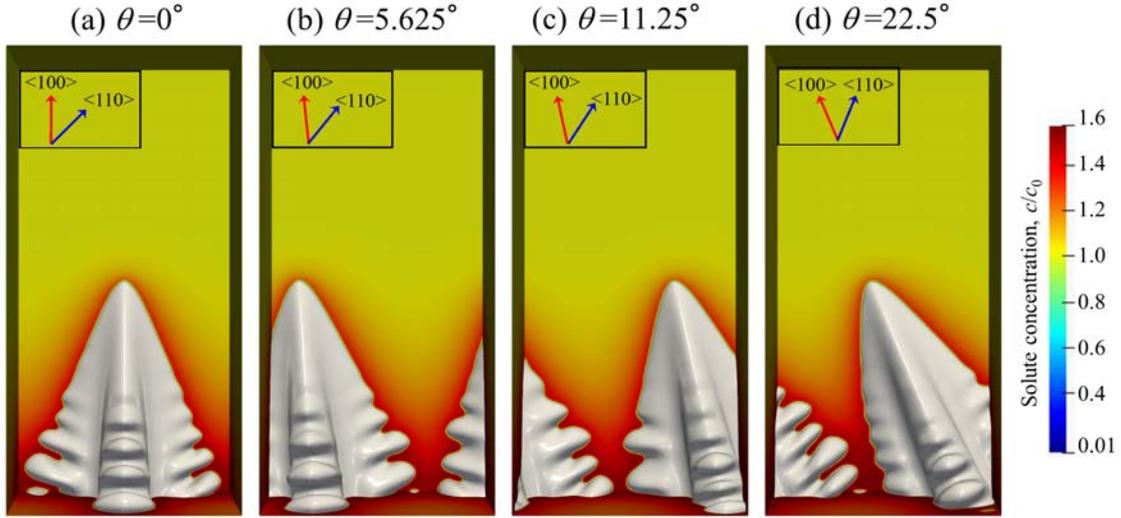
In the simulations of directional solidification, the same model alloy was employed as the isothermal solidification. By the normalization of the spatial and time scales by d_0 and d_0^2/D_L, respectively, the problem depends only on four parameters, i.e., the initial supersaturation u_0, the partition coefficient k, anisotropy parameters ε_1 and ε_2, the temperature gradient G and the pulling speed V_p. Also the angle between $\langle 100 \rangle$ and thermal flow direction (z direction in Fig. 4.1) was systematically changed θ, then growth morphology and tip undercooling with different θ were investigated. The parameters used in the simulation are summarized in Table 4.1. The numbers of grid points was set to $224 \times 112 \times 448$ or $224 \times 80 \times 448$ and Δx was set to 0.3125 μm in case of $V_p = 500$ $\mu m/s$ and $G = 10$ K/mm which is also depends on the solidification conditions.

Table 4.1: Physical parameters used in directional solidification.

Physical parameter	Value
Anisotropy paramters, ε_1	0 - 0.15
Anisotropy paramters, ε_2	-0.01 - 0
Initial supersaturation, u_0	-0.30
Partition coefficient, k	0.10
Temperature gradient, G	5, 10, 15 [K/mm]
Pulling speed, V_p	100, 500, 1000 [μm/s]
Angle between $\langle 100 \rangle$ and thermal flow direction, θ	0-45 [degree]

## 4.2 Classification of growth morphologies

Growth morphologies of directionally-solidified microstructure were classified by changing anisotropy parameters ε_1 and ε_2 and the angle between $\langle 100 \rangle$ of crystal and heat flow direction θ. Figure 4.2 shows the snapshots of dendrites calculated for $\varepsilon_1 = 0.1$ and $\varepsilon_2 = 0$ with different θ and the solidification condition was set to $u_0 = -0.3$, $k = 0.1$, $G = 10$ K/mm and $V_p = 500$ μm/s. In this case, all dendrites seem to grow along $\langle 100 \rangle$ regardless of the value of θ. These are the typical $\langle 100 \rangle$ dendrite usually observed in fcc-based alloys when the contribution of ε_1 is dominant. In real solidification process, there are many solid nuclei at the beginning of solidification. It can be anticipated that most favorably oriented crystals will grow preferentially in long period of solidification. This orientation was identified by the farthest grown direction in pulling direction and it was defined as preferred growth direction in directional solidification. This also corresponds to the microstructure with the lowest tip undercooling. Figures 4.3 shows tip undercooling in case of $\varepsilon_1 = 0.1$ and $\varepsilon_2 = 0$. As shown in Fig. 4.3, tip undercooling ΔT_{tip} converges to a constant value by the solidification time passing which means that the solidification reached the steady-state growth. In this case, dendrite tip undercooling was lowest when $\theta = 0°$. It means that the dendrite growth farthest when $\theta = 0°$. Therefore, one can find that the preferred growth direction is $\langle 100 \rangle$ with $\theta = 0°$ in this condition and anisotropy parameters.

Fig. 4.2. Directionally-solidified microstructures obtained by phase-field simulations for $u_0 = -0.3$, $k = 0.1$, $G = 10$ K/mm and $V_p = 500$ μm/s. Calculated by different θ with fixed anisotropy parameters, $\varepsilon_1 = 0.1$ and $\varepsilon_2 = 0$.
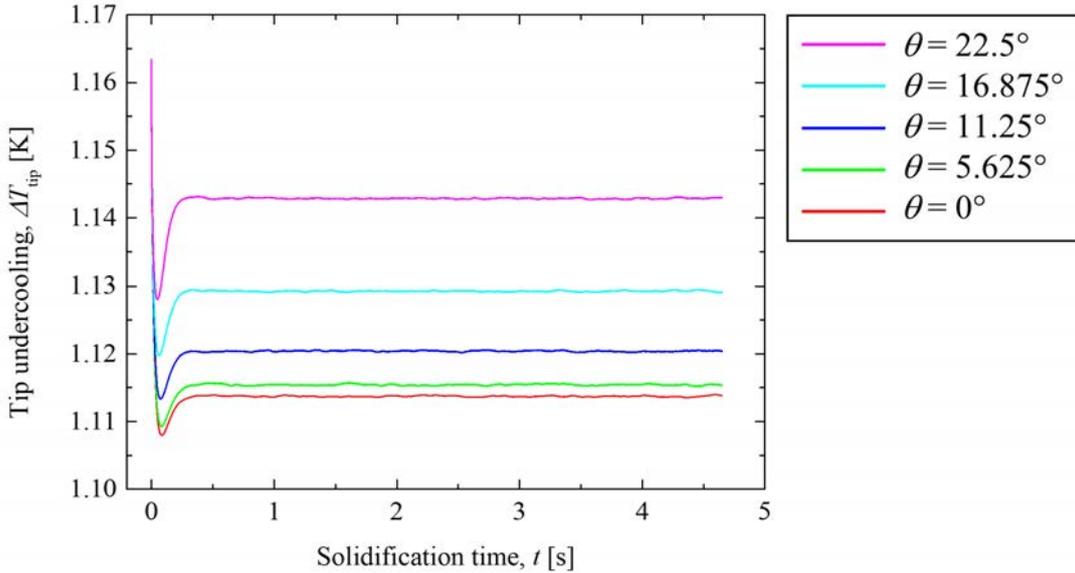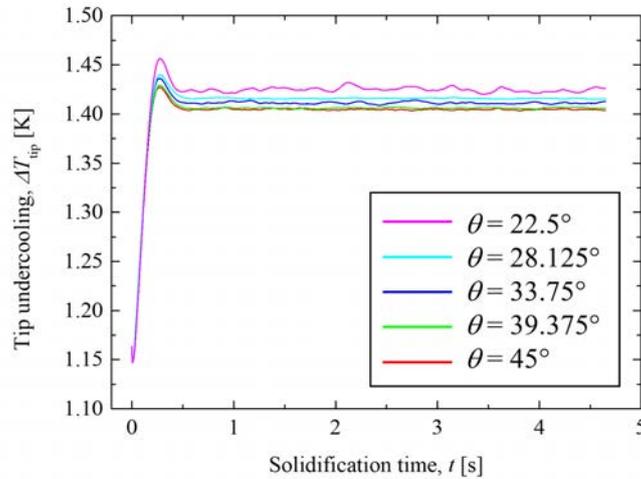

Fig. 4.3. Tip undercooling with solidification time in case of $(\varepsilon_1, \varepsilon_2) = (0.1, 0)$. In this case, dendrites preferentially grow in $\langle 100 \rangle$, since ΔT_{tip} is lowest when $\theta = 0°$.
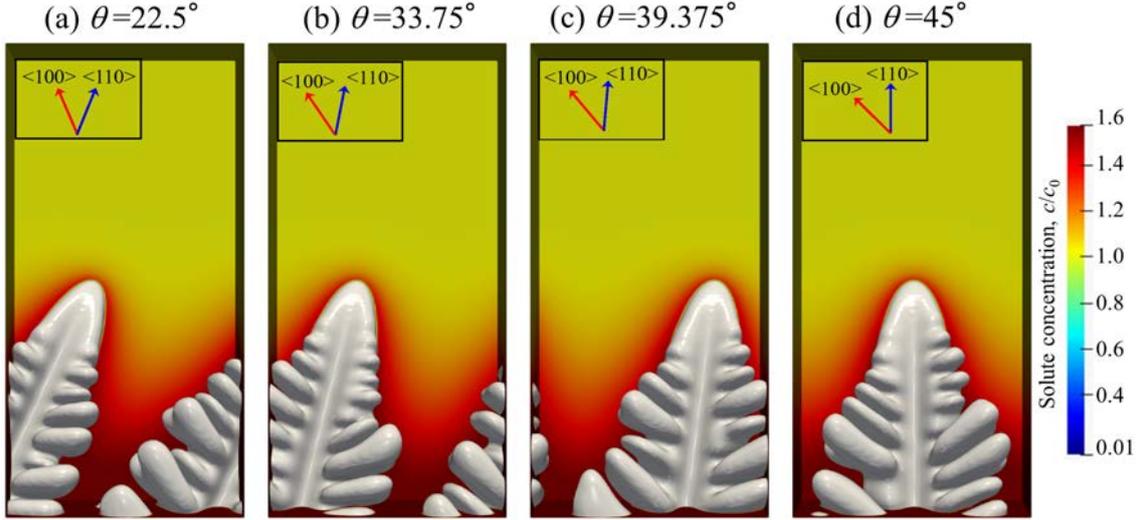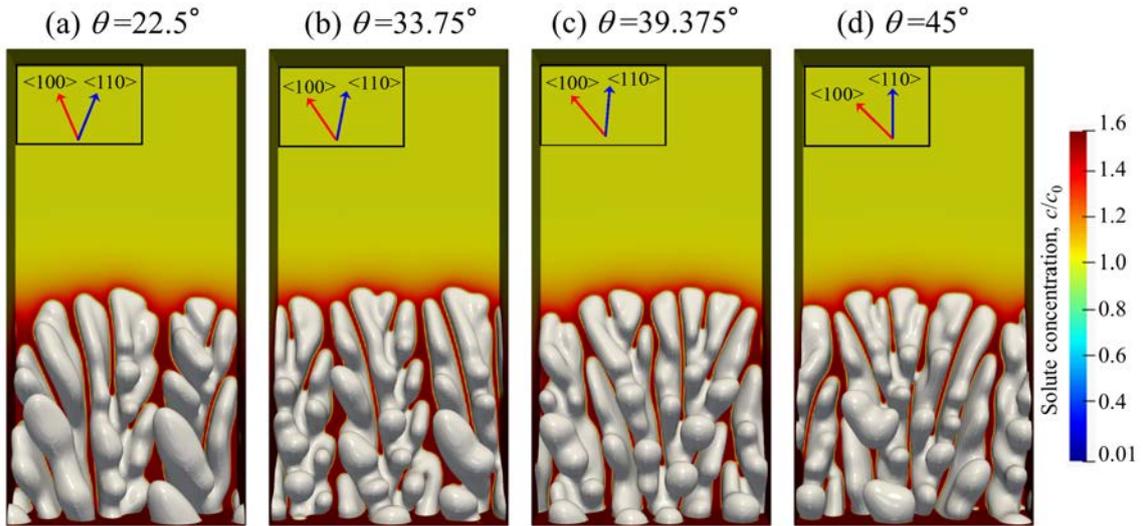
Fig. 4.4. Directionally-solidified microstructures obtained by phase-field simulations for $u_0 = -0.3$, $k = 0.1$, $G = 10$ K/mm and $V_p = 500$ μm/s. Calculated by different θ with fixed anisotropy parameters, $\varepsilon_1 = 0$ and $\varepsilon_2 = -0.01$.

Figure 4.4 represents the simulated microstructures in case of $\varepsilon_1 = 0$ and $\varepsilon_2 = -0.01$ with different θ and the solidification condition was set to $u_0 = -0.3$, $k = 0.1$, $G = 10$ K/mm and $V_p = 500$ μm/s. In this case, dendrites seem to grow along $\langle 110 \rangle$ in all θ. This growth morphology was observed in the directional solidification of Al-Zn alloy with high Zn concentration range [1]. The contribution of ε_2 is dominant in this case. The preferred growth direction was determined by tip undercooling represented as Fig. 4.5. Tip undercooling converges to constant value, and it has lowest value when $\theta = 45°$. Therefore, the growth type was determined as $\langle 110 \rangle$ dendrite and preferred growth direction as $\langle 110 \rangle$.
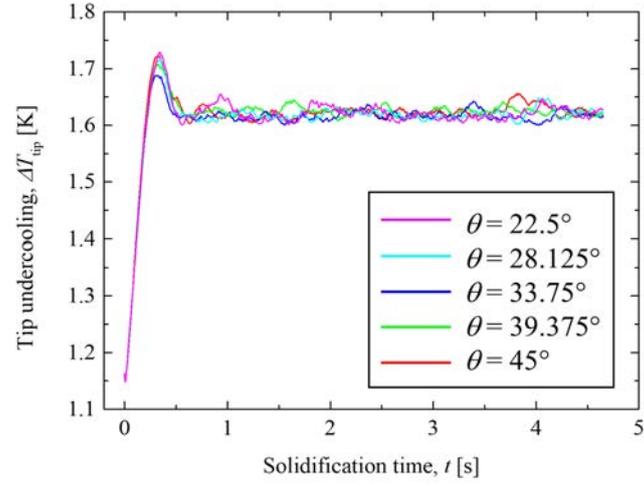

Fig. 4.5. Tip undercooling with solidification time in case of $(\varepsilon_1, \varepsilon_2) = (0, -0.01)$. Dendrites preferentially grow in $\langle 110 \rangle$, since ΔT_{tip} is lowest when $\theta = 45°$.

The seaweed growth was observed in directional solidification of Al-Zn alloy conducted by Haxhimali et al. [1] at the intermediated Zn concentration range (around 25 and 55 mass% Zn). In phase-field simulations conducted by Dantzig et al. [2], the seaweed growth was also observed when anisotropy parameters took the intermediate value between ε_1-dominant and ε_2-dominant cases. Similarly, in this study, the seaweed growth was observed when the anisotropy parameters were set to $\varepsilon_1 = 0.05$ and $\varepsilon_2 = -0.005$ as shown in Fig. 4.6. The other simulation conditions were set as follows: $u_0 = -0.3$, $k = 0.1$, $G = 10$ K/mm and $V_p = 500$ μm/s. In this case, regardless of the value of θ, all microstructures formed seaweed structure. The difference between dendrite growth and seaweed growth is that tip undercooling continues to fluctuate in the latter case as shown in Fig. 4.7. This is because the tip of the seaweed structure continues to split. This oscillation in tip undercooling is characteristic of the seaweed growth as observed in Refs. [3,4] that investigated seaweed structure in directional solidification experiments of transparent alloy.

Fig. 4.6. Directionally-solidified microstructures obtained by phase-field simulations for $u_0 = -0.3$, $k = 0.1$, $G = 10$ K/mm and $V_p = 500$ μm/s. Calculated by different θ with fixed anisotropy parameters, $\varepsilon_1 = 0.05$ and $\varepsilon_2 = -0.005$.

Fig. 4.7. Tip undercooling with solidification time in case of $(\varepsilon_1, \varepsilon_2) = (0.05, -0.005)$. ΔT_{tip} vibrate due to the tip splitting of seaweed structure.

4.3 Morphology map of directionally-solidified microstructure

As described in section 5.2, growth morphologies of directionally-solidified microstructure were classified into three types by quantitative phase-field simulations. From this classification, morphology map was constructed. Figure 4.8 shows the morphology map of directionally-solidified structure in case of $u_0 = -0.3$, $k = 0.1$, $G = 10$ K/mm and $V_p = 500$ μm/s. The $\langle 100 \rangle$ growth and $\langle 110 \rangle$ growth regions appear in the upper-left and the lower-right parts, respectively, which is similar to the morphology map for isothermally-solidified structure. Note that the boundary line indicated by the dotted line in Fig. 4.8 is a boundary extend from solid boundary line due to lack of the investigation area.
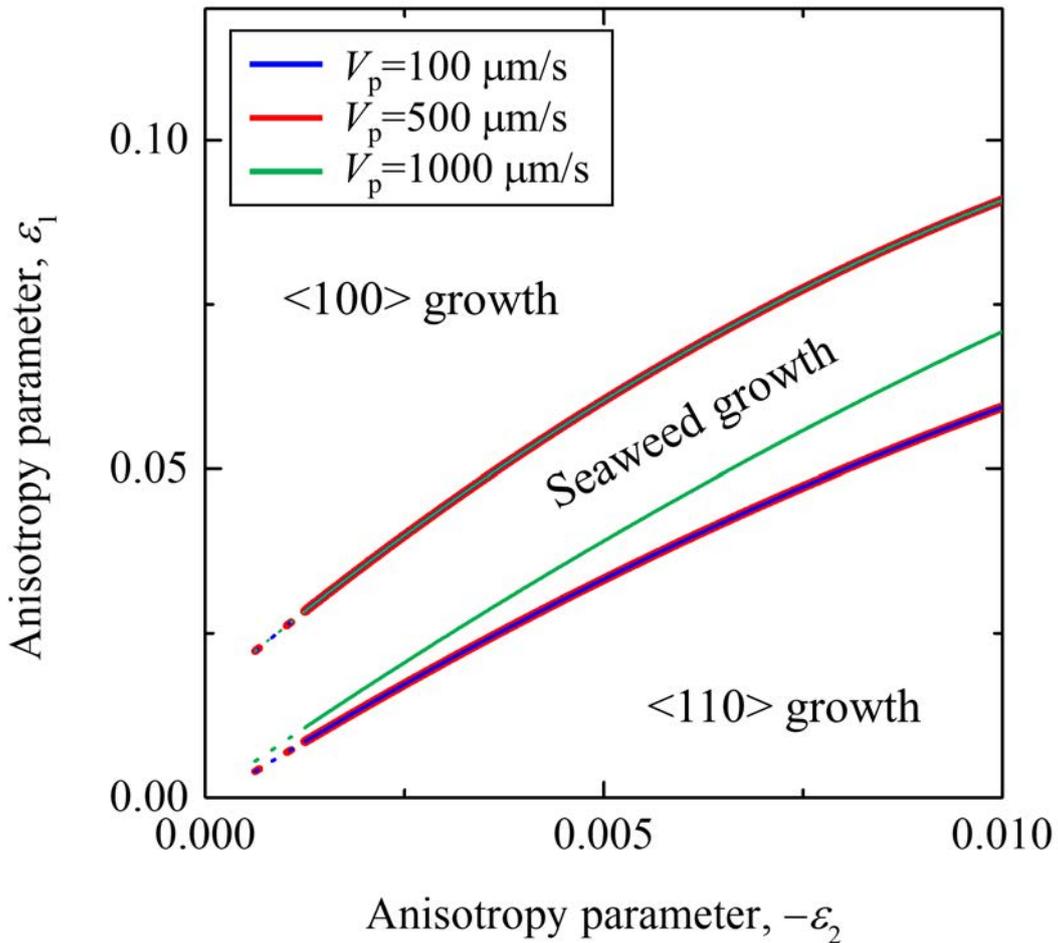
The morphology map for directionally-solidified microstructure, was constructed for the first time through extensive investigation of ε_1, ε_2 and θ in this study. From this map, we can predict the solidification structure of alloys with different anisotropy parameters. Reversely, it may be also possible to deduce the anisotropy parameters of alloy from the comparison of actual solidification structures with the morphology selection map.
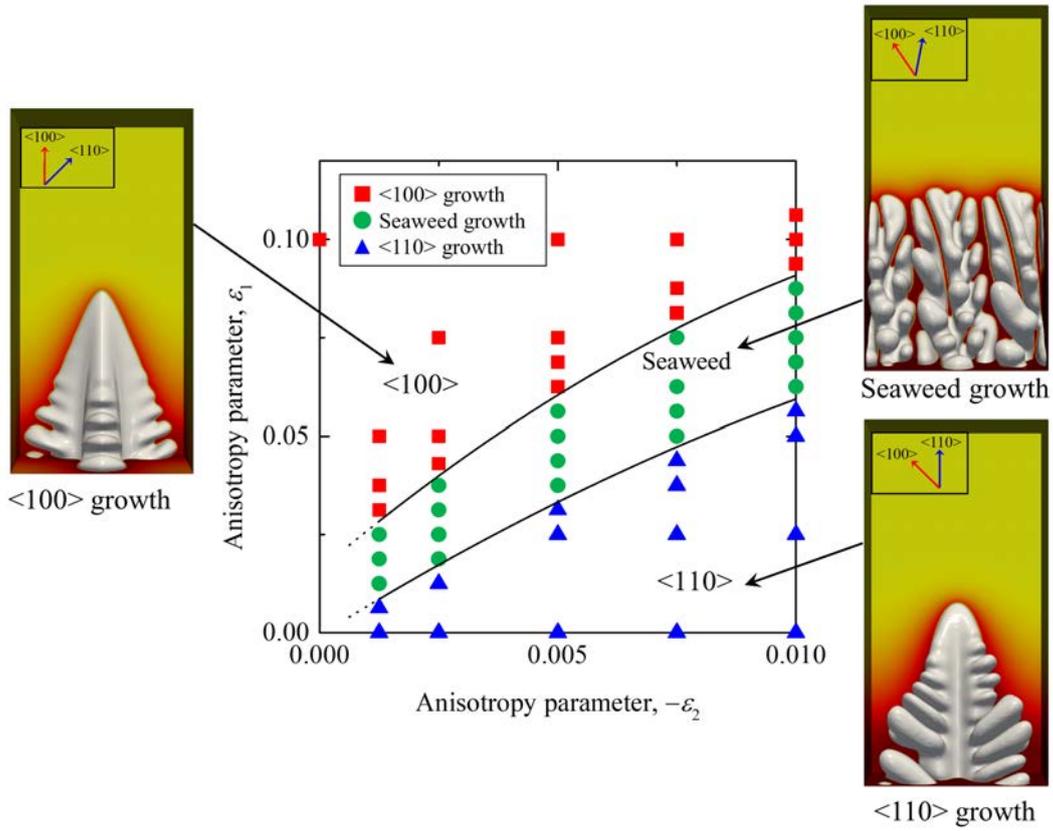
Fig. 4.8. Morphology map of directionally-solidified microstructure in case of $u_0 = -0.3$, $k = 0.1$, $G = 10$ K/mm and $V_p = 500$ μm/s. This map shows what kind of morphology will be formed by directional solidification with different sets of anisotropy parameters.

4.4 Effects of solidification conditioins on morphology map

In this study, to investigate the influence of solidification condition the simulations of directional solidification were carried out for three different solidification conditions. First, to investigate the effect of pulling speed on morphology maps, phase-filed simulations were performed at different pulling speed with fixed temperature gradient. Figure 4.9 shows the morphology map for different pulling speed 100, 500 and 1000 μm/s with fixed temperature gradient $G = 10$ K/mm.

Fig. 4.9. Morphology map of directionally-solidified microstructure with different pulling speed, other conditions are fixed as $u_0 = -0.3$, $k = 0.1$, $G = 10$ K/mm. Only the boundary between seaweed and $\langle 110 \rangle$ growth slightly changes.

Note that only the boundary between seaweed growth and $\langle 110 \rangle$ growth region slightly changed. This result indicates that as the pulling speed decreases, the sea-

weed growth region becomes wider. That is, the seaweed growth hardly occurs easily as pulling speed increases. It can be understood that when the pulling speed decreases, the curvature of the dendrite tip becomes larger, that is, the solid-liquid interface becomes flat, making the interface easier to split, so the the morphologically unstable seaweed structure is easily formed. According to early work on Al-32mass%Zn alloy [5], the seaweed structure forms at low pulling speed ($\sim$150 μm/s), while $\langle 110 \rangle$ growth columnar dendrite forms at high pulling speed (1000 μm/s). That is, the morphology map obtained in this study shows similar tendency with early work by Chen et al. [5].

In addition, in this study, the effect of the temperature gradient on morphology map was also investigated. Phase-field simulations were conducted and morphology maps were constructed for different temperature gradient 5, 10, 15 K/mm with fixed pulling speed $V_p = 500$ μm/s. However, there was no change in morphology map in this range of temperature gradient. Since the temperature gradient also affects the growth morphology of solidification microstructure [6, 7], further investigation should be carried out in other pulling speed or in a wider range of temperature gradient.

4.5 Summary

In this chapter, morphological change of directionally-solidified microstructure associated with transition in preferred growth direction were investigated by systematically changing anisotropy parameter and the angle between $\langle 100 \rangle$ crystallographic orientation and heat flow direction. The growth morphologies were classified into three types, i.e. $\langle 100 \rangle$, seaweed and $\langle 110 \rangle$ growth. From this classification, the morphology map for directionally-solidified microstructure was constructed. Furthermore, dependence of this map on solidification conditions, pulling speed and temperature gradient, was investigated. It was found that the seaweed growth region in the space of ε_1 and ε_2 slightly becomes wider as the pulling speed decreases. It was also found that there was no change in morphology map in the range of temperature gradient $5 - 15$ K/mm with fixed pulling speed $V_p = 500$ μm/s.

References

[1] T. Haxhimali, A. Karma, F. Gonzales, M. Rappaz, Orientation selection in dendritic evolution, Nature materials 5 (8) (2006) 660.

[2] J. Dantzig, P. Di Napoli, J. Friedli, M. Rappaz, Dendritic growth morphologies in Al-Zn alloys –PartII: phase-field computations, Metallurgical and Materials Transactions A 44 (12) (2013) 5532–5543.

[3] B. Utter, R. Ragnarsson, E. Bodenschatz, Alternating tip splitting in directional solidification, Physical review letters 86 (20) (2001) 4604.

[4] B. Utter, E. Bodenschatz, Dynamics of low anisotropy morphologies in directional solidification, Physical review E 66 (5) (2002) 051604.

[5] Z. Chen, E. Wang, X. Hao, Microstructure and orientation evolution in unidirectional solidified Al–Zn alloys, Materials Science and Engineering: A 667 (2016) 1–8.

[6] W. Kurz, D. J. Fisher, Fundamentals of solidification, Vol. 1, Trans Tech Publications Aedermannsdorf, Switzerland, 1986.

[7] J. A. Dantzig, M. Rappaz, Solidification, EPFL press, 2009.

Chapter 5

Estimation of anisotropy parameter of solid-liquid interfacial energy

In this chapter, it will be described that a method of estimating anisotropy parameters of solid-liquid interfacial energy using inverse analysis. This method is an inverse analytical approach that combined phase-field simulation and machine learning, each of which will be described in detail. In addition, the estimation results will be discussed.

5.1 Idea of the estimation method

In this study, instead of directly calculating the anistoropy parameters of solid-liquid interfacial energy, a method of estimating them from the morphology of solidification microstructures using inverse analysis approach was proposed. First, the interfacial shape distribution (ISD) maps that can characterize the morphology of solidification microstructure at different values of $(\varepsilon_1, \varepsilon_2)$ were obtained from phase-field simulations of fcc model alloy for isothermal solidification. Then those maps were trained through machine learning to match the relationship between ISD map and $(\varepsilon_1, \varepsilon_2)$. Using machine learning model, $(\varepsilon_1, \varepsilon_2)$ can be estimated from a given ISD map. In following sections, details of ISD map and machine learning will be described.

5.2 Methodology

5.2.1 Phase-field simulations

To generate free-growing dendrite during isothermal solidification of a dilute binary alloy, phase-field simulations were carried out by solving Eqs. (2.77) and (2.78). Note that the length and time scales in Eqs. (2.77) and (2.78) were normalized by d_0 and d_0^2/D_l, respectively. Thus, except for the two anisotropy parameters ε_1 and ε_2, the growth problem in this system depends only on three parameters, namely k, q_s , and initial supersaturation of u_0.

Equations (2.77) and (2.78) were discretized using a second-order finite- difference scheme for space. Time integration was performed using the first-order Euler scheme. To reduce the computational cost, only one- eighth of the system was considered by applying the same boundary conditions as described in Section 3.1. An initial solid seed was placed at the origin of the 3D computational domain occupied by the liquid phase to simulate a free-growing dendrite under isothermal conditions.

In this study, a model alloy system with $k = 0.1$ and $q_s = 10^{-4}$ was employed. The computational domain was discretized into 512^3 grid points. The normalized grid spacing Δx was set to 13 and η was set as $1.2\Delta x$. The initial supersaturation was set as $u_0 = -0.3$. The step size of the normalized time was set as $\Delta t = 24.14$, and all simulations were performed until $t = 50000\Delta t$. These values were selected to achieve a balance between the accuracy and computational cost in the preliminary simulations. All computations were accelerated using single graphics processing units (GPU), NVIDIA Tesla P100.

5.2.2 Curvedness and shape factor

The morphology of the entire solidification microstructure can be characterized by the statistical nature of the local interface morphology in terms of curvedness C and shape factor S [1]. C denotes the degree to which the interface is curved and is defined as follows:

$$C = \sqrt{\frac{\kappa_1^2 + \kappa_2^2}{2}} \tag{5.1}$$

where κ_1 and κ_2 are the maximum and minimum curvatures of the local interface, respectively. S represents the shape of the local interface as follows:

$$S = \frac{2}{\pi} \tan^{-1} \left(\frac{\kappa_1 + \kappa_2}{\kappa_1 - \kappa_2} \right) \tag{5.2}$$

The interface with $S = 0, \pm 0.5$ and ± 1 correspond to the saddle point, cylindrical, and the spherical shape, respectively.

The principal curvature can be computed from the mean H and Gaussian curvature K:

$$H = \frac{\kappa_1 + \kappa_2}{2} \tag{5.3}$$

$$G = \kappa_1 \kappa_2 \tag{5.4}$$

H and K can be calculated from the ψ-field [2]:

$$\begin{aligned} H =& [\psi_x^2(\psi_{yy} + \psi_{zz}) + \psi_y^2(\psi_{xx} + \psi_{zz}) + \psi_z^2(\psi_{xx} + \psi_{yy}) \\ & - 2(\psi_{xy}\psi_x\psi_y + \psi_{yz}\psi_y\psi_z + \psi_{zx}\psi_z\psi_x)]/2|\nabla\psi|^3 \end{aligned} \tag{5.5}$$

$$\begin{aligned} K =& [\psi_x^2(\psi_{yy}\psi_{zz} - \psi_{yz}^2) + \psi_y^2(\psi_{zz}\psi_{xx} - \psi_{zx}^2) + \psi_z^2(\psi_{xx}\psi_{yy} - \psi_{xy}^2) \\ & - 2\psi_x\psi_y(\psi_{zz}\psi_{xy} - \psi_{zx}\psi_{yz}) \\ & - 2\psi_y\psi_z(\psi_{xx}\psi_{yz} - \psi_{xy}\psi_{zx}) \\ & - 2\psi_z\psi_x(\psi_{yy}\psi_{zx} - \psi_{yz}\psi_{xy})]/|\nabla\psi|^4 \end{aligned} \tag{5.6}$$

where ψ_i and ψ_{ij} represent the first and second derivatives of ψ, respectively, with resepect to the direction(s) denoted by the subscript.

The relationship between the morphology of local interface and these two quantities is represented in Fig. 5.1.
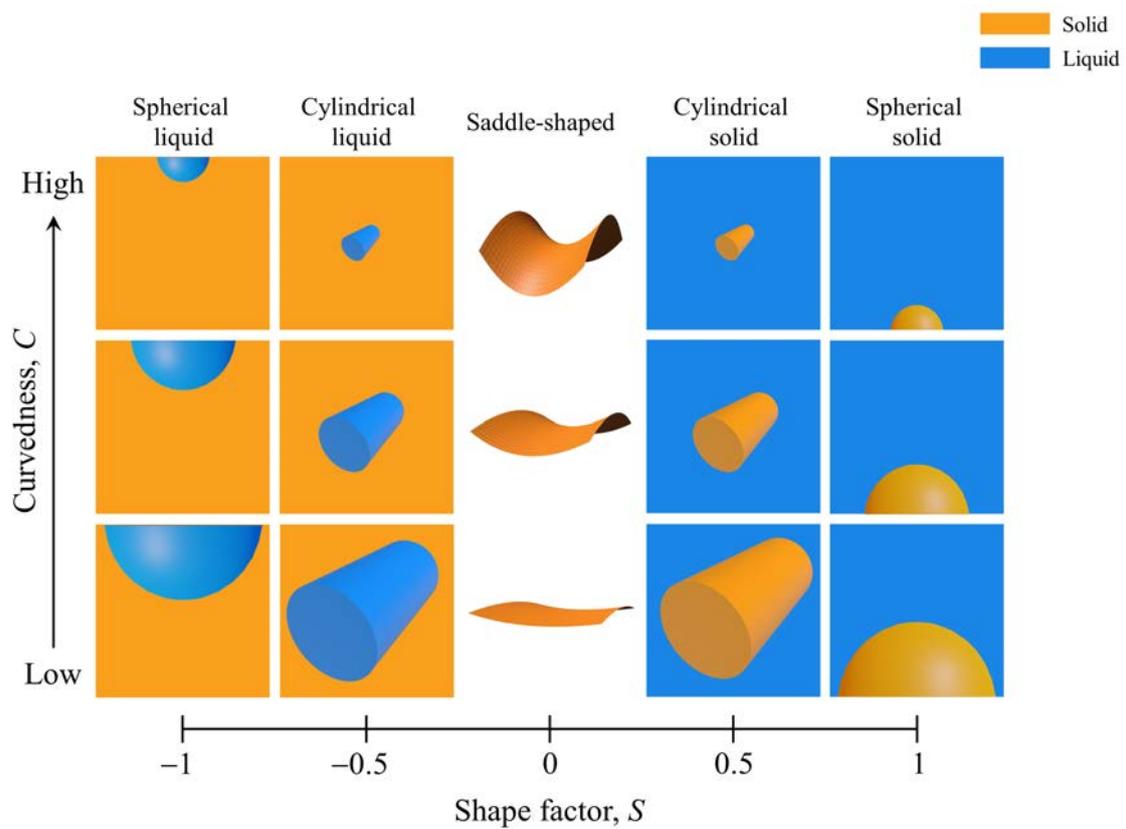
Fig. 5.1. Relation between morphology and curvdeness and shape factor. Solid and liquid phases are represented in orange and skyblue, respectively.

5.2.3 Interfacial shape distribution (ISD)

Gibbs et al. [3] proposed a method to characterize the morphology of solidification microstructure as interfacial shape distribution (ISD) map by calculating the existing probability of C and S values of the local interface as illustrated in Fig. 5.1.

Figure 5.2 shows an example of the dendrite at $t = 40000\Delta t$ simulated for $(\varepsilon_1, \varepsilon_2) = (0.1, 0)$. The local interface of the dendrite is colored according to the values of (a) $C/\langle C \rangle$ and (b) S. Here, $\langle C \rangle$ represents the average curvedness at a given time. C takes high values at the tip and edges of the primary and secondary arms. S exhitbits +1, +0.5, and –0.5 at the tip of the arms, edges of the secondary arms, and primary arm trunks (or roots of the secondary arm), respectively. The existing probability of the local morphology of the interface is summarized in the ISD map (Fig. 5.2(c)). By introducing this two-dimensional map called ISD, the details of the 3D dendrite morphology can be represented
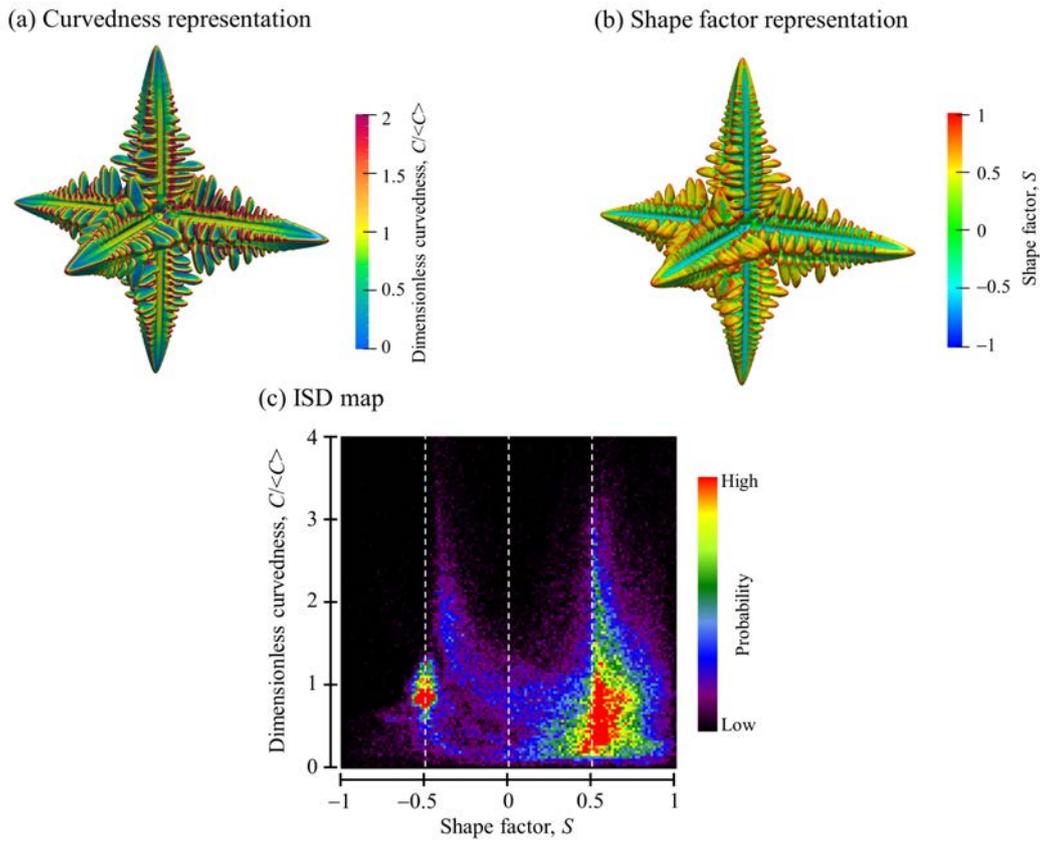
Fig. 5.2. (a,b) three-dimensional dendrite structure and (c) the corresponding ISD map at $t = 40000\Delta t$ simulated for $(\varepsilon_1, \varepsilon_2) = (0.1, 0)$. The local interface of the dendrite is colored according to the values of (a) $C/\langle C \rangle$ and (b) S.

5.2.4 Convolutional neural network (CNN)

Recently, machine learning has emerged as an important technology in various fields [4] and various machine learning models have also being applied in the field of material science [5–9]. Convolutional neural network (CNN), an artificial neural network variant suitable for processing data, which has a grid topology structure, can be applied to image recognition, classification, segmentation etc. [10–12] . In this study, CNN was utilized in this study to develop an approach for the inverse analysis of ε_1 and ε_2 from the ISD map. The CNN typically consists of three layers, namely, convolutional, pooling, and fully connected layers. The convolution layer performs a sliding dot product of the convolution kernel with the input matrix of the layer. The convolutional kernel is a matrix consisting of learnable parameters, and the convolution operation produces feature maps that are utilized as the input of the next layer. The learnable parameters are trained to decrease the loss function, such as the mean squared error (MSE) between the training data and predicted values. A pooling layer is used to reduce the dimensions of the matrix. The most common layer is the max-pooling layer, which selects the maximum value from each local components of the matrix. The fully connected layer connects every input value to each output value in the next layer, similar to a multi-layer perception neural network. The prediction accuracy of the CNN depends on how these layers are stacked and should generally increase with increasing depth of the model, i.e., the number of layers.

The CNN architecture is presented in Fig. 5.3. The input image is the ISD map with a size of $128 \times 128 \times 1$, followed by three operations, each consisting of two convolution layers with a (3,3) kernel size, a zero-padding and 1 stride and 1 max-pooling layer of (2,2), one fully connected layer, and the output layer for continuous values of ε_1 and ε_2. Here, (3,3) and (2.2) represents the size of matrix employed for convolution and max-pooling, respectively. These sizes and the number of layers, etc. are called hyperparameters that affect the accuracy of machine learning model. These hyperparameters were tuned using the validation dataset as described later. A machine learning framework known as PyTorch 1.7.0 was employed. Adam and MSE were selected as the optimizer and loss function, respectively. The learning rate was set to 10^{-5} and the training was performed for 1000 epochs that was determined based on a balance between the reduction of MSE and overfitting.
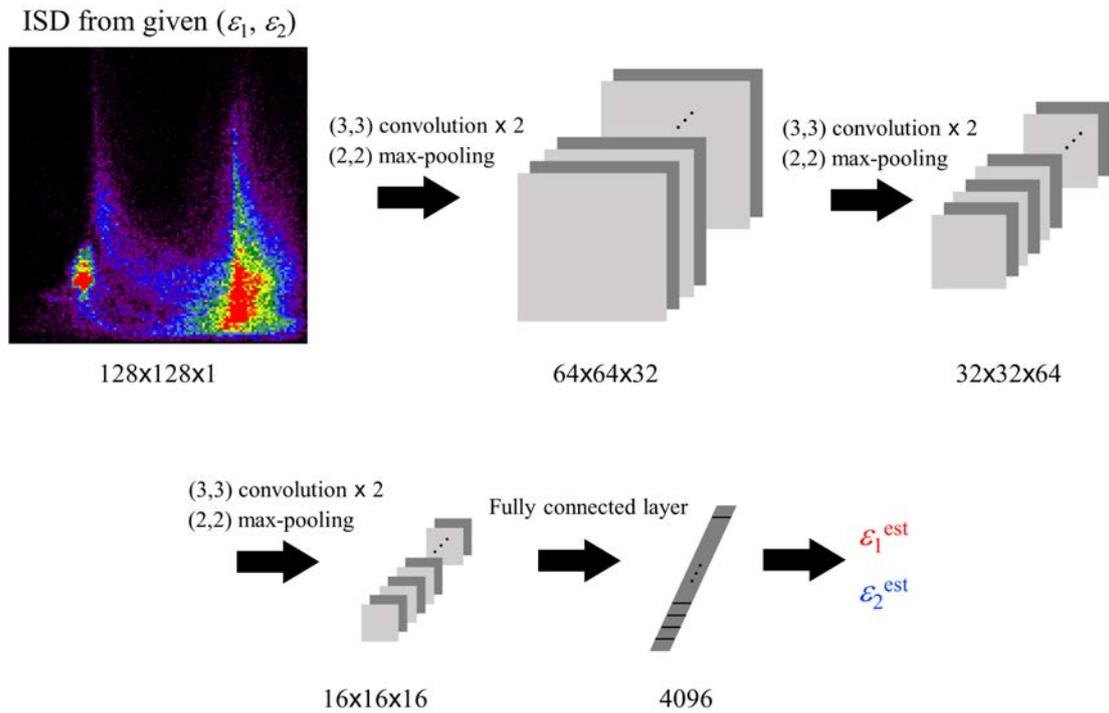
Fig. 5.3. CNN architecture used in this study. All convolution operations were performed with zero-padding and 1 stride and max-pooling was performed with 1 stride.

For the training, we used four datasets consisting of 49, 100, 196 and 400 sets of ε_1 and ε_2, which were uniformly sampled from the range of $\varepsilon_1 = [0, 0.1]$ and $\varepsilon_2 = [-0.01, 0]$, as shown in Fig. 5.4 As described in the preceding sections, the quantitative phase-field simulation of the free growth of a single dendrite under isothermal conditions was performed for each set of ε_1 and ε_2 until $t = 50000\Delta t$ and the ISD maps were calculated every $500\Delta t$. Namely, 100 ISD maps were obtained for each set of ε_1 and ε_1. Hence, the training datasets used in this study consist of 4900, 10000, 19600, 40000 ISD maps. The training dataset was divided into two subsets; one was used for training and the other was used for tuning the hyperparameters. The latter set is called the validation dataset. We used 80% of the training data for training and 20% for validation. The test dataset was obtained by randomly sampling 100 sets of ε_1 and ε_2 as shown in Fig. 5.4. Note that the region of $\varepsilon_1 < 0.01$ or $\varepsilon_2 > -0.001$ was avoided when sampling the test data. This is because the preliminary tests showed that estimations in this region involve large errors, and these values of ε_1 and ε_2 are not commonly observed in metallic systems [13]. Because the ISD maps of the test data were obtained every $500\Delta t$ for each set of ε_1 and ε_2, the test dataset consisted of a total of 10000 ISD maps. Since the test data were not employed to construct the CNN model including the hyperparameters, the generalization error can be estimated using the test dataset.
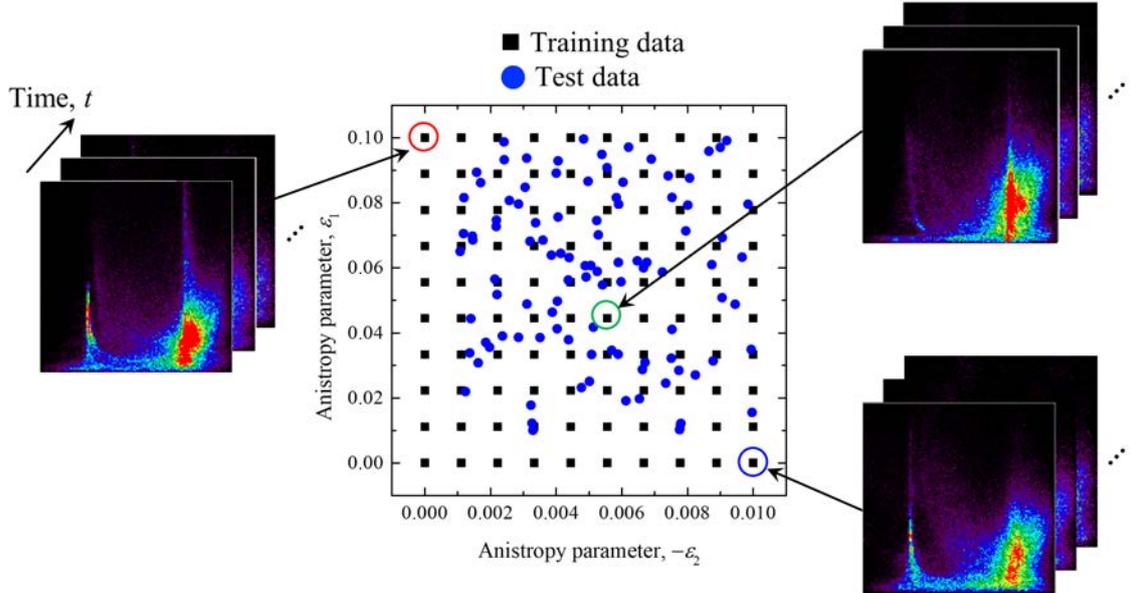

Fig. 5.4. Illustration of sampling the training and test datasets in the $\varepsilon_1 - \varepsilon_2$ space.

5.3 Results and discussions

5.3.1 Growth morphologies and ISD maps

The time evolution of the dendrite structure and corresponding ISD map are shown in Fig. 5.5. These are the results for $(\varepsilon_1, \varepsilon_2) = (0.1, 0)$. Starting from the initial spherical shape, the solid exhibits a dendritic structure with well-developed primary arms at $t = 10000\Delta t$. In the ISD map at $t = 10000\Delta t$, several peaks appear at $S \cong 0.5$, which mainly originate from the interfaces at the edges of the primary arms. The high probabilities at $C/\langle C \rangle \cong 0$ and $S \cong -0.5$ are associated with the side surface of the primary arms. In addition, the secondary arms begin to appear after $t = 10000\Delta t$ and were well developed at $t = 40000\Delta t$, with a dominant contribution in the ISD map.
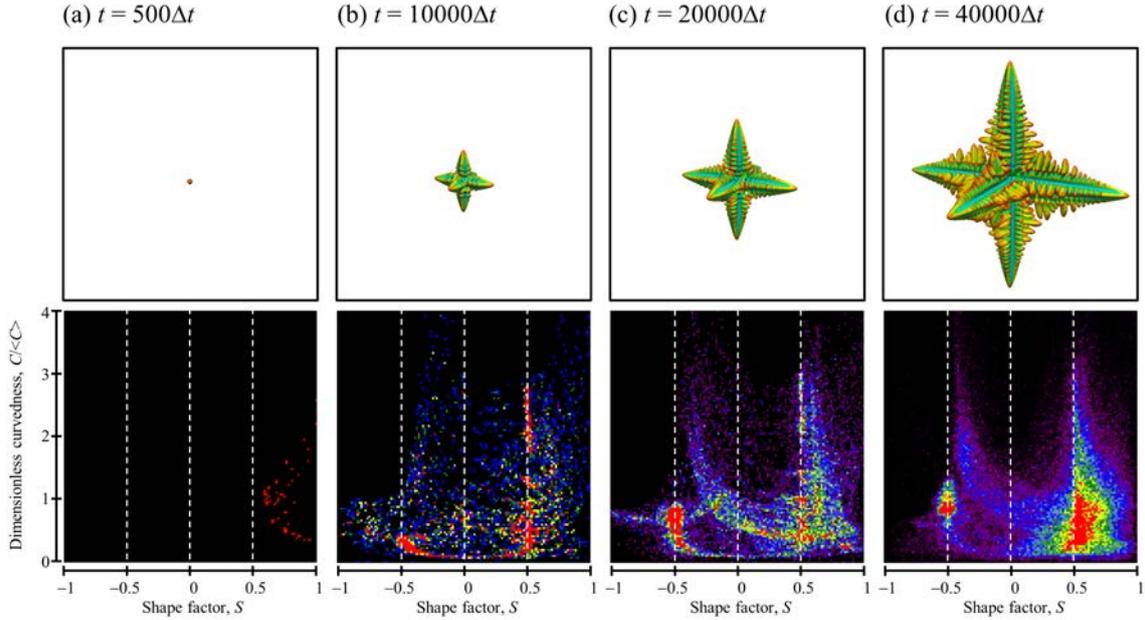

Fig. 5.5. Time evolution processes of the dendrite structure (upper) and corresponding ISD map (lower) for $(\varepsilon_1, \varepsilon_2) = (0.1, 0)$.

As reported in early studies [14, 15], different growth modes arise depending on the values of ε_1 and ε_2. The dendrite structures via different growth modes and the corresponding ISD maps at $t = 40000\Delta t$ are compared in Fig. 5.6, where the $\langle 100 \rangle$ growth simulated for $(\varepsilon_1, \varepsilon_2) = (0.1, 0)$, hyperbranched growth for $(\varepsilon_1, \varepsilon_2) = (0.05, -0.005)$, and $\langle 110 \rangle$ growth for $(\varepsilon_1, \varepsilon_2) = (0, -0.01)$. The growth morphology is very different owing to the values of ε_1 and ε_2. Importantly, there are clear
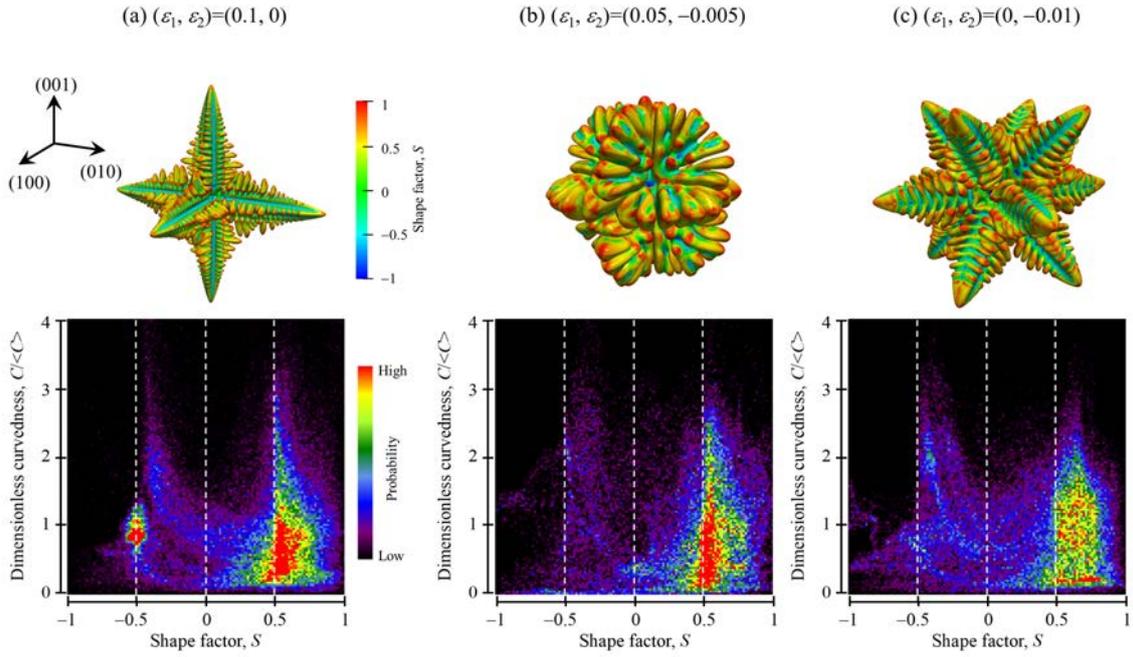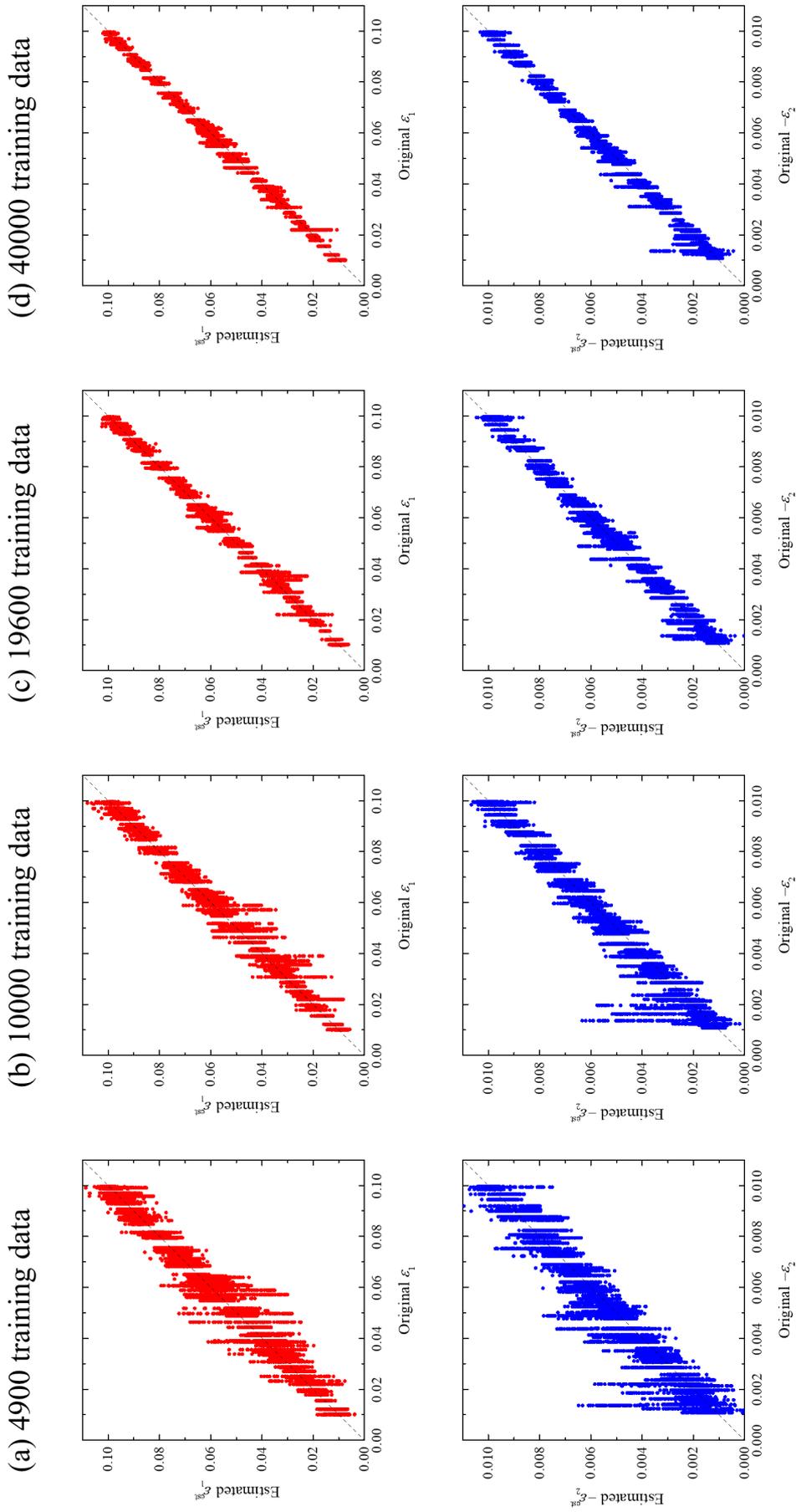
Fig. 5.6. Growth morphologies (upper) and ISD maps (lower) at $t = 40000\Delta t$ in (a) $\langle 100 \rangle$, (b) hyperbranched, and (c) $\langle 110 \rangle$ growth modes.

differences between the ISD maps, indicating that the different values of ε_1 and ε_2 yield the difference in the ISD map. Figure 5.7 shows the ISD maps at $t = 40000\Delta t$ for different values of ε_1 and ε_2 indicated in the omorphology map (center), where the regions of $\langle 100 \rangle$ growth, $\langle 100 \rangle$−like hyperbranched growth, $\langle 110 \rangle$−like hyperbranched growth, and $\langle 110 \rangle$ growth are specified according to the previous work [15]. Although the difference is not always remarkable, the ISD maps differ according to the values of ε_1 and ε_2. This result supports the feasibility of the proposed approach.
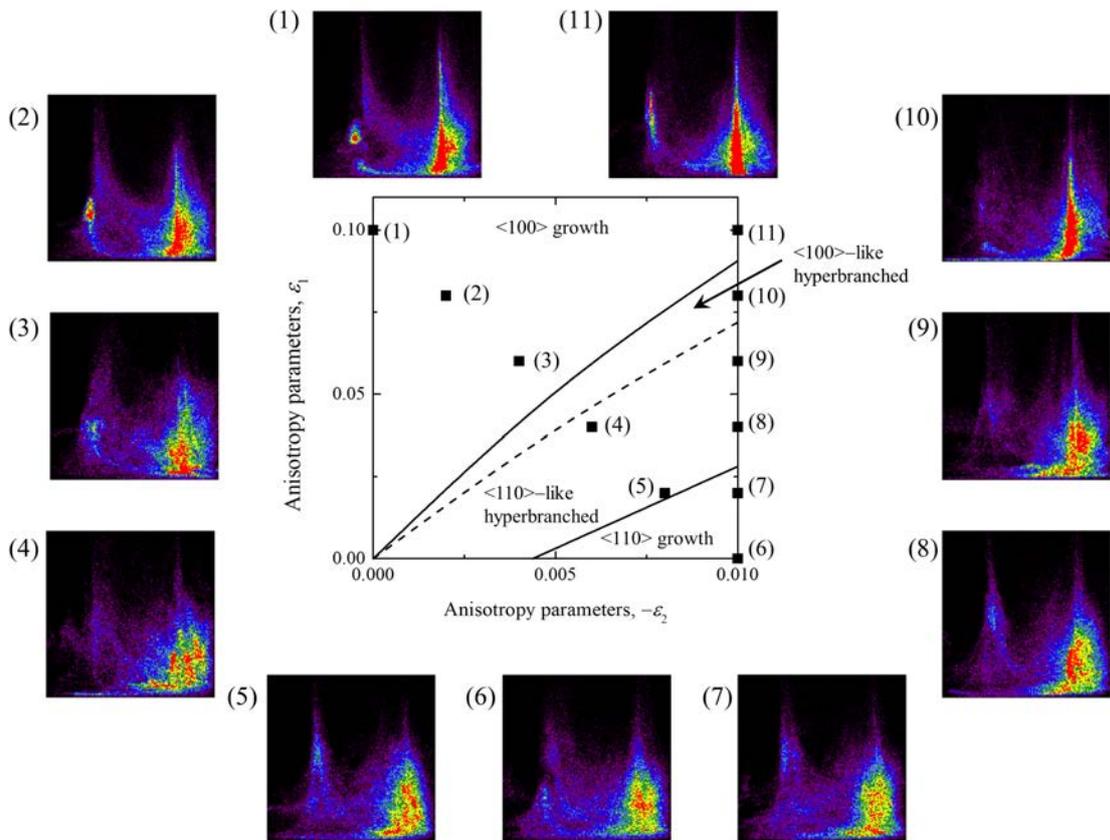
Fig. 5.7. ISD maps at $t = 40000\Delta t$ for different values of ε_1 and ε_2 indicated in the morphology selection map.

(a) 4900 training data

(b) 10000 training data

(c) 19600 training data

(d) 40000 training data

Fig. 5.8. Results of estimations of ε_1 and ε_2 obtained for different training datasets.

5.3.2 Estimation of anisotropy parameters

Figure 5.8 shows the estimation results for ε_1 and ε_2. In all the figures, the horizontal and the vertical axes represent the true value and that estimated by the machine learning model, respectively. The dashed (diagonal) line is shown for a visual aid to indicate the agreement between them. When the amount of training data is small, the accuracy is not high. However, the accuracy is improved by increasing the amount of training data.

Table 5.1: Relative and absolute error for ε_1 and ε_2.

	Error(ε_1), %	Error(ε_2), %	$|\varepsilon_1 - \varepsilon_1^{est}|$	$|\varepsilon_2 - \varepsilon_2^{est}|$
49 sets	7.163	15.029	3.32×10^{-3}	4.80×10^{-3}
100 sets	5.001	10.426	2.29×10^{-3}	3.16×10^{-3}
196 sets	3.287	5.470	1.45×10^{-3}	1.91×10^{-3}
400 sets	2.628	4.251	1.17×10^{-3}	1.42×10^{-3}

Table 5.1 shows the averages of the relative and absolute errors. The error for ε_2 is always larger than that for ε_1. Importantly, both ε_1 and ε_2 can be estimated with errors of less than 5% when employing the training dataset with 40000 maps. The accuracy is expected to further increase by increasing the size of the training dataset. Moreover, as a first attempt, we sampled the values of $(\varepsilon_1, \varepsilon_2)$ uniformly from the range of $\varepsilon_1 = [0, 0.1]$ and $\varepsilon_2 = [-0.01, 0]$ to obtain the training dataset. However, higher accuracy can be probably achieved by biased sampling of $(\varepsilon_1, \varepsilon_2)$. This point should be further investigated in a future work.

In the present approach, the ISD maps for different timesteps were utilized as the training data for each set of ε_1 and ε_2. Hence, ε_1 and ε_2 can be inversely estimated from the ISD map at any given time step. However, the accuracy of the estimation depends on the time at which the ISD map is obtained. The mean relative errors between the test data and estimated values were calculated every $500\Delta t$ for all sets of ε_1 and ε_2, which is given as:

$$\Delta E_i(t) = \frac{1}{m} \sum_{j}^{m} \left| \frac{\varepsilon_i^{est,j}(t) - \varepsilon_i^{true,j}}{\varepsilon_i^{true,j}} \right| \tag{5.7}$$

where $\Delta E_i(t)$ is the mean relative error of ε_i at t, $\varepsilon_i^{est,j}(t)$ is the estimation value of ε_i from the ISD map at t associated with j^{th} data in the test dataset, $\varepsilon_i^{true,j}$ is the corresponding true value and m is the total number of ISD map at each time step.
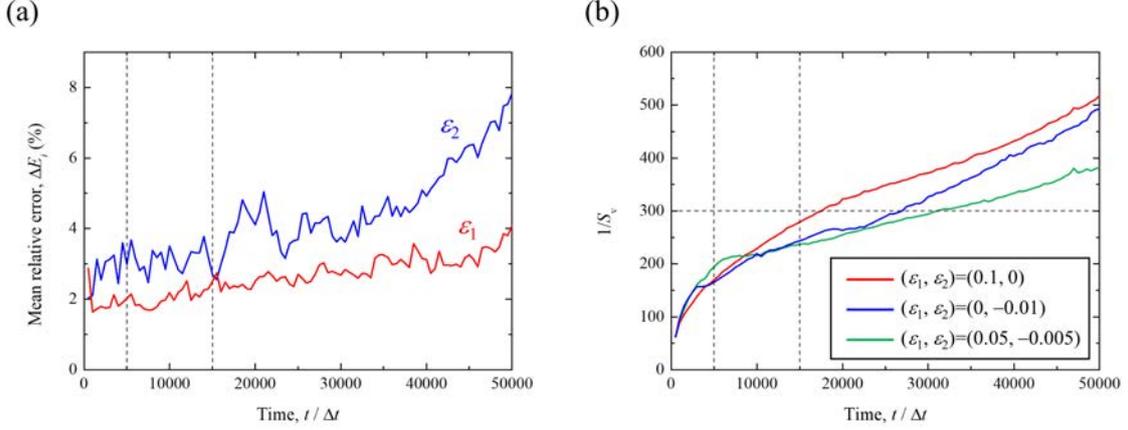
Fig. 5.9. Time changes of the (a) mean relative errors of ε_1 and ε_2 for the training dataset with 40,000 maps and (b) reciprocal of the surface area per unit volume of the solid phase for different anisotropy parameters.

Figure 5.9(a) shows the dependence of the relative errors on time for the training dataset with 40000 mapes. Both errors and relatively low in the period between approximately $5000\Delta t$ and $15000\Delta t$, as indicated by the vertical dashed lines. As is understood from Fig. 5.5, the ISD map is mainly determined by the growing shape of the primary arms during this period. Note that the value of $(\varepsilon_1, \varepsilon_2)$ determines the preferential growth direction (PGD) of dendrite, and the primary arms of free-growing dendrite exactly grow in the PGD. However, the growth direction of secondary arms may deviate from the PGD due to the overlapping of solute diffusion layer of neighboring secondary arms. Therefore, the ISD maps related to the growth of primary arms are more sensitive to the change of $(\varepsilon_1, \varepsilon_2)$ than those related to the growth of both primary and secondary arms. Accordingly, the former ISD maps are more suitable for estimation of $(\varepsilon_1, \varepsilon_2)$ than the latter ISD maps.

The values of $5000\Delta t$ and $15000\Delta t$ discussed above must depend on the initial supersaturation and alloy systems. Hence, it should be desirable to employ a different measure indicating the condition for accurate estimation. Since the present discussion is closely related to the morphology of dendrite, we chose the surface area per unit volume of solid S_v which has often been employed as a measure characterizing the whole morphology of dendrites in a general way. Figure 5.9(b) shows the

time change of the reciprocal of S_v calculated for $(\varepsilon_1, \varepsilon_2) = (0.1, 0)$, $(0, -0.01)$ and $(0.05, -0.005)$. In all cases, S_v^{-1} is lower than 300 during the period for accurate estimation. This value can be used as an approximate guide to obtain an accurate estimation using the proposed approach, though its validity and accuracy must be investigated in a future work.

Realizing the free growth of a dendrite during in-situ observations for long period of time is generally complicated because the effects of other dendrites and mold walls become non-negligible. Therefore, the results shown in Fig. 5.9 are favorable in terms of the actual application of the proposed approach. We emphasize that the application of the present approach is not limited to this time period. As shown in Fig. 5.9(a), a relative error of less than 10% can be expected for the ISD map in any time period tested. The error of less than 10% is considered low because errors of 10–50% are often involved in conventional approaches for estimation of anisotropy parameters [16]. More importantly, the accuracy of the present approach can be further improved by increasing the amount of training data.

In this study, the training data were limited to $u_0 = -0.3$. Because the morphology map shown in Fig. 5.7 is affected by the value of u_0 [15], further studies should be aimed at including the data for different initial supersaturations. The present approach should also be applied to different solidification conditions, such as continuous cooling and directional solidification. In addition, the estimation accuracy for different alloys, with different values of k and q_s and multicomponent alloys, need to be examined. Above all, the validity and efficacy of the present approach using real ISD map obtained by in-situ observation or other experimental techniques remain to be investigated in a future work.

5.4 Summary

In this chapter, a method of estimating anisotropy parameters of solid-liquid interfacial energy using inverse analysis was described. The ISD map, which characterizes the details of the dendrite morphology, was selected as the input for machine learning. The feasibility of this approach was tested by performing quantitative phase-field simulations for a free-growing 3D dendrite during isothermal solidification of a model alloy system to obtain training and test data. Both ε_1 and ε_2 were estimated with reasonable accuracy, which can be further improved by increasing the size of the training dataset.

References

[1] J. J. Koenderink, A. J. Van Doorn, Surface shape and curvature scales, Image and vision computing 10 (8) (1992) 557–564.

[2] R. Goldman, Curvature formulas for implicit curves and surfaces, Computer Aided Geometric Design 22 (7) (2005) 632–658.

[3] J. Gibbs, K. A. Mohan, E. Gulsoy, A. Shahani, X. Xiao, C. Bouman, M. De Graef, P. Voorhees, The three-dimensional morphology of growing dendrites, Scientific reports 5 (1) (2015) 1–9.

[4] C. M. Bishop, N. M. Nasrabadi, Pattern recognition and machine learning, Vol. 4, Springer, 2006.

[5] R. Yamashita, M. Nishio, R. K. G. Do, K. Togashi, Convolutional neural networks: an overview and application in radiology, Insights into imaging 9 (4) (2018) 611–629.

[6] R. Kondo, S. Yamakawa, Y. Masuoka, S. Tajima, R. Asahi, Microstructure recognition using convolutional neural networks for prediction of ionic conductivity in ceramics, Acta Materialia 141 (2017) 29–38.

[7] S. M. Azimi, D. Britz, M. Engstler, M. Fritz, F. Mücklich, Advanced steel microstructural classification by deep learning methods, Scientific reports 8 (1) (2018) 1–14.

[8] J. Yeom, T. Stan, S. Hong, P. W. Voorhees, Segmentation of experimental datasets via convolutional neural networks trained on phase field simulations, Acta Materialia 214 (2021) 116990.

[9] T. Stan, Z. T. Thompson, P. W. Voorhees, Optimizing convolutional neural networks to perform semantic segmentation on large materials imaging datasets: X-ray tomography and serial sectioning, Materials Characterization 160 (2020) 110119.

[10] A. Krizhevsky, I. Sutskever, G. E. Hinton, Imagenet classification with deep convolutional neural networks, Advances in neural information processing systems 25.

[11] D. Ciregan, U. Meier, J. Schmidhuber, Multi-column deep neural networks for image classification, in: 2012 IEEE conference on computer vision and pattern recognition, IEEE, 2012, pp. 3642–3649.

[12] D. C. Ciresan, U. Meier, J. Masci, L. M. Gambardella, J. Schmidhuber, Flexible, high performance convolutional neural networks for image classification, in: Twenty-second international joint conference on artificial intelligence, 2011.

[13] J. J. Hoyt, M. Asta, A. Karma, Atomistic and continuum modeling of dendritic solidification, Materials Science and Engineering: R: Reports 41 (6) (2003) 121–163.

[14] T. Haxhimali, A. Karma, F. Gonzales, M. Rappaz, Orientation selection in dendritic evolution, Nature materials 5 (8) (2006) 660.

[15] G. Kim, T. Takaki, Y. Shibuta, S. Sakane, K. Matsuura, M. Ohno, A parametric study of morphology selection in equiaxed dendritic solidification, Computational Materials Science 162 (2019) 76–81.

[16] R. E. Napolitano, S. Liu, Three-dimensional crystal-melt wulff-shape and interfacial stiffness in the al-sn binary system, Physical Review B 70 (21) (2004) 214103.

Chapter 6

Conclusions

In this study, morphological diversity of solidification microstructures associated with transition in anisotropy of solid-liquid interfacial energy were closely investigated by means of quantitative phase-field simulations for fcc-based binary model alloys. By changing anisotropy parameters systematically, growth morphologies of isothermally- and directionally-solidified microstructures were classified. Then morphology maps were constructed for both isothermally- and directionally solidified microstructures. In addition, influences of solidification conditions and alloy sytem on morphological maps were also investigated.

On the one hand, a method for estimation anisotropy parameters of solid–liquid interfacial free energy was proposed based on inverse problem approach combining quantitative phase-field simulations and machine learning. The interfacial shape distribution (ISD) map, which characterizes the details of the dendrite morphology, was selected as the input for machine learning. The feasibility of this approach was tested by performing quantitative phase-field simulations for a isothermally-solidified microstructures of a model alloy system to obtain training and test data. Both ε_1 and ε_2 were estimated with reasonable accuracy less than 5%, which can be further improved by increasing the size of the training dataset.

In chapter 1, the effect and importance of anisotropy parameters on the growth morphologies of soldification microstructures were described. In addition, an overview of previous studies related to the topic and the necessity of further studies were explained [1–7].

In chapter 2, the phase-field model used in this study was explained in detail. First, the solid-liquid interface was represented as diffuse interface by introducing

a phase-field variable. The time evolution equation of conserved quantity (Cahn-Hilliard equation) and non-conserved quantity (Allen-Cahn equation) were derived from free energy functional based on the second law of thermodynamics. The classical sharp interface models for both solidification of pure substance and alloy were described. Then, the quantitative phase-field model used in this study was explained. By introducing the quantitative phase-field model, the quantitative defects of the conventional models was resolved. In addition, the anisotropic solid-liquid interfacial energy to correctly simulate three-dimensional solidification microstructure was also described and the suitable form for applying it to numerical simulation was derived. The quantitative phase-field model for directional solidification and the normalization of the models described so far were explained. Finally, preconditioning technique to enhance the numerical stability for larger grid spacings in phase-field simulation was briefly explained.

In chapter 3, first of all, the computational conditions for the simulations of isothermal solidification and the acceleration method using graphical processing units (GPU) were described. Under these conditions, morphological diversity of isothermally-solidified microstructure associated with transition in anisotropy parameters was investigated by systematically changing ε_1 and ε_2. The growth morphologies were classified into four types, i.e. $\langle 100 \rangle$, $\langle 100 \rangle$-like hyperbranched, $\langle 110 \rangle$-like hyperbranched and $\langle 110 \rangle$ growth. From this classification, the morphology map for isothermally-solidified microstructure was constructed. Furthermore, dependencies of this map on solidification condition and alloy system were also investigated by changing initial supersaturation and partition coefficient, respectively. It was found that $\langle 100 \rangle$ growth, which is typical growth pattern of fcc-based alloy, hardly occurs when initial supersaturation is large and/or partition coefficient is small [8].

In chapter 4, morphological diversity of directionally-solidified microstructure associated with transition in anisotropy parameters was investigated by systematically changing ε_1, ε_2 and the angle between $\langle 100 \rangle$ crystallographic orientation and heat flow direction. The growth morphologies were classified into three types, i.e. $\langle 100 \rangle$, seaweed and $\langle 110 \rangle$ growth. From this classification, the morphology map for directionally-solidified microstructure was constructed. Furthermore, dependence of this map on solidification conditions, pulling speed and temperature gradient, was

investigated. It was found that the seaweed growth region in the space of ε_1 and ε_2 slightly becomes wider as the pulling speed decreases. It was also found that there was no change in morphology map in the range of temperature gradient $5-15$ K/mm with fixed pulling speed $V_p = 500$ μm/s.

The morphology map of isothermally- and directionally-solidified microstructure serves as a basis for understanding of occurrence of various growth morphologies associated with anisotropy parameters of solid-liquid interfacial energy. From the morphology maps obtained in this study, solidification microstructure of alloys can be predicted with different anisotropy parameters, solidification condition and alloy system. Therefore, construction of the morphology map with high accuracy is of great importance in controlling solidification microstructures considering transition in anisotropy parameters.

In chapter 5, a method for estimation anisotropy parameters of solid–liquid interfacial free energy was proposed. Interfacial shape distribution (ISD) map that characterize the three-dimensional morphology of solidification microstructure was explained. ISD map represents the existing probability of curvedness and shape factor of the local interface of 3D morphology, then the complex three-dimensional morphology map can be summarized into two-dimensional ISD map. The ISD map was selected as a material for inverse analysis that estimates anisotropy parameters using machine learning. ISD maps at different values of $(\varepsilon_1, \varepsilon_2)$ were obtained from phase-field simulations of fcc model alloy for isothermal solidification. Then those maps were trained through convolutional neural network (CNN) to match the relationship between ISD map and $(\varepsilon_1, \varepsilon_2)$. Using CNN model, $(\varepsilon_1, \varepsilon_2)$ can be estimated from a given ISD map. Both ε_1 and ε_2 were estimated with an accuracy less than 5%, which can be further improved by increasing the size of the training dataset [9].

In this study, anisotropy parameters were estimated only for isothermal solidification microstructures with a fixed initial supersaturation u_0. Because the morphology map can be influenced by u_0 [8], further investigations hould be aimed including the data for different initial supersaturations. The present approach should also be applied to different solidification processes, such as continuous cooling and directional solidification. In addition, the estimation accuracy for different alloys, with different values of partition coefficient, k, the ratio of diffusivity in solid-liquid phases, q_s and

multicomponent alloys, need to be examined. Above all, the validity and efficacy of the present approach using real ISD map obtained by in-situ observation [10] or other experimental techniques [11] remain to be investigated in a future work.

References

[1] T. Haxhimali, A. Karma, F. Gonzales, M. Rappaz, Orientation selection in dendritic evolution, Nature materials 5 (8) (2006) 660.

[2] J. Dantzig, P. Di Napoli, J. Friedli, M. Rappaz, Dendritic growth morphologies in Al-Zn alloys –PartII: phase-field computations, Metallurgical and Materials Transactions A 44 (12) (2013) 5532–5543.

[3] M. Wang, Y. Xu, Q. Zheng, S. Wu, T. Jing, N. Chawla, Dendritic growth in Mg-based alloys: phase-field simulations and experimental verification by X-ray synchrotron tomography, Metallurgical and Materials Transactions A 45 (5) (2014) 2562–2574.

[4] S. Shuai, E. Guo, Q. Zheng, M. Wang, T. Jing, Y. Fu, Three-dimensional α-Mg dendritic morphology and branching structure transition in Mg-Zn alloys, Materials Characterization 118 (2016) 304–308.

[5] Z. Chen, E. Wang, X. Hao, Microstructure and orientation evolution in unidirectional solidified Al–Zn alloys, Materials Science and Engineering: A 667 (2016) 1–8.

[6] M. Becker, J. Dantzig, M. Kolbe, S. T. Wiese, F. Kargl, Dendrite orientation transition in alge alloys, Acta Materialia 165 (2019) 666–677.

[7] L. Wang, J. J. Hoyt, N. Wang, N. Provatas, C. W. Sinclair, Controlling solid-liquid interfacial energy anisotropy through the isotropic liquid, Nature communications 11 (1) (2020) 1–7.

[8] G. Kim, T. Takaki, Y. Shibuta, S. Sakane, K. Matsuura, M. Ohno, A parametric study of morphology selection in equiaxed dendritic solidification, Computational Materials Science 162 (2019) 76–81.

[9] G. Kim, R. Yamada, T. Takaki, Y. Shibuta, M. Ohno, Inverse analysis of anisotropy of solid-liquid interfacial free energy based on machine learning, Computational Materials Science 207 (2022) 111294.

[10] T. Stan, Z. T. Thompson, P. W. Voorhees, Optimizing convolutional neural networks to perform semantic segmentation on large materials imaging datasets: X-ray tomography and serial sectioning, Materials Characterization 160 (2020) 110119.

[11] J. Yeom, T. Stan, S. Hong, P. W. Voorhees, Segmentation of experimental datasets via convolutional neural networks trained on phase field simulations, Acta Materialia 214 (2021) 116990.

Acknowledgement

I spent more than five years in the Laboratory of Microstructure Control and met many people. I was able to learn a lot from them and make a lot of memories. In particular, with Jaehoon Lee, Takahisa Kinoshita, Tomoya Nakayama and Koharu Takano, I made unforgettable memories and pleasure in academic confernces and Nomikai. A big thank you to all the former and current laboratory members.

I cannot help but thank my colleagues of Korea-Japan Joint Government Scholoship in Hokkaido University: Soobeom Lee, Yongjoon Kim, Seokjin Na, Junbum Park, and Minhyeok Park. I would also like to thank other member of Korea-Japan Joint Government Scholoship in Hokkaido University: Chunghyeon Lee, Hyeongtae Lee, Yungoo Ro, Seunggoo Rim, Seongwoo Jung and Gun Yoon (special thanks to him for helping managing our lab server).

I really appreciate Daeun Kim for everything. Thank you for your support and make me happy all the time. Let's be happy together. I love you.

Last but not least, I would like to thank my parents for their support, sacrifice, and love.

<div align="right">

Research Group of Materials Design

Laboratory of Microstructure Control

Geunwoo Kim

</div>

Appendix

Publications

- <u>G. Kim</u>, T. Takaki, Y. Shibuta, S. Sakane, K. Matsuura, M.Ohno, "A parametric study on morphology selection in equiaxed dendritic solidification", Comput. Mater. Sci., **162** (2019), 76.

- R. Yamada, M. Kudo, <u>G. Kim</u>, T. Takaki, Y. Shibuta, M. Ohno, "Time invariance of three-dimensional morphology of equiaxed dendrite: A Phase-field study", Comput. Mater. Sci., **204** (2022), 111173.

- <u>G. Kim</u>, R. Yamada, T. Takaki, Y. Shibuta, M. Ohno, "Inverse analysis of anisotropy of solid-liquid interface free energy based on machine learning", Comput. Mater. Sci., **207** (2022), 111294.

International Conferences

- <u>G. Kim</u>, M. Ohno, K. Matsuura, "Phase-field simulation of morphological change of equiaxed dendrite for different preferred growth directions", The 10th Pacific Rim International Conference on Modeling of Casting and Solidification Process (MCSP 2017), Beijing, China, 21-23 Aug. 2017. [Oral]

- <u>G. Kim</u>, M. Ohno, K. Matsuura, T. Takaki, "Quantitative phase-field simulations for solidification microstructure with different preferred growth direction", The 13th World Congress in Computational Mechanics (WCCM2018), New York City, USA, 22-27 July 2018. [Oral]

- <u>G. Kim</u>, M. Ohno, T. Takaki, Y. Shibuta, K. Matsuura, "Phase-field simulation for morphological change of solidification structure with transition in

preferred growth orientation", 55th Annual Technical Meeting of the Society of Engineering Science (SES2018), Madrid, Spain, 10-12 Oct. 2018. [Oral]

- <u>G. Kim</u>, T. Takaki, Y. Shibuta, S. Sakane, M. Ohno, "Phase-field simulation on morphological change of dendrite with different preferred growth directions", 5th International Conference on Advances in Solidification Process (ICASP-5), Salzburg, Austria, 17-21 June 2019. [Poster]

- <u>G. Kim</u>, T. Takaki, Y. Shibuta, S. Sakane, M. Ohno, "Phase-field simulation on morphological diversity of solidification structure with different preferred growth directions", The 4th International Symposium on Phase-field Modelling in Materials Science (PF19), Bochum, Germany, 22-25 July 2019. [Oral]

- <u>G. Kim</u>, T. Takaki, Y. Shibuta, M. Ohno, "A method of estimation of solid-liquid interface anisotropy based on machine learning combined with phase-field simulations", TMS 2021 Annual Meeting and Exhibition, Virtual Conference, 14-18 Mar. 2021. [Oral]

Domestic Conferences and Symposium

- <u>G. Kim</u>, M. Ohno, K. Matsuura, "結晶の優先成長方位とデンドライト成長形態との関係", Hokkaido Chapter Meeting of Japan Institute of Metals and Materials, Muroran, Japan, 14 July 2017. [Poster]

- <u>G. Kim</u>, M. Ohno, K. Matsuura, "優先成長方位遷移現象に伴う等軸デンドライト形態変化のシミュレーション", Annual Meeting of Japan Insitute of Metals and Materials, Sapporo, Japan, 6-8 Sep. 2017. [Oral]

- <u>G. Kim</u>, M. Ohno, K. Matsuura, "Phase-field study on growth morphology of dendrite with different interfacial anisotropy", AGH-HU Joint Symposium, Krakow, Poland, 6-8 May 2018. [Oral and Poster]

- <u>G. Kim</u>, T. Takaki, Y. Shibuta, K. Matsuura, M. Ohno, "優先成長方位遷移に伴う一方向凝固組織の形態変化のフェーズフィールド・シミュレーション", Annual Meeting of Japan Insitute of Metals and Materials, Tokyo, Japan, 20-22 Mar. 2019. [Poster]

- <u>G. Kim</u>, S. Sakane, T. Takaki, Y. Shibuta, M. Ohno, "Diverse Growth Morphology of Directionally-solidified Microstructure with Different Preferred Growth Directions", Annual Meeting of Korean Institute of Metals and Materials, Daegu, Korea, 23-25 Oct. 2019. [Oral]

- <u>G. Kim</u>, T. Takaki, Y. Shibuta, M. Ohno, "Phase-field simulations for diverse morphology in dendritic growth with transition in preferred growth direction", HU-SNU Joint Symposium, Seoul, Korea, 14 Nov. 2019. [Oral]

- <u>G. Kim</u>, T. Takaki, Y. Shibuta, M. Ohno, "Estimation of solid-liquid interface anisotropy based on phase-field simulations and machine learning", Annual Meeting of Korean Institute of Metals and Materials, Virtual Conference, 28-30 Apr. 2021. [Oral]

Awards and Hornors

- Korea-Japan Joint Govermment Scholarship (Mar. 2011–Mar. 2016)

- Encouragement prize: JIMM and ISIJ (23 Mar. 2017)

- Best Oral Presentation Award: MCSP 2017 (23 Aug. 2017)

- AEON 1% International Scholoship (Apr. 2018–Mar. 2019)

- Best Poster Award:Annual Meeting of JIMM (21 Mar. 2019)

- Best Oral Presentation Award: Annual Meeting of KIMM (30 Apr. 2021)

- Fellowship from Japan Society for the Promotion of Science (DC2)
  (Apr. 2020–Mar. 2022)